NUREG/CR-5385
ANL-89/17

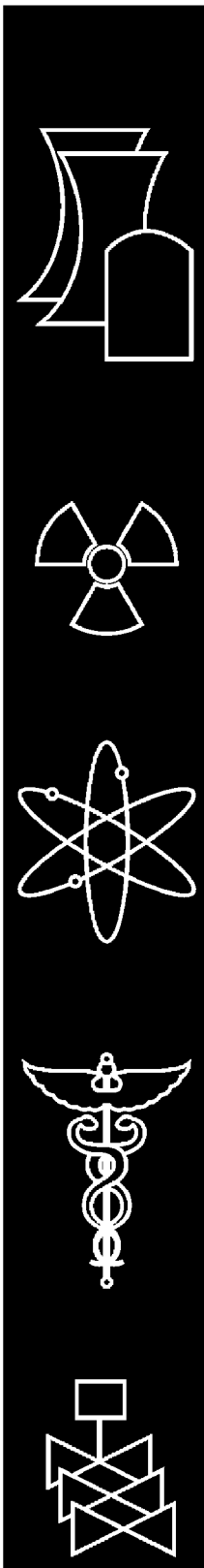

Initial Assessment of the Mechanisms and Significance of Low-Temperature Embrittlement of Cast Stainless Steels in LWR Systems

Argonne National Laboratory

U.S. Nuclear Regulatory Commission
Office of Nuclear Regulatory Research
Washington, DC 20555-0001

NUREG/CR-5385
ANL-89/17

Initial Assessment of the Mechanisms and Significance of Low-Temperature Embrittlement of Cast Stainless Steels in LWR Systems

Manuscript Completed: May 1989
Date Published: August 1990

Prepared by
O.K. Chopra, A. Sather

Argonne National Laboratory
9700 South Cass Avenue
Argonne, IL 60439

Prepared for
Division of Engineering
Office of Nuclear Regulatory Research
U.S. Nuclear Regulatory Commission
Washington, DC 20555-0001
NRC FIN A2243

Initial Assessment of the Mechanisms and Significance of Low–Temperature Embrittlement of Cast Stainless Steels in LWR Systems

O. K. Chopra and A. Sather

Abstract

This report summarizes work performed by Argonne National Laboratory on long-term embrittlement of cast duplex stainless steels in LWR systems. Metallurgical characterization and mechanical property data from Charpy-impact, tensile, and J-R curve tests are presented for several experimental and commercial heats, as well as for reactor-aged CF-3, CF-8, and CF-8M cast stainless steels. The effects of material variables on the embrittlement of cast stainless steels are evaluated. Chemical composition and ferrite morphology strongly affect the extent and kinetics of embrittlement. In general, the low-carbon CF-3 stainless steels are the most resistant and the molybdenum-containing high-carbon CF-8M stainless steels are most susceptible to embrittlement. The microstructural and mechanical–property data are analyzed to establish the mechanisms of embrittlement. The procedure and correlations for predicting the impact strength and fracture toughness of cast components during reactor service are described. The lower bound values of impact strength and fracture toughness for low-temperature–aged cast stainless steel are defined.

Contents

List of Tables

List of Figures

Executive Summary

A program is being conducted to investigate the significance of low–temperature embrittlement of cast duplex stainless steels under light water reactor operating conditions and to evaluate possible solutions to the embrittlement problem for existing and future plants. The scope of the investigation includes the following goals: (1) establish the mechanism of embrittlement and validate the simulation of in–reactor degradation by accelerated aging, (2) evaluate the effects of key compositional and metallurgical variables on embrittlement, and (3) obtain fracture toughness data to predict the degree of toughness loss suffered by cast stainless steel components during normal and extended service life of reactors.

Microstructural and mechanical–properties data were obtained on 25 experimental heats (static–cast keel blocks and slabs) and six commercial heats (centrifugally cast pipes and static–cast pump impeller and pump casing ring) as well as reactor–aged material of grades CF–3, CF–8, and CF–8M cast stainless steel. All cast materials were characterized and the data on chemical composition, ferrite content, hardness, ferrite morphology, and grain structure are presented. The ferrite content of the cast materials ranged between 3 and 30%. The ferrite morphology for the castings containing >5% ferrite were either lacy or acicular. The centrifugally cast pipe material had equiaxed or radially oriented columnar grains, while the static–cast keel blocks, slabs, and the pump impeller had a mixed grain structure.

Charpy–impact, tensile, and J–R curve tests were conducted on several experimental and commercial heats of cast stainless steel that were thermally aged up to 30,000 h at temperatures between 290 and 450°C (~555 and 840°F). The results indicate that aging at these temperatures leads to an increase in tensile strength, a decrease in impact energy, fracture toughness J_{IC}, and tearing modulus of the material, and the ductile–to–brittle transition curve shifts to higher temperatures. In general, low–carbon CF–3 cast stainless steels were most resistant and molybdenum–containing high–carbon CF–8M steels were most susceptible to low–temperature embrittlement. Ferrite morphology had a strong effect on the degree or extent of embrittlement, whereas small changes in material composition significantly altered the kinetics of embrittlement.

The mechanisms of embrittlement of cast duplex stainless steel have also been established. Embrittlement occurs when failure is dominated by brittle fracture associated with either cleavage of ferrite or separation of ferrite/austenite phase boundaries. The formation of α' phase by spinodal decomposition of the ferrite is the primary strengthening mechanism that can raise local tensile stresses above the critical value for cleavage and, thus, promote brittle fracture. Precipitation and/or growth of phase boundary carbides or nitrides leads to a brittle failure by phase boundary separation and also facilitates cleavage of the ferrite by particle cracking. The degree of brittle fracture and, hence, the degree of embrittlement of a specific heat of cast stainless steel, depends strongly on the amount and spacing of the ferrite in the duplex structure. Cast materials that are sensitive to embrittlement either have a semicontinuous ferrite morphology or provide an easy fracture path via phase boundary separation. For other materials, although a portion of the material may fail in a brittle fashion, the surrounding austenite provides ductility and toughness, e.g., cast materials with low ferrite content or the low–carbon cast stainless steels.

The kinetics of embrittlement are controlled by three processes, viz., spinodal decomposition, precipitation and growth of phase boundary carbides, and precipitation of G phase in ferrite. The interactions of these processes lead to apparent activation energies that range between 65 and 230 kJ/mole. The influence of material variables on the kinetics of embrittlement is discussed, and correlations for the activation energy in terms of material composition are presented.

The loss of toughness of cast stainless steels can be recovered by a short–term anneal of 1 h at 550°C and water quenching. However, preliminary data show that the recovery–annealed material reembrittles in a relatively short time.

A method and examples of estimating the impact strength and fracture toughness of cast components during reactor service are described. The results indicate that the lower bound values of impact energy, fracture toughness J_{IC}, and tearing modulus at room temperature could be as low as 20 J/cm^2 (11.8 ft·lb), 25 kJ/m^2 (143 in.–lb/in.^{2}), and 24, respectively. Correlations for estimating the toughness at reactor temperatures are being developed. Available data indicate that the lower–bound values of toughness at reactor temperatures are ~50% higher than those at room temperature. These values may be very conservative for most heats of material. The present analysis has focussed on assuring that the correlations are adequately conservative for “bad” heats.

1 Introduction

Cast duplex stainless steels are used extensively in the nuclear industry for valve bodies, pump casings, and primary coolant piping. The ferrite phase in the duplex structure of austenitic–ferritic stainless steels increases the tensile strength and improves the soundness of casting, weldability, and resistance to stress corrosion cracking of these steels. However, various carbide phases, intermetallic compounds such as sigma and chi phases, and the chromium–rich bcc phase (α') can precipitate in the ferrite matrix during service at elevated temperatures and lead to substantial degradation in mechanical properties. It has been known for almost 40 years that binary iron–chromium alloys and ferritic stainless steels are susceptible to severe embrittlement when exposed to temperatures in the range of 300 to 500°C (~570 to 930°F).[1–7] The potential for significant embrittlement of cast duplex stainless steels has been confirmed by recent studies on cast materials that were aged at temperatures between 300 and 450°C for times up to 70,000 h (~8 yr).[8–17]

The time–temperature curves for the formation of various phases and the change in impact strength of thermally aged cast duplex stainless steel[15] are shown in Fig. 1. The results indicate that at temperatures above 550°C (1020°F), the embrittlement is largely due to formation of sigma phase, and below 500°C (930°F), precipitation of α' phase leads to embrittlement. Formation of carbides and chi phase influences mechanical properties in the 500 to 600°C (930 to 1110°F) temperature range. At the operating temperatures of

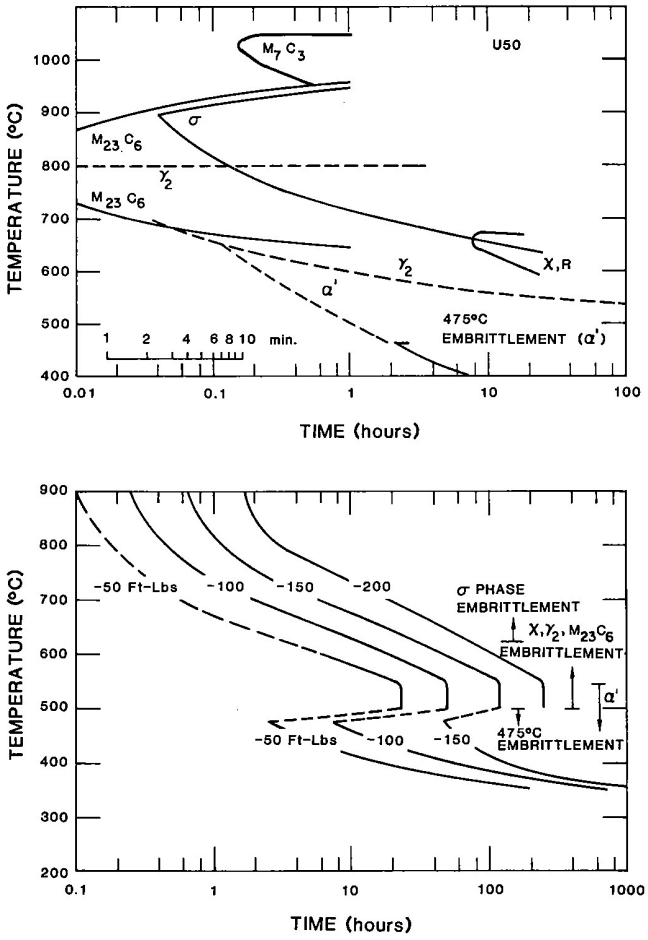

Figure 1. Time–Temperature Curve for (Top) Formation of Various Phases and (Bottom) Decrease in Room Temperature Impact Energy in Cast Stainless Steel (Ref. 15).

light–water reactors (LWRs), i.e., 280 to 320°C (535 to 610°F), embrittlement of ferritic or duplex stainless steels is primarily caused by α' precipitation.

Thermal aging of cast duplex stainless steels at temperatures between 300 and 450°C causes an increase in hardness and tensile strength and a decrease in ductility, Charpy–impact strength, and fracture toughness of the material.[8–15] However, the low–cycle fatigue properties and fatigue crack propagation rates are not modified significantly by low–temperature aging.[10,11] The room temperature impact energy can be reduced by ~80% after aging for ~8 yr at temperatures as low as 300°C (570°F). The ferrite content of the cast material has a pronounced influence on the embrittlement behavior, viz., an increase in ferrite content increases the susceptibility to embrittlement, Fig. 2. Also, the addition of molybdenum to the steel, i.e., CF–8M grade stainless steel, increases both the rate and extent of embrittlement.

The data for single–phase binary Fe–Cr ferritic alloys are helpful in gaining insight into the effects of composition on aging and in identifying possible mechanisms of embrittlement. Unfortunately, the bulk of this work has been carried out at temperatures of 400°C (750°F) or above, and caution must be observed in extrapolating the data to reactor temperatures. Data on the thermal aging of single–phase ferritic alloys indicate that an increase in the chromium, molybdenum, or titanium content of the ferrite phase decreases the time required for embrittlement.[6] The influence of chromium is more pronounced

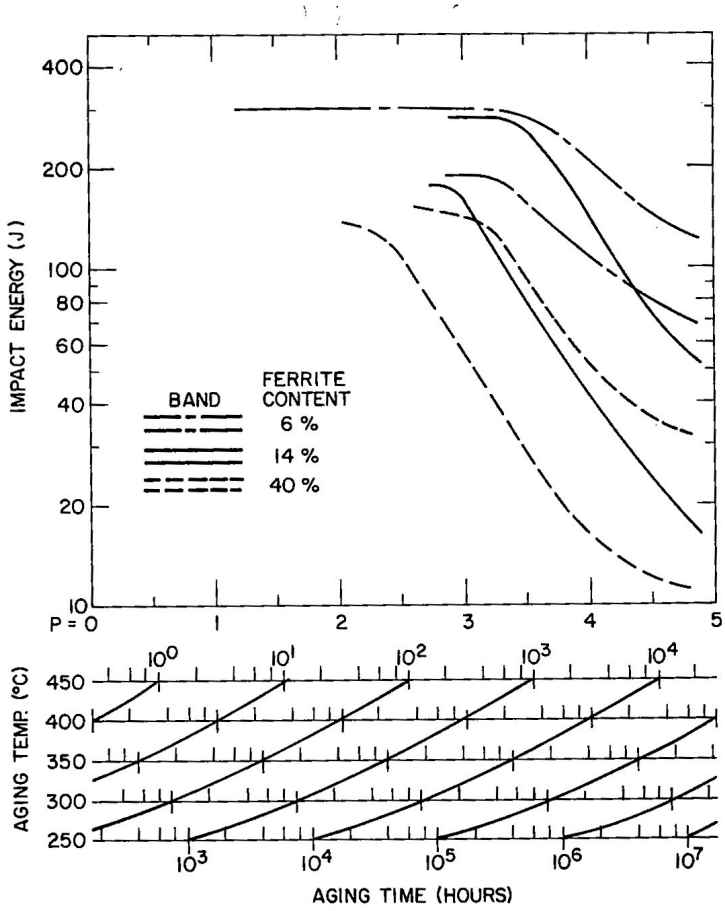

Figure 2. Influence of Ferrite Content on the Embrittlement of Cast Stainless Steel.

than that of molybdenum or titanium. Variations in manganese or silicon content have no effect on the aging behavior.[17] For single–phase Fe–Cr–Ni alloys, an increase in the nickel content promotes α' precipitation,[17] but the higher nickel ferritic steels take longer to embrittle because other deformation modes, such as twinning, are promoted by additions of nickel.[18–21] Interstitial elements such as carbon and nitrogen also accelerate embrittlement of single–phase ferritic steels. Nitrogen in the ferrite phase influences the aging behavior by enhancing the precipitation of the α' phase and by the formation of nitrides or carbonitrides.[5,6,22,23]

The degree of embrittlement has generally been characterized in terms of Charpy–impact energy of notched toughness specimens. The current "best estimates" of the degree of embrittlement at reactor operating temperatures are obtained from Arrhenius extrapolations of laboratory data obtained at higher temperatures.[8] The aging time to reach a given degree of embrittlement at different temperatures is determined from the equation

$$t = 10^{P} \exp\left[\frac{Q}{R}\left\{\frac{1}{T} - \frac{1}{673}\right\}\right] \qquad (1)$$

where Q is the activation energy, R the gas constant, T the absolute temperature, and P an aging parameter that represents the degree of aging reached after 10^{P} h at 400°C (750°F). The activation energy for the process of embrittlement has been described as a function of the chemical composition of the cast material.[11] Thus,

$$Q(\text{kJ/mole}) = -182.6 + 19.9(\%\ \text{Si}) + 11.08(\%\ \text{Cr}) + 14.4(\%\ \text{Mo}),$$

or

$$Q(\text{kcal/mole}) = -43.64 + 4.76(\%\ \text{Si}) + 2.65(\%\ \text{Cr}) + 3.44(\%\ \text{Mo}). \qquad (2)$$

The activation energy calculated from Eq. (2) for the process of embrittlement, ranges between 65 and 105 kJ/mole (15 and 25 kcal/mole) for CF–3, CF–8, and CF–8M cast stainless steels. For a given composition of the cast material, Eqs. (1) and (2) can be used to determine the aging conditions that are representative of end–of–life reactor service. For a cast material with an activation energy of 100 kJ/mole (24 kcal/mole), the end–of–life condition for cold–leg piping, i.e., 40 yr at 290°C (555°F), is equivalent to 10,000 h at 400°C, and the end–of–life condition for hot–leg piping, i.e., 40 yr at 320°C (610°F), is equivalent to 30,000 h at 400°C. Consequently, the laboratory data obtained for materials aged at 400°C are currently used to predict the end–of–life impact strength at reactor temperatures.

Simulation of reactor conditions by accelerated aging is valid only when it can be established that the same mechanisms are operating over the temperature range involved in the extrapolation. The Charpy–impact data for aged cast stainless steel, in general, yield activation energies well below the 202 kJ/mole (48 kcal/mole) value associated with chromium bulk diffusion in the Fe–28Cr alloy, the process that has most commonly been assumed to be rate–controlling in the low–temperature embrittlement of ferritic steels.[24] These results indicate that the mechanisms of embrittlement change over the temperature range of 300 to 450°C. Additional data on the kinetics and extent of embrittlement at LWR operating temperatures, as well as other measures of fracture toughness, viz., J–R curves, are needed to evaluate the in–service embrittlement of cast stainless steels.

The objective of this program is to investigate the significance of low–temperature embrittlement of cast duplex stainless steels under LWR operating conditions and to evaluate possible solutions to the embrittlement problem for existing and future plants. The scope of the investigation includes the following goals: (1) characterize and correlate the microstructure of in–service reactor components and laboratory–aged material with loss of fracture toughness to establish the mechanism of aging and to validate the simulation of in–reactor degradation by accelerated aging, (2) establish the effects of key compositional and metallurgical variables on the kinetics and extent of embrittlement, and (3) obtain fracture toughness data on long–term–aged materials for extrapolation to predict the degree of toughness loss suffered by cast stainless steel components during normal and extended service life of reactors. This report presents the results obtained from Charpy–impact, tensile, and J–R curve tests on several heats of cast stainless steel aged up to 30,000 h at temperatures between 290 and 450°C (555 and 840°F). The mechanisms of embrittlement and the effects of chemical composition and ferrite morphology on the embrittlement behavior are discussed. The procedure and correlations for predicting the impact strength and fracture toughness of cast components during reactor service are described.

2 Experimental Procedure

2.1 Material Procurement

Material was obtained from various experimental and commercial heats of CF–3, CF–8, and CF–8M (ASTM Specification A 351 and A 451) cast stainless steels in different product forms and section thicknesses. Nineteen experimental heats of cast material were obtained in the form of keel blocks approximately 180 mm long and 120 mm high, with a thickness that tapered from 90 to 30 mm. The composition was varied to provide different concentrations of nickel, chromium, carbon, and nitrogen in the material, and ferrite content in the range of 3 to 30%, Table 1. Six of the experimental heats were also procured in the form of 76–mm–thick slabs. Materials from the commercial heats included sections of four different centrifugally cast pipes (CF–8 and CF–8M grades), a pump impeller (CF–3 grade), and a pump casing ring (CF–8 grade). The outer diameter and wall thickness of the cast pipes range from 0.6 to 0.9 m and 38.1 to 76.2 mm, respectively.

A cover plate assembly from the recirculating pump of the Gundremmingen (KRB) reactor was also procured. The cover plate assembly was in service for ~12 yr, i.e., ~8 yr at a service temperature of 284°C (543°F). The plate assembly was decontaminated and samples were obtained from the inner 25–mm thick region of the plate. The average temperature of the samples was estimated to be 280°C.

Fractured impact test bars from five heats of aged cast stainless steel were obtained from the Georg Fischer Co. (GF), Switzerland, for microstructural characterization. The materials were used earlier to study the long–term–aging behavior of cast stainless steel.[8] The specimens were aged for up to 70,000 h at 300, 350, and 400°C. The chemical composition and ferrite content of the laboratory–aged materials from the GF and reactor–aged material from the KRB reactor pump cover plate are given in Table 1.

Charpy–impact specimen blanks were obtained from material of all the experimental and commercial heats and from the KRB pump cover plate. Blanks for compact–tension

Table 1. Product Form, Chemical Analysis, Hardness, and Ferrite Morphology of Various Heats of Cast Stainless Steel

Heat	Grade	Composition (wt.%) Mn	Si	P	S	Mo	Cr	Ni	N	C	Ferrite[a] (%) Calc.	Meas.	Hardness R_B	Ferrite Spacing (μm)
							Keel Blocks[b]							
50	CF–3	0.60	1.10	0.016	0.007	0.33	17.89	9.14	0.079	0.034	3.0	4.4	80.1	194
49	CF–3	0.60	0.95	0.010	0.007	0.32	19.41	10.69	0.065	0.010	4.4	7.2	76.6	185
48	CF–3	0.60	1.08	0.009	0.006	0.30	19.55	10.46	0.072	0.011	5.1	8.7	78.1	127
47	CF–3	0.60	1.06	0.007	0.006	0.59	19.81	10.63	0.028	0.018	8.4	16.3	79.7	68
52	CF–3	0.57	0.92	0.012	0.005	0.35	19.49	9.40	0.052	0.009	10.3	13.5	81.6	69
51	CF–3	0.63	0.86	0.014	0.005	0.32	20.13	9.06	0.058	0.010	14.3	18.0	83.8	52
58	CF–8	0.62	1.12	0.010	0.005	0.33	19.53	10.89	0.040	0.056	3.2	2.9	77.1	303
54	CF–8	0.55	1.03	0.011	0.005	0.35	19.31	9.17	0.084	0.063	4.1	1.8	83.3	317
57	CF–8	0.62	1.08	0.009	0.004	0.34	18.68	9.27	0.047	0.056	4.4	4.0	80.2	138
53	CF–8	0.64	1.16	0.012	0.009	0.39	19.53	9.23	0.049	0.065	6.3	8.7	83.1	92
56	CF–8	0.57	1.05	0.007	0.007	0.34	19.65	9.28	0.030	0.066	7.3	10.1	82.5	84
59	CF–8	0.60	1.08	0.008	0.007	0.32	20.33	9.34	0.045	0.062	8.8	13.5	83.2	75
61	CF–8	0.65	1.01	0.007	0.007	0.32	20.65	8.86	0.080	0.054	10.0	13.1	85.3	82
60	CF–8	0.67	0.95	0.008	0.006	0.31	21.05	8.34	0.058	0.064	15.4	21.1	86.7	63
62	CF–8M	0.72	0.56	0.007	0.005	2.57	18.29	12.39	0.030	0.063	2.8	4.5	78.1	140
63	CF–8M	0.61	0.58	0.007	0.006	2.57	19.37	11.85	0.031	0.055	6.4	10.4	81.6	81
66	CF–8M	0.60	0.49	0.012	0.007	2.39	19.45	9.28	0.029	0.047	19.6	19.8	85.3	41
65	CF–8M	0.50	0.48	0.012	0.007	2.57	20.78	9.63	0.064	0.049	20.9	23.4	89.0	43
64	CF–8M	0.60	0.63	0.006	0.005	2.46	20.76	9.40	0.038	0.038	29.0	28.4	89.7	41
							76–mm Slabs[c]							
69	CF–3	0.63	1.13	0.015	0.005	0.34	20.18	8.59	0.028	0.023	21.0	23.6	83.7	35
73	CF–8	0.72	1.09	0.028	0.016	0.25	19.43	8.54	0.053	0.070	7.0	7.7	78.8	253
68	CF–8	0.64	1.07	0.021	0.014	0.31	20.64	8.08	0.062	0.063	14.9	23.4	84.6	87
70	CF–8M	0.55	0.72	0.021	0.016	2.30	19.17	9.01	0.049	0.066	14.2	18.9	86.5	96
74	CF–8M	0.54	0.73	0.022	0.016	2.51	19.11	9.03	0.048	0.064	15.5	18.4	85.8	90
75	CF–8M	0.53	0.67	0.022	0.012	2.58	20.86	9.12	0.052	0.065	24.8	27.8	89.5	69
							Reactor Components [d]							
P3	CF–3	1.06	0.88	0.017	0.014	0.01	18.89	8.45	0.168	0.021	2.8	1.9	82.2	–
P2	CF–3	0.74	0.94	0.019	0.006	0.16	20.20	9.38	0.040	0.019	12.5	15.6	83.8	69
I	CF–3	0.47	0.83	0.030	0.011	0.45	20.20	8.70	0.032	0.019	20.4	17.1	81.0	65
C1	CF–8	1.22	1.18	0.033	0.008	0.65	19.00	9.37	0.040	0.039	7.8	2.2	79.5	–
P1	CF–8	0.59	1.12	0.026	0.013	0.04	20.49	8.10	0.056	0.036	17.7	24.1	84.9	90
P4	CF–8M	1.07	1.02	0.019	0.015	2.05	19.64	10.00	0.151	0.040	5.9	10.0	83.1	182
205	CF–8M	0.93	0.63	0.019	–	3.37	17.88	8.80	–	0.040	21.0	15.9	–	79
758	CF–8M	0.91	0.62	0.018	–	3.36	17.91	8.7	–	0.030	24.2	19.2	–	62

Table 1. (Contd.)

Heat	Grade	Composition (wt.%) Mn	Si	P	S	Mo	Cr	Ni	N	C	Ferrite[a] (%) Calc.	Meas.	Hardness R_B	Ferrite Spacing (μm)
							Laboratory Aged[e]							
280	CF–3	0.50	1.37	0.015	0.006	0.25	21.60	8.00	0.038	0.028	36.3	40.0	–	186
278	CF–8	0.28	1.00	0.008	0.019	0.13	20.20	8.27	0.030	0.038	18.5	15.0	–	174
292	CF–8	0.34	1.57	0.018	0.016	0.13	21.60	7.52	0.039	0.090	23.9	28.0	–	–
286	CF–8M	0.40	1.33	0.044	0.015	2.44	20.20	9.13	0.062	0.072	18.9	22.0	–	201
							Reactor Aged[f]							
KRB	CF–8	0.31	1.17	–	–	0.17	21.99	8.03	0.038	0.062	27.7	34.0	–	–

a Calculated from the composition with Hulls equivalent factor
Measured by ferrite scope AUTO Test FE, Probe Type FSP–1

b *Static Cast Keel Blocks:* Foundry ESCO; Size 180x120x90–30 mm

c *Static Cast Slabs*: Foundry ESCO; Size 610x610x76 mm

d *Centrifugally Cast Pipes*:
P3 Foundry SANDUSKY; Size 580 mm O.D. 76 mm wall
P2 Foundry FAM, France; Size 930 mm O.D. 73 mm wall
P1 Foundry ESCO; Size 890 mm O.D. 63 mm wall
P4 Foundry SANDUSKY; Size 580 mm O.D. 32 mm wall
205 Size 305 mm O.D. 25 mm wall
Static Cast: Elbow 758: Size 305 mm O.D. 30 mm wall
Pump Impeller I: Foundry ESCO; Size 660 mm diameter
Pump Casing C1: Foundry ESCO; Size 600 mm O.D. 57 mm wall

e *Aged Material from George Fischer Co., Switzerland*

f *KRB Reactor Pump Cover Plate*: Foundry GF; Size 890 mm diameter

and tensile specimens were obtained from sections of cast pipes, a pump casing ring, a pump impeller, cast slabs, and the KRB pump cover plate. The specimen blanks from the experimental and commercial heats are being aged at 290, 320, 350, 400, and 450°C for times up to 50,000 h. The test matrix for the microstructural studies and mechanical–property measurements is given in Table 2. Aging time and temperature for cast materials for the various mechanical tests are given in Tables 3 and 4.

2.2 Material Characterization

The various cast materials were characterized to determine their chemical composition, hardness, grain structure, and ferrite content and distribution. All castings were examined in the three orientations as well as at different locations, namely, material near the center and near the inner and outer surfaces of the pipes, and top and bottom regions of the keel blocks and slabs. A ferrite scope was used to measure the ferrite content of the castings. The instrument was calibrated with several weld metal standards (ferrite numbers between 2.4 and 28.1) obtained from the British Welding Institute. The distribution of ferrite was determined by means of the intercept method, i.e., by counting the number of ferrite/austenite phase boundaries intersected by a superimposed outline. Measurements were made along a circular outline to minimize the standard deviation

Table 2. Test Matrix for the Cast Stainless Steel Specimens

Material	Microstructural Characterization	Charpy Impact	Tensile Tests	DBTT	J_R Curve
GF specimens	x	–	–	–	
In–service components	x	x	x	x	x
Large heats[b]	x	x	x	x	x
Commercial heats[b]	x	x	x	x	x
Small heats[b]	x	x	–	–	–

[a] Characterization of chemical composition, ferrite content, and grain size and structure.
[b] Tests will be performed after thermal aging.

Table 3. Aging Time and Temperature for Cast Materials Used in Charpy–Impact, Tensile, and J–R Curve Tests

	Temperature (°C)				
Time (h)	450	400	350	320	290
100	a	a	–	–	–
300	a	a	a	–	–
1,000	a	a	a	a	–
3,000	a	a	a,b	a	a
10,000	a	a,b	a,b,c	a,b	a
30,000	a	a	a,b,c	a,b,c	a,b,c
>50,000	–	a	a	a,b	a,b

[a] Charpy–impact tests on small experimental and commercial heats.
[b] J–R curve tests at room temperature and 290°C on commercial heats.
[c] Charpy–impact tests to obtain transition curves for commercial heats

Table 4. Aging Time and Temperature for Materials from Cast Slabs Used in Charpy–Impact, Tensile, and J–R Curve Tests

	Temperature (°C)				
Time (h)	450	400	350	320	290
3,000	a	a	a	–	–
10,000	–	a	a,b	a,b	–
30,000	–	–	a,b	a,b	a,b
50,000	–	–	b	a,b	–

[a] Charpy–impact tests.
[b] Tensile and J–R curve tests.

of the analysis. The average number of intersections per unit length, N_L is given by NM/L, where N is the number of intersections on a test figure (i.e., a circle) of total length L, applied to a field view of magnification M. The ferrite/austenite phase boundary area per unit volume is expressed as $Sv = 2 N_L$ and the average linear intercept between ferrite is expressed as $\lambda = 2/\bar{N}_L$.

The hardness and the ferritic spacing and content of the various heats of cast stainless steel are given in Table 1. Some differences in hardness and ferritic content were observed for material from different locations in the castings. The ferrite content was lower and the hardness slightly higher towards the top of the static–cast keel blocks and slabs or the inner surface of the centrifugally cast pipes. This behavior appears to be related to compositional variations, particularly changes in the nickel content. In general, the hardness of the cast material increases with an increase in ferrite content. For the same ferrite content, the hardness of CF–8 and CF–8M material is comparable, whereas the hardness of CF–3 material is lower. An increase in nitrogen content increases the hardness of cast stainless steels of all grades.

The chromium and nickel equivalents for the various heats are plotted on the modified Schaeffler diagram in Fig. 3. The two–phase regimes covered by the ASTM Specification A 351 for CF–8 or CF–3 and CF–8M cast stainless steels are shown by solid and dashed

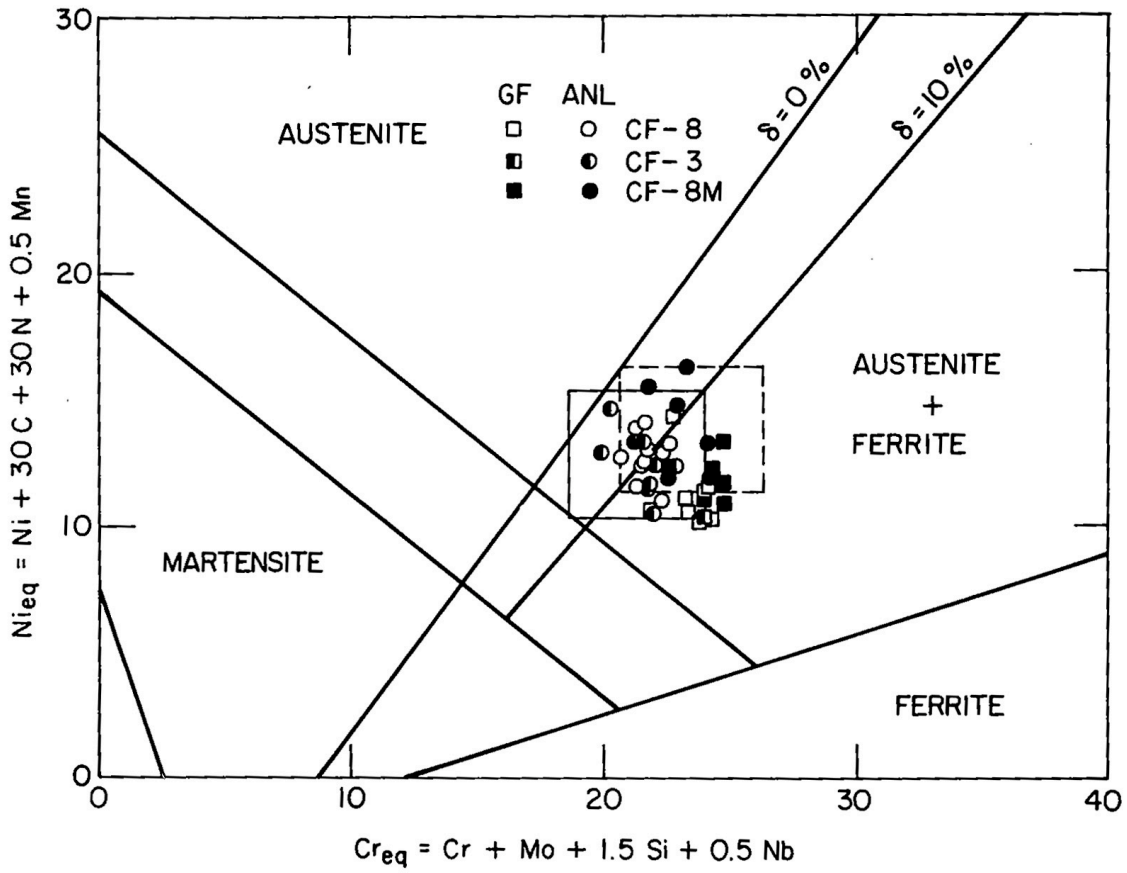

Figure 3. Schaeffler Diagram and Ferrite Content of Cast Duplex Stainless Steels in the Present Work and in the Study by Georg Fischer Company (Ref. 8).

Table 5. Ferrite Content and Grain Structure of Various Cast Stainless Steel Pipes

Heat	OD (m)	Wall (mm)	Process	Grade	Ferrite Cont. (%)[a] OD	ID	Grain Structure
C1	0.60	57.1	Static	CF–8	2.3	1.7	Banded, columnar/equiaxed radial to axial growth near ends
P1	0.89	63.5	Centr.	CF–8	27.6	19.5	Equiaxed across thickness
P3	0.58	51.6	Centr.	CF–3	2.5	0.9	Banded, radially oriented columnar one equiaxed band (~4 mm deep) near ID
P2	0.93	73.0	Centr.	CF–3	15.9	13.2	Equiaxed across thickness
P4	0.58	31.8	Centr.	CF–8M	11.1	9.8	Radially oriented columnar

[a] Ferrite content measured by Ferrite Scope, Auto Test FE, Probe Type FSP–1.

lines, respectively. The chemical compositions of the cast materials used in the GF study[8] are also included in Fig. 3. The composition and ferrite content of the Argonne National Laboratory (ANL) heats vary over the entire range represented by ASTM Specification A 351. The cast materials used in the GF study have a high ferrite content and the compositions of most of the materials are outside the ASTM Specifications, i.e., either the chromium content is >21 wt.% or the nickel content is <8 wt.% for CF–8 steel and <9 wt.% for CF–8M steel. Combined data from the two studies can be used to establish the effects of compositional variables on the embrittlement behavior of cast stainless steels.

The grain structures of the different castings were examined along the axial, circumferential, and radial sections. The structures observed in the four centrifugally cast pipe sections and the pump casing ring are given in Table 5. Two castings, Heats P1 and P2, contain equiaxed grains across the entire thickness of the pipe. The grain size and distribution are not significantly different in different orientations, Fig. 4. The equiaxed grains were probably produced intentionally by a low pouring temperature or by shear between the

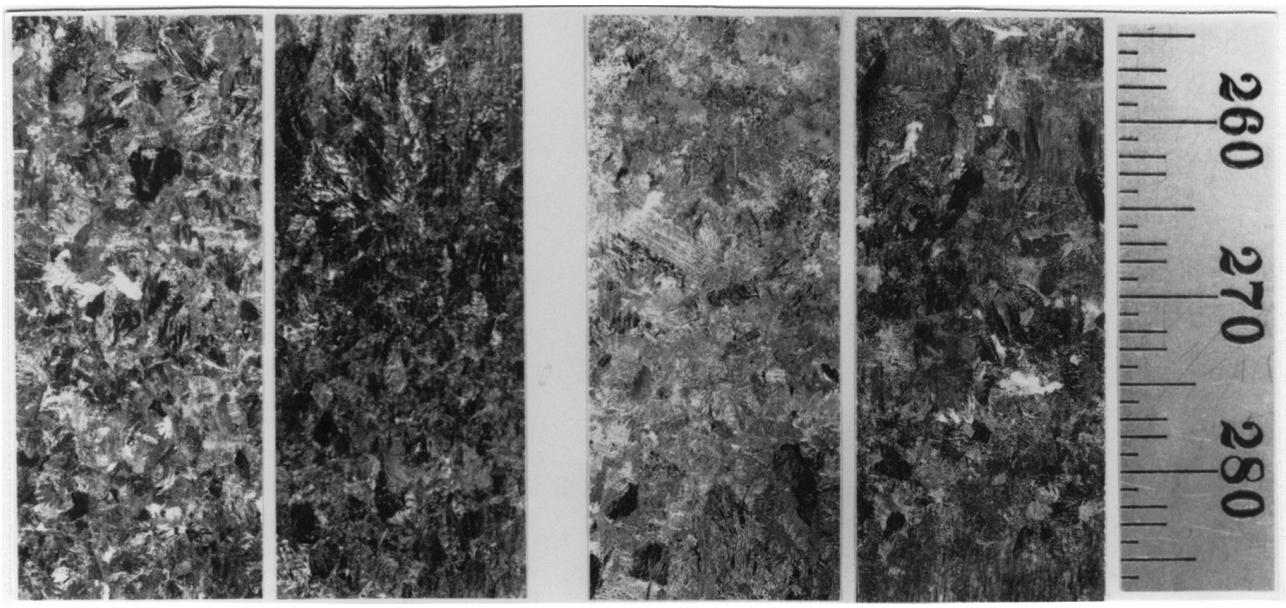

Figure 4. Grain Structure along the (a) Axial and (b) Circumferential Sections of Centrifugally Cast Pipes P1 and P2.

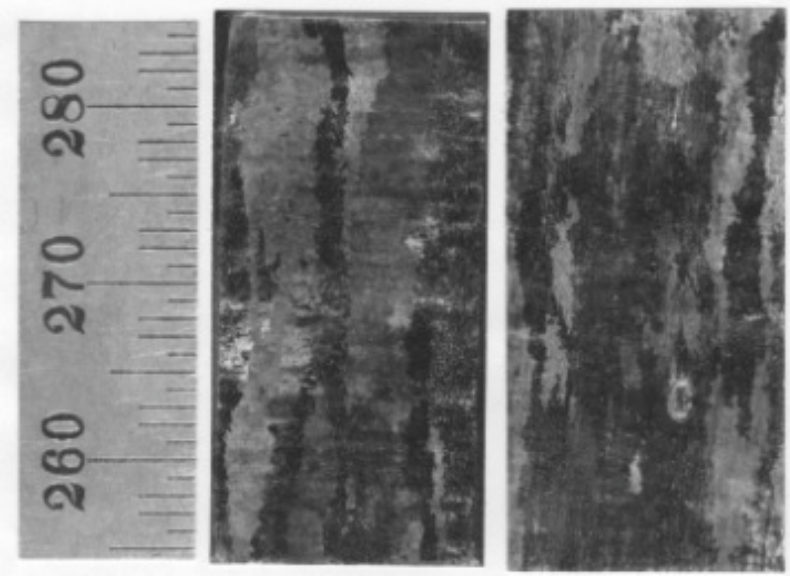

Figure 5. Grain Structure along the (a) Axial and (b) Circumferential Sections of Centrifugally Cast Pipe P4.

liquid and solid; the shear could cause dendrite arms to break and disperse in the liquid–solid region. The other two centrifugally cast pipes, Heats P3 and P4, show radially oriented columnar grains, Fig. 5. Pipe section P3 also contained a band of small equiaxed grains near the inner surface. This band was relatively thin, i.e., ~4–mm deep, and probably formed accidentally.

The static–cast keel blocks, slabs, and the pump casing ring showed a mixed structure of columnar and equiaxed grains. The grain structures of the cast slabs are shown in Fig. 6. A change from horizontal to vertical growth of the columnar grains was observed near the edges of the keel blocks and cast slabs, e.g., Heat 73. The size of the equiaxed grains in the mixed structure is generally smaller than that of the columnar grains.

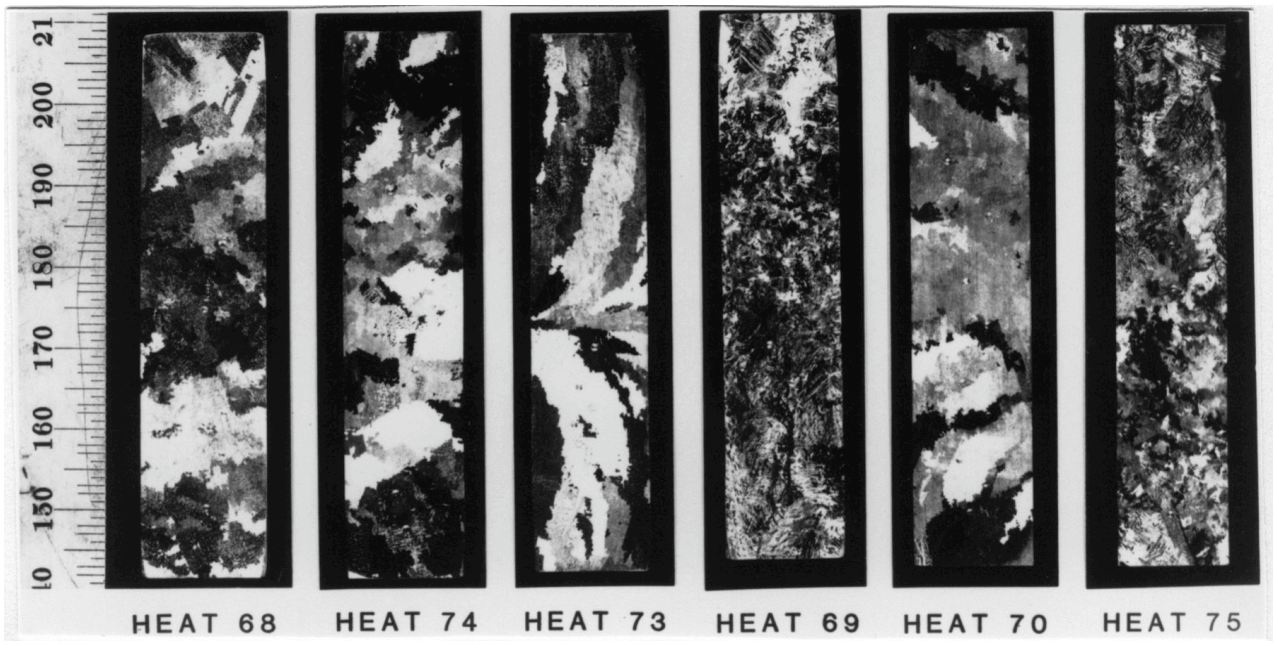

Figure 6. Grain Structure of the Various Static–Cast Slabs.

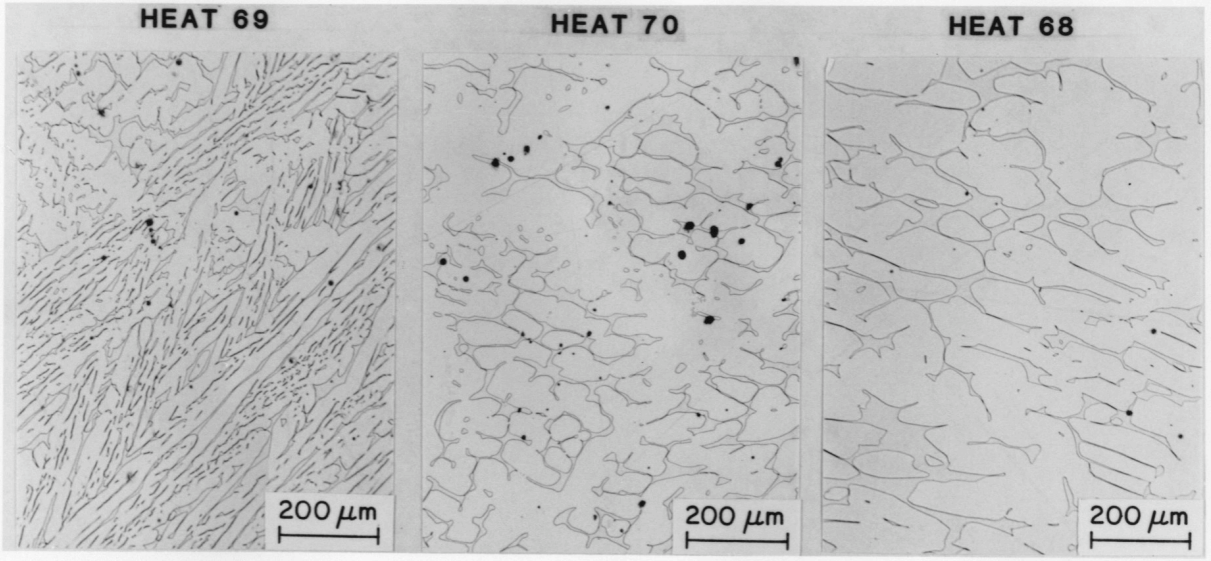

Figure 7. Ferrite Morphology for CF–3 (Heat 69), CF–8 (Heat 68), and CF–8M (Heat 70) Cast Stainless Steels.

The ferrite morphology of the various materials varied with the ferrite content, chemical composition, and size of the casting. The ferrite morphology was globular for materials containing <5% ferrite. Some differences in morphology were observed between the different grades of cast stainless steel containing >5% ferrite. The CF–8 and CF–8M steels had a lacy morphology, i.e., an interlaced network of ferrite islands, while the CF–3 cast steel showed a mixture of lacy and acicular ferrite. The acicular morphology is characterized by fine needle–like ferrite that is distributed in the austenite matrix. All morphologies had a random arrangement within the casting. The ferrite morphologies of the various cast materials are given in Appendix A. Typical microstructures for the static–cast slabs and pump impeller and centrifugally cast pipes are shown in Figs. 7 and 8.

The mean ferrite intercept for the cast materials is plotted as a function of the measured ferrite content in Fig. 9. The mean ferrite intercept for the keel blocks decreases with an increase in ferrite content, e.g., the mean ferrite intercept decreases from >150 μm for a material with ~4% ferrite to ~45 μm for cast material with ~25% ferrite. However, the ferrite distribution in centrifugally cast pipes or the slabs does not show any correlation with the ferrite content. For the same ferrite content, the mean ferrite intercepts for the cast pipes and slabs are generally larger than for the keel blocks. The mechanical–property data for materials with different mean ferrite intercepts but the same ferrite content will be used to establish the influence of ferrite distribution on the embrittlement behavior of cast duplex stainless steel.

2.3 Mechanical Tests

The specimen blanks for mechanical tests were obtained from the various experimental and commercial heats of cast stainless steel. The orientation and location of the specimens from pipe sections, slabs, keel blocks, and the KRB pump cover plate are shown in Figs. 10 and 11. The test specimens were machined from the blanks after thermal aging. The configuration of the Charpy–impact, tensile, and compact–tension (CT) test specimens is

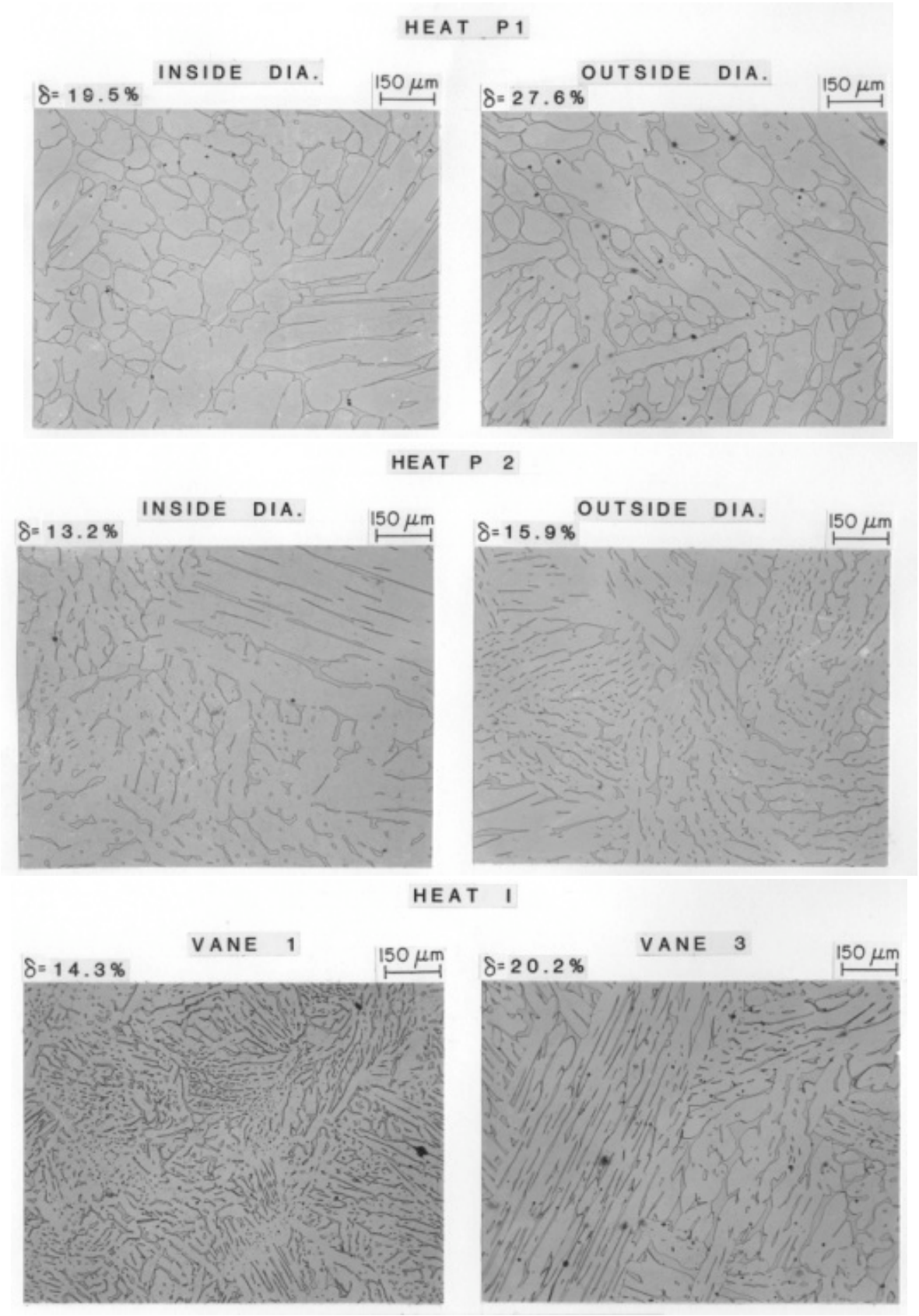

Figure 8. Ferrite Morphology for the Centrifugally Cast Pipes (Heats P1 and P2) and the Pump Impeller (Heat I).

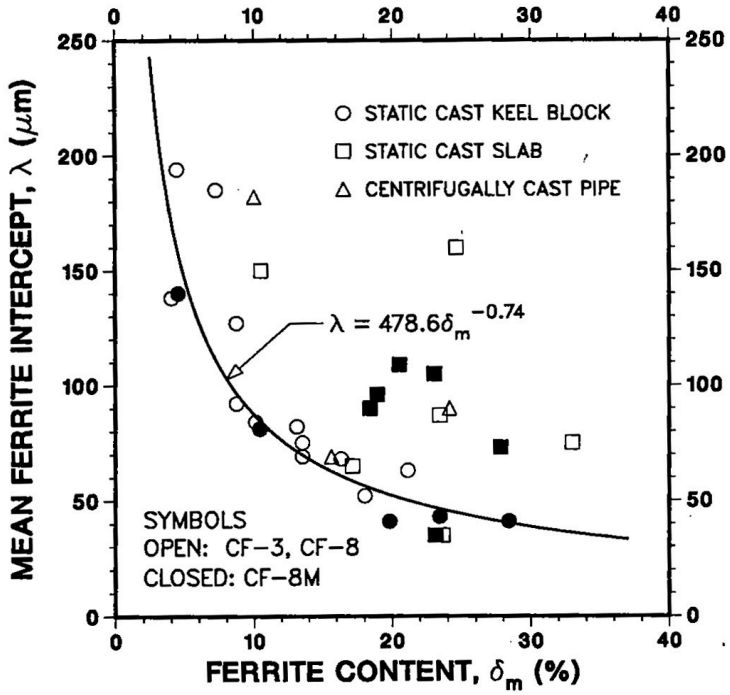

Figure 9.
Mean Ferrite Intercept vs Ferrite Content for the Various Heats of Cast Stainless Steel.

shown in Fig. 12. Tensile and J–R curve tests were also conducted by Materials Engineering Associates (MEA), under subcontract to ANL. The experimental details and results from these tests are presented elsewhere.[25]

2.3.1 Charpy Tests

A Dynatup Model 8000A drop–weight impact machine with an instrumented tup and data readout system was used for the Charpy–impact tests. The available energy and impact velocity of the machine can be varied by altering the weight of the crosshead and the drop height; the maximum energy and velocity obtainable with the machine were 1.3 kJ and 4 m/s, respectively. Load– and energy–time data were obtained from an instrumented tup and recorded on a dual–beam storage oscilliscope. The instrumented tup consists of a striking head and a strain gauge with a four–arm semiconductor bridge circuit. The strain gauge, which measures the compressive load on the tup during the test, was calibrated by a dynamic loading technique. The initial and final velocities of the tup were measured optically. The load–time traces from each test were digitized and stored on a floppy disk for analysis. The total energy was computed from the load–time trace; the value was corrected for the effects of tup velocity.

The instrumented tup and data readout instrumentation were periodically calibrated by fracturing standard V–notch specimens fabricated from 6061–T6 aluminum and 4340 steel with a hardness of Rockwell R_C 54. The amplifier gain was adjusted from the load– and energy–time traces for the aluminum specimen so that the recorded load limit coincided with the load limit for the material (i.e., 7.74 kN). The linearity of the calibration was established from the results for the 4340 steel specimen, which has a higher limit load.

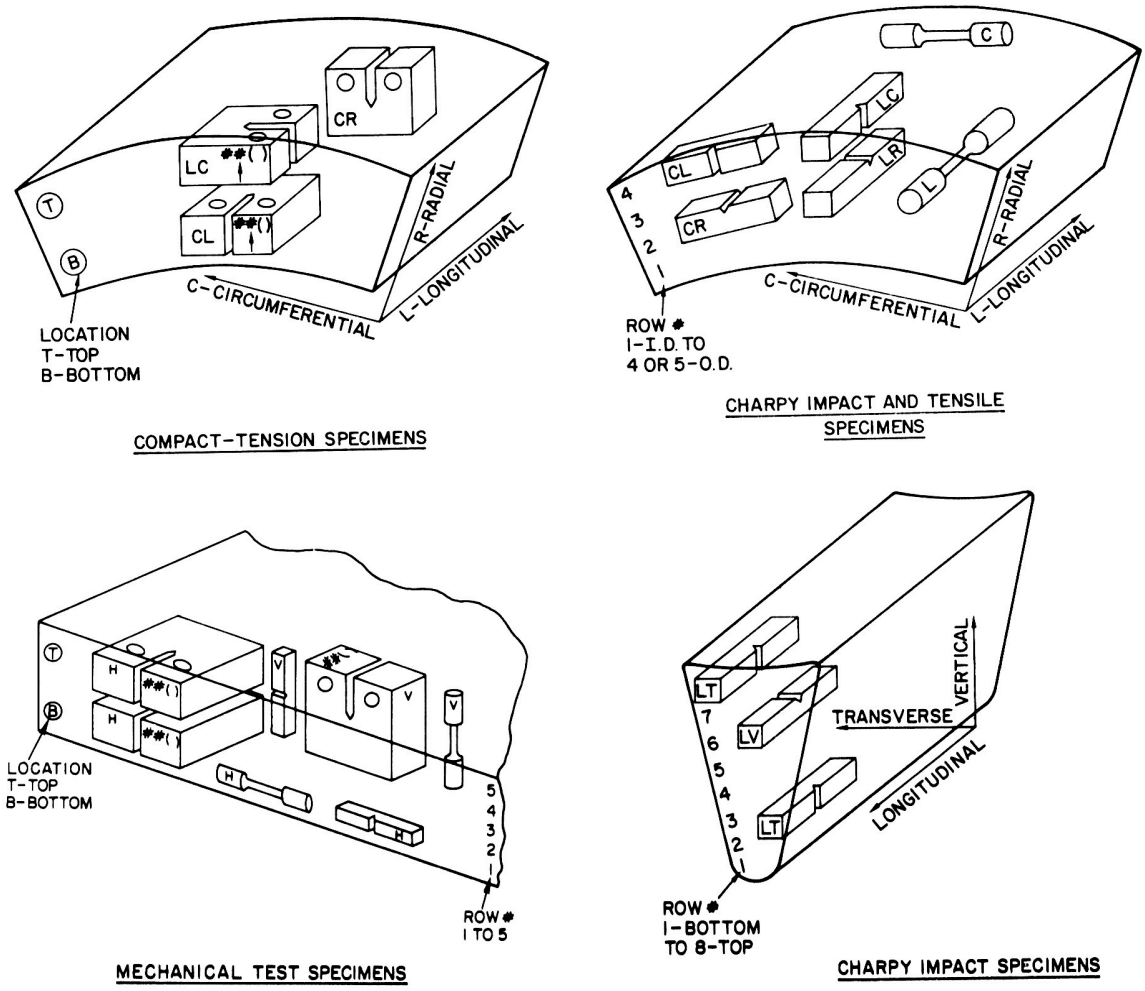

Figure 10. Orientation and Location of the Mechanical–Test Specimens Taken from (a) and (b) Pipe Sections, (c) Slabs, and (d) Keel Blocks.

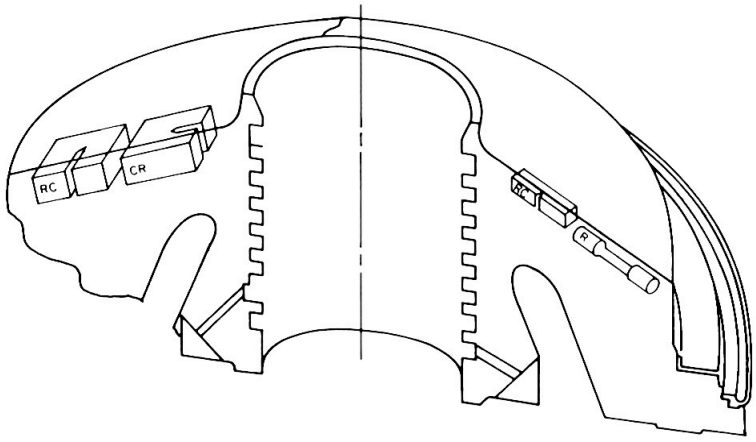

Figure 11. Orientation and Location of the Mechanical–Test Specimens Taken from the KRB Reactor Pump Cover Plate.

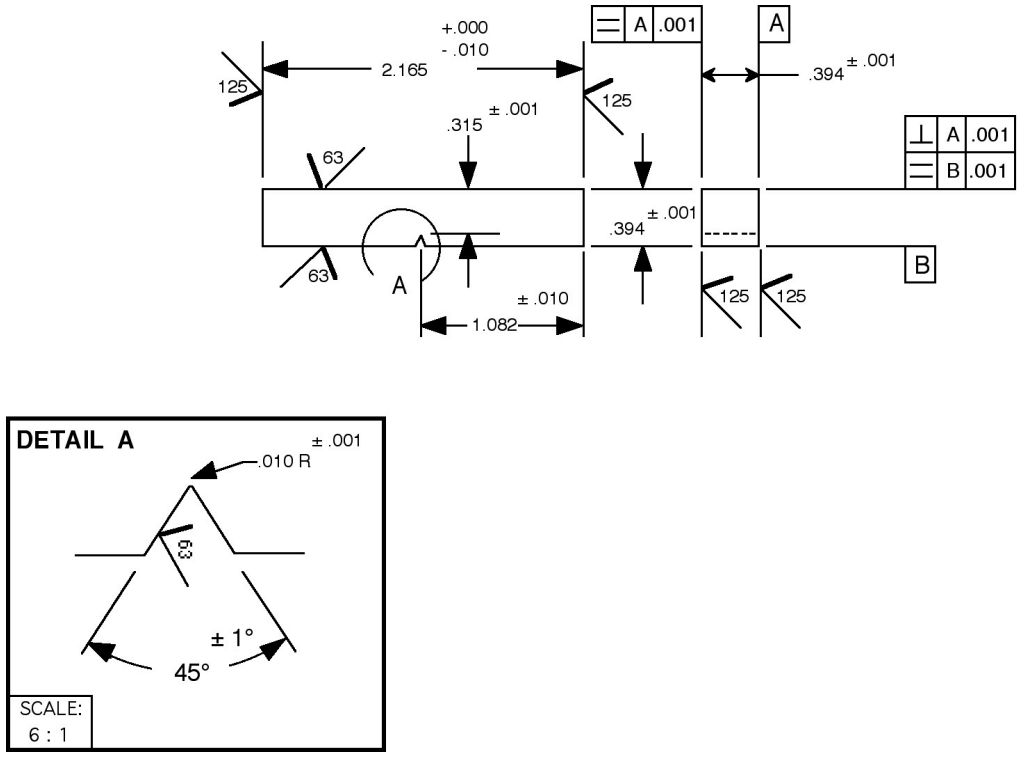

(a)

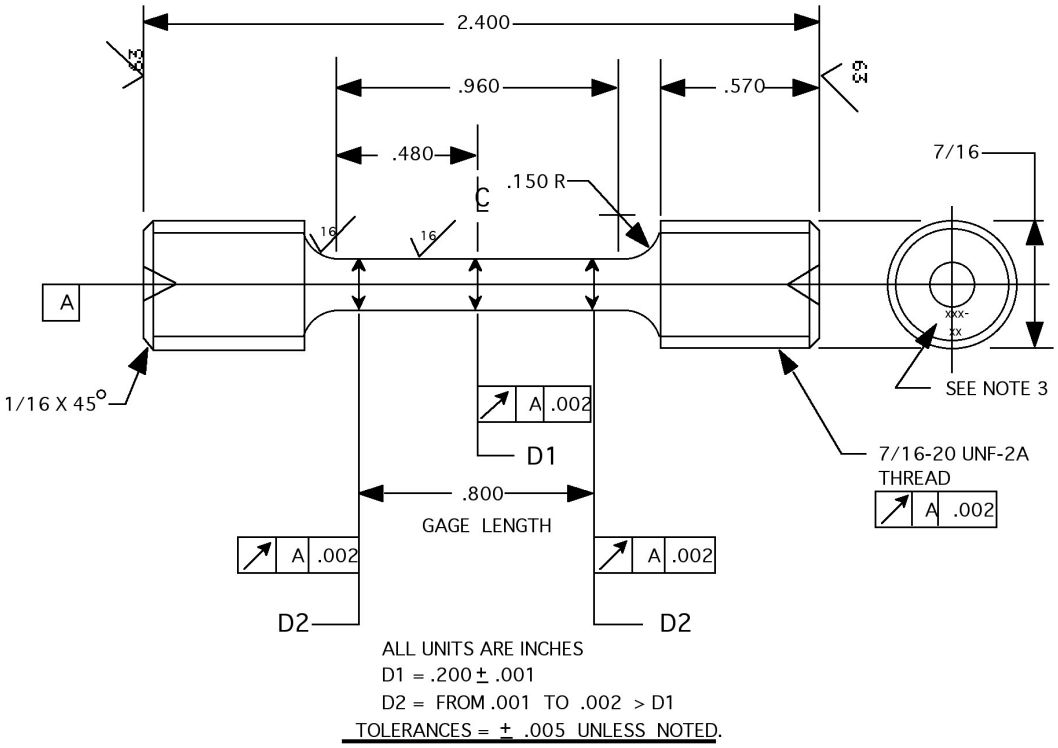

(b)

Figure 12. Mechanical Test Specimens (a) Charpy Impact, (b) Tensile, and (c) Compact Tension.

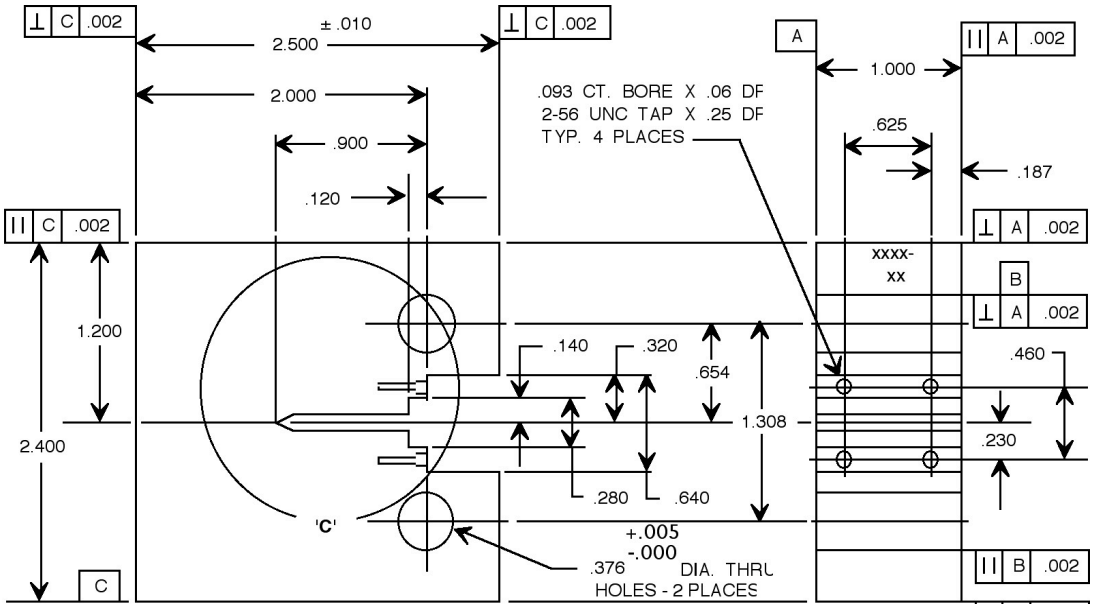

(c)

Figure 12. (Contd.)

The specimens for high–temperature tests were heated by resistance heating. Pneumatic clamps were used to make electrical connection and hold the specimens in position on the anvils. The anvils were electrically insulated from the base plate. The power to the specimen was interrupted immediately before impact to release the clamps and remove any constraint on the specimen. The temperature was monitored and controlled by a thermocouple attached to the specimen. The specimens for the low–temperature tests were cooled in either a refrigerated bath or liquid nitrogen.

2.3.2 Tensile Tests

Tensile tests were performed according to ASTM Specification E 8 and E 21 in an Instron tensile test machine with a maximum loading capacity of 90 kN (20 kips). Cylindrical specimens with a diameter of 5.08 mm (0.2 in.) and a gauge length of 20.3 mm (0.8 in.) were used for all the tests. An axial extensometer, with an initial gauge length of 20.3 mm (0.8 in.), was used for continuous measurement of strain during room temperature tests. An IBM computer was used to digitize load, crosshead movement, and axial displacement data and to store the data on floppy disks. Analog traces of load–vs–crosshead displacement and load–vs–extensometer displacement were also obtained for each test.

The true stress–strain data were calculated up to the maximum load using the constant volume criterion, which assumes a homogeneous distribution of strain along the gauge length. However, most specimens showed inhomogeneous deformation because of the relatively large grain structure. The specimen surfaces along the gauge length were irregular, and the fracture cross sections were often elliptical. These factors create some uncertainty in the true stress–strain data. The strain at fracture, i.e., total elongation, was determined from extensometer displacements. Total elongation was also measured from crosshead displacements; the values obtained from extensometer were ~64% of the values determined from crosshead displacement.

The tests at 290°C (~550°F) were conducted in a forced–air recirculating furnace. Thermocouples were mounted above and below the specimen gauge length to monitor and control the temperature within ±2°C. An axial extensometer was not used for the elevated temperature tests and the total elongation was determined from the crosshead displacement multiplied by 0.64.

2.3.3 Fracture Toughness Tests

The J–R curve tests were conducted according to ASTM Specification E 813 Rev. 85 and E 1152. Compact–tension specimens, 25.4 mm (1 in.) thick (i.e., 1T size) were used for the tests. The CT specimen design of ASTM Specification E–399 was modified to permit measurement of load–line displacement by axial extensometer. The extensometer was mounted on razor blades that were screwed onto the specimen along the load line.

Prior to testing, the specimens were fatigue–precracked at room temperature and at load levels within the linear elastic range. The final ratio of crack length to width (a/W) after precracking was ~0.55. The final 1–mm (~0.04–in.) crack extension was carried out at a load range of 13 kN (2.92 kip) to 1.3 kN (0.292 kip), i.e., during precracking K_{max} was <25 MPa·m$^{1/2}$ (22.6 ksi·in.$^{1/2}$). After precracking, all specimens were side–grooved by 20% of the total specimen thickness, i.e., 10% per side.

The J–R curve tests were performed on an Instron testing machine with 90 kN (20 kip) maximum load capacity. The load and load–line displacement data were digitized with digital voltmeters and stored on a disk for posttest analysis and correction of the test data. The single–specimen compliance procedure was used to estimate the crack extension. Rotation and modulus corrections were applied to the compliance data. Both deformation theory and modified forms of the J integral were evaluated for each test.

After each test, the specimen was heated to 350°C to heat–tint the exposed fracture surface. The specimen was then fractured at liquid nitrogen temperature. The initial (i.e., fatigue precrack) and final (test) crack lengths were measured optically for both halves of the fractured specimen. The crack lengths were determined by the 9/8 averaging technique, i.e., the two near–surface measurements were averaged and the resultant value averaged with the remaining seven measurements.

The fracture toughness J_{IC} values were determined in accordance with ASTM Specification 813–81 and E 813–85. For the former, J_{IC} is defined as the intersection of the blunting line given by $J = 2\sigma_f\Delta a$, and the linear fit of the J–vs–Δa test data between the 0.15–mm and 1.5–mm exclusion lines. The flow stress, σ_f, is the average of the 0.2% yield stress and the ultimate stress. The ASTM Specification E 813–85 procedure defines J_{IC} as the intersection of the 0.2–mm offset line with the power law–fit (of the form $J = C\Delta a^n$) of the test data between the exclusion lines. J–R curve tests on cast stainless steels indicate that a slope of four times the flow stress ($4\sigma_f$) for the blunting line expresses the J *vs* Δa data better than the slope of $2\sigma_f$ defined in E 813–81 or E 813–85. The fracture toughness J_{IC} values were determined using the $4\sigma_f$ slope. The J_{IC} values were also determined by the procedure used by MEA;[25] where J_{IC} is determined from the intersection of the power law curve with the 0.15–mm offset line. These values of J_{IC} are comparable to the ASTM Specification E 813–81 values.

The tearing modulus was also evaluated for each test. The tearing modulus is given by $T = E(dJ/da)/\sigma_f^2$, where E is the Young's modulus and σ_f is the flow stress. The ASTM E 813–81 value of tearing modulus is determined from the slope dJ/da of the linear fit to the J–vs–Δa data. For the power law curve fits, an average value of dJ/da was calculated[26] to obtain average tearing modulus.

The various validity criteria specified in ASTM Specification E 813 for J_{IC} and in ASTM Specification E 1152 for J–R curve, were used to qualify the results from each test. For the present investigation, most of the unaged or short–term–aged specimens yielded invalid J_{IC} values because of the relatively high toughness of the material.

3 Mechanical Properties

3.1 Charpy–Impact Energy

The results from Charpy–impact tests on the various experimental and commercial heats, aged up to 30,000 h at 290, 320, 350, 400, and 450°C, are tabulated in Appendix B. The data for room temperature impact energy were analyzed to determine the kinetics and extent of embrittlement. The variation of the Charpy–impact energy KCV with time can be expressed as

$$KCV = K_m + \beta\{1 - \tanh [(P - \theta)/\alpha]\}, \quad (3)$$

where P is the aging parameter defined in Eq. (1), K_m is the minimum impact energy reached after long–term aging, β is half the maximum decrease in impact energy (i.e., half the difference between initial and minimum impact energy), θ is the log of the time to achieve β reduction in impact energy, and α is a shape factor.

The values of the constants in Eqs. (1) and (3) for various heats of cast stainless steel are given in Table 6 and the best–fit curves for some of the heats are shown in Figs. 13–15. In Figs. 16–18, the Charpy–impact data are plotted as a function of the aging parameter; the actual time and temperature of aging are shown on five separate axes below the figures; the service time, in years, at the hot–leg temperature of LWRs is shown at the top of the figures.

Table 6. Values of the Constants Representing the Kinetics of Embrittlement of Cast Stainless Steel

Heat	Constants				Activation Energy	
	K_m (J/cm^2)	β (J/cm^2)	θ	α	[kJ/mole	(kcal/mole)]
47	163.6	38.5	2.89	1.11	91.6	(21.90)
51	153.0	31.0	3.06	0.58	184.3	(44.06)
56	100.4	51.3	4.22	1.05	234.5	(56.05)
59	91.2	63.5	3.26	1.55	196.4	(46.94)
60	64.7	63.9	2.82	0.63	198.8	(47.51)
63	140.2	58.4	2.43	0.92	101.7	(24.30)
64	53.3	73.9	2.47	0.66	142.5	(34.06)
65	54.3	78.9	2.84	1.07	152.3	(36.39)
66	94.9	74.9	2.72	1.73	125.5	(30.23)

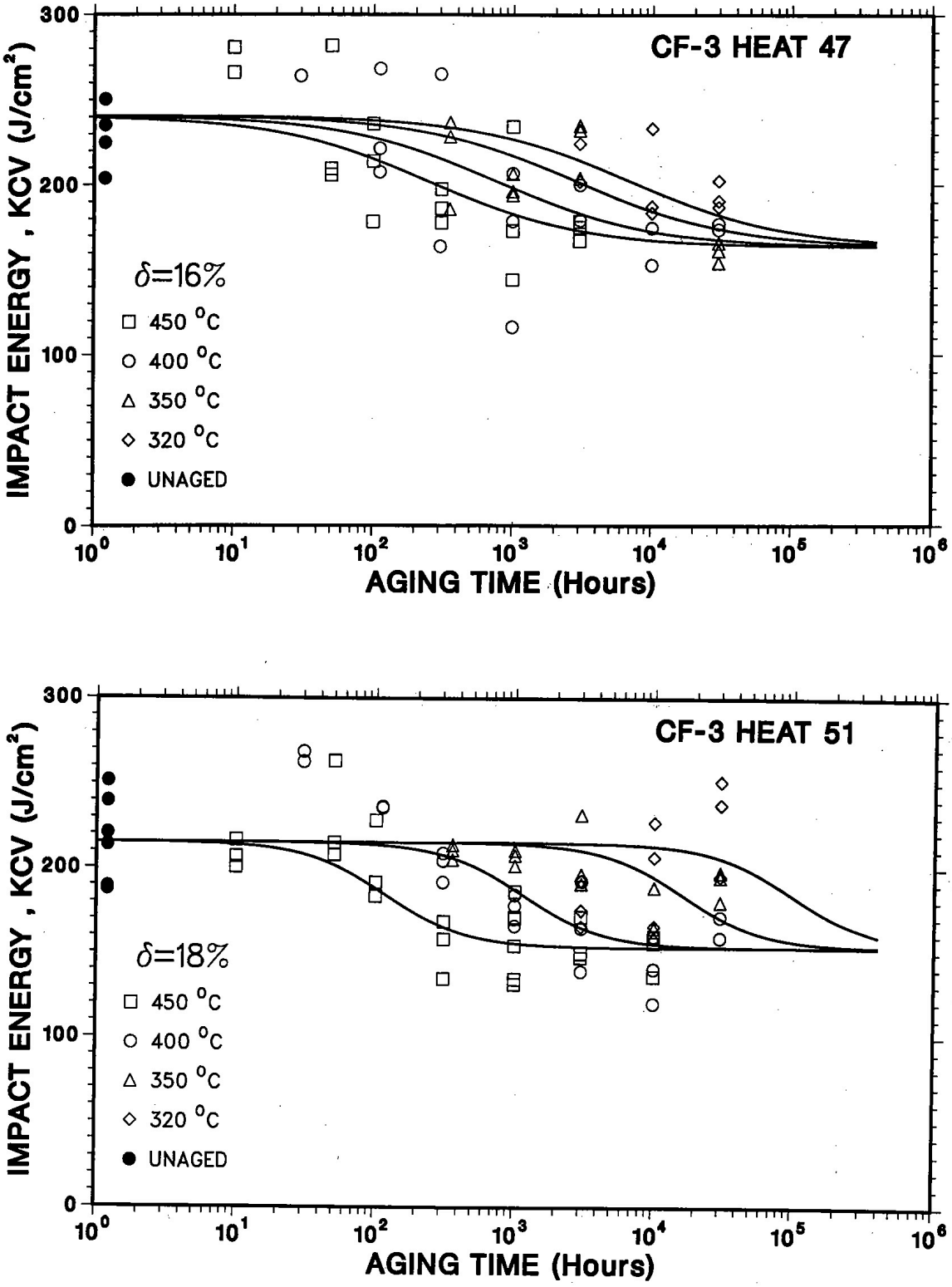

Figure 13. Effect of Aging Time and Temperature on the Room Temperature Impact Energy of CF–3 Cast Stainless Steel.

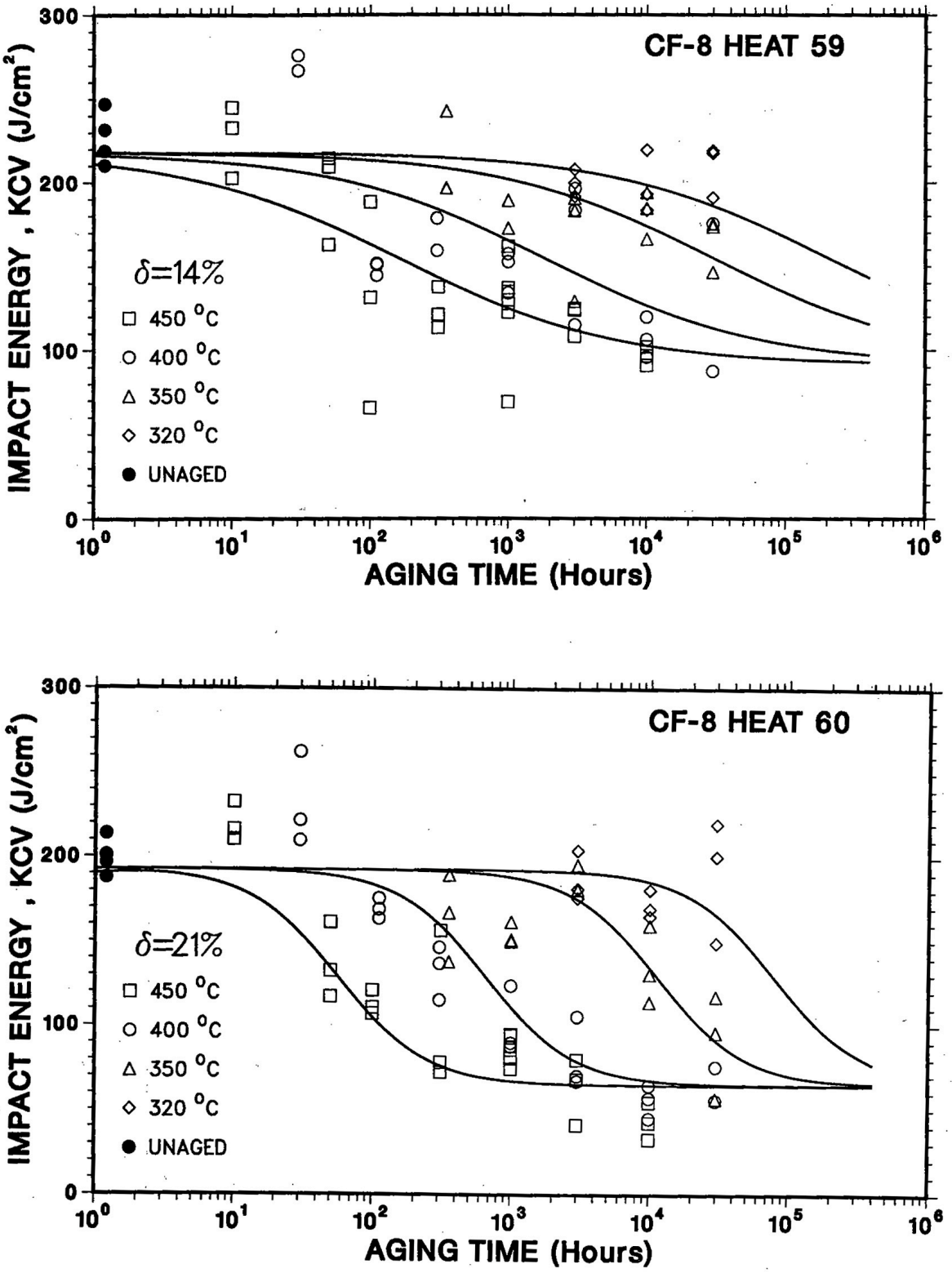

Figure 14. Effect of Aging Time and Temperature on the Room Temperature Impact Energy of CF–8 Cast Stainless Steel.

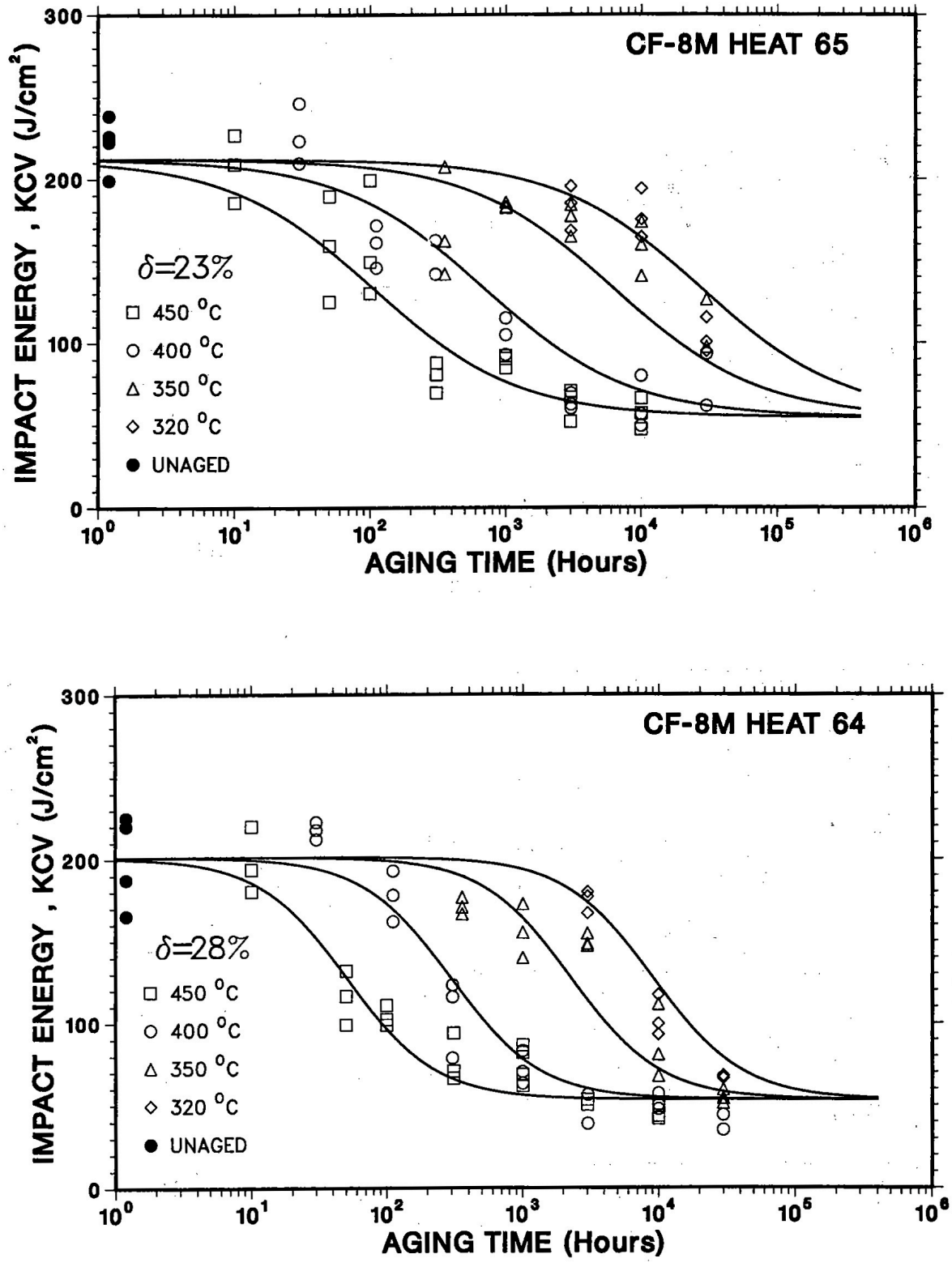

Figure 15. Effect of Aging Time and Temperature on the Room Temperature Impact Energy of CF–8M Cast Stainless Steel.

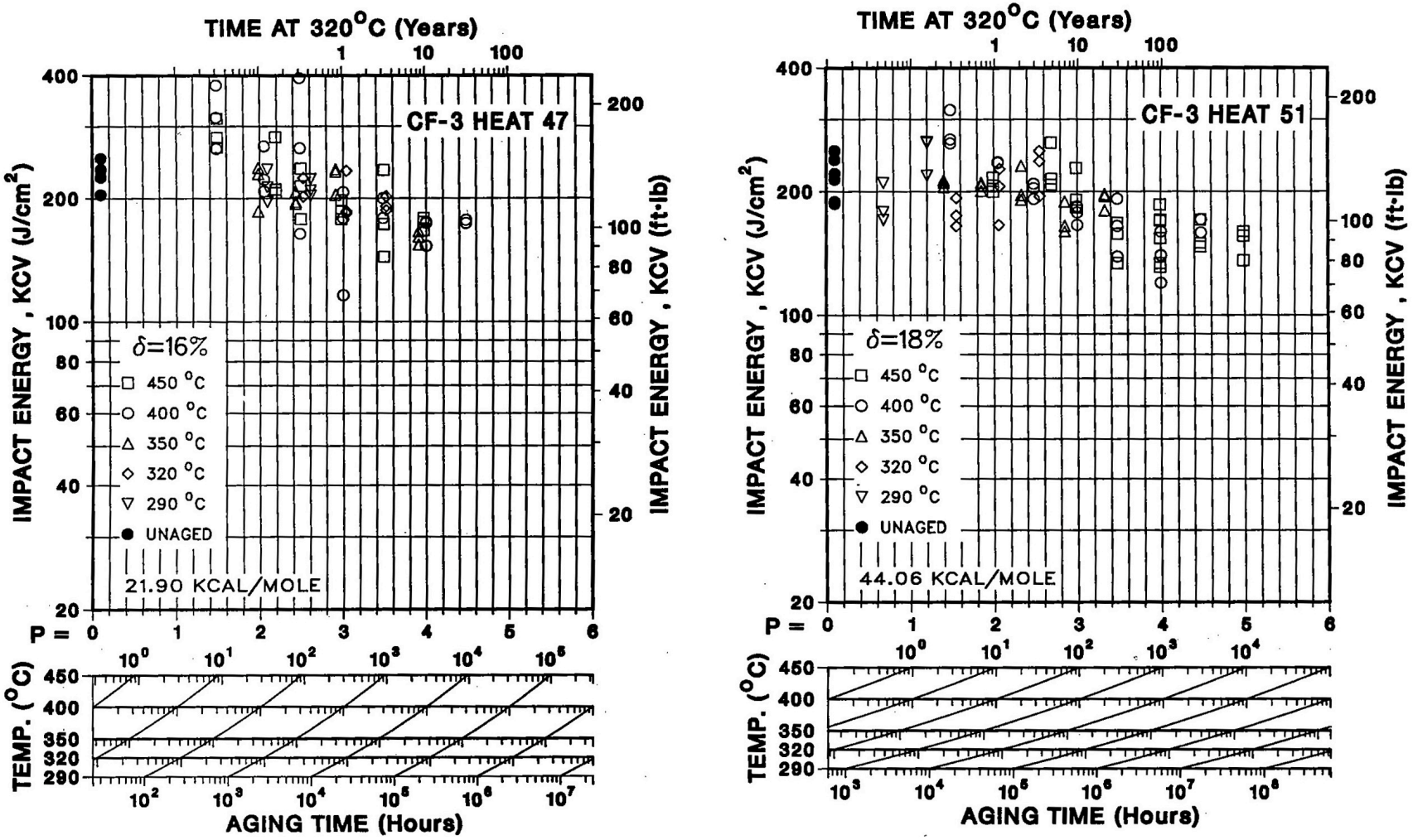

Figure 16. Influence of Thermal Aging on the Room Temperature Impact Energy of CF-3 Cast Stainless Steel.

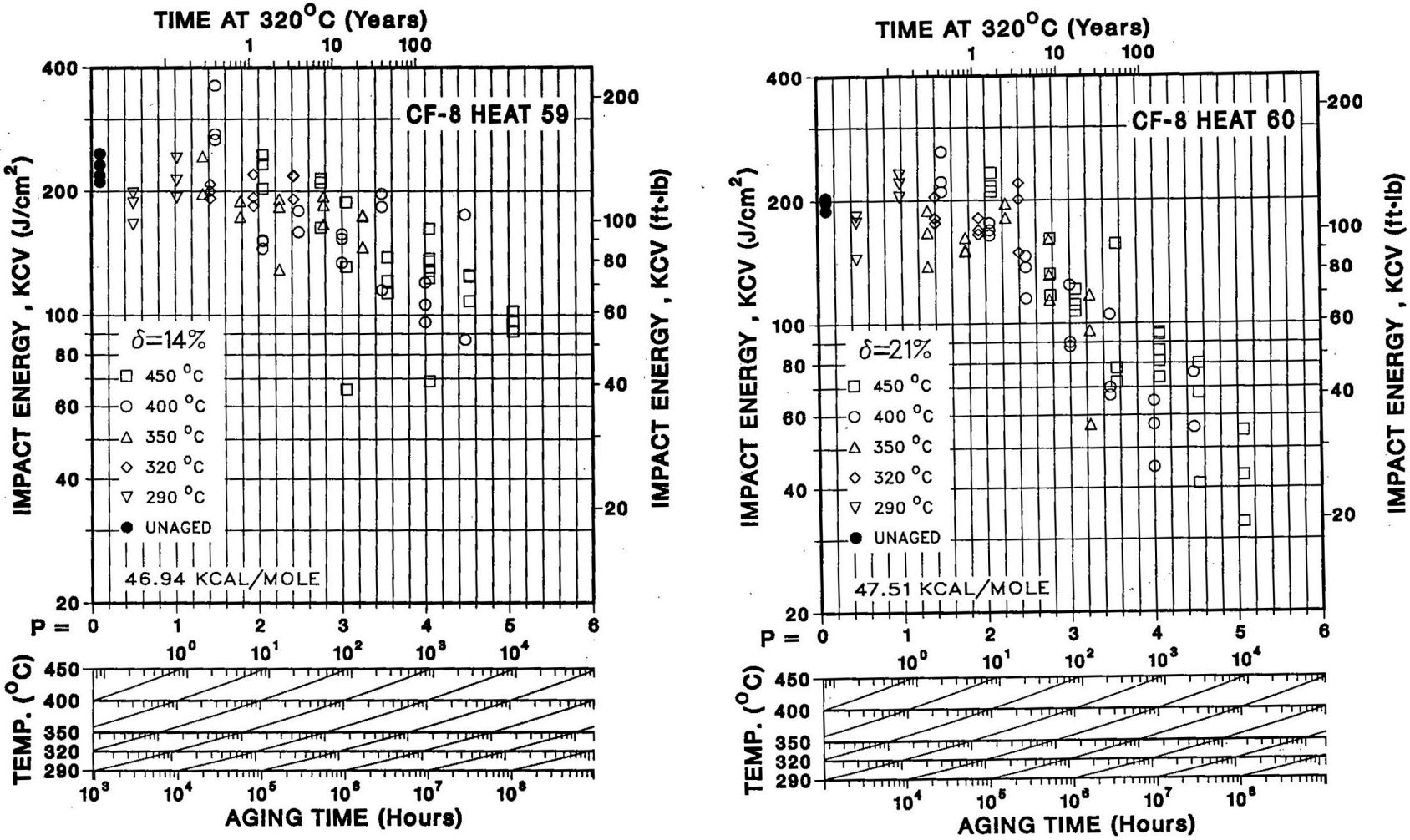

Figure 17. Influence of Thermal Aging on the Room Temperature Impact Energy of CF-8 Cast Stainless Steel.

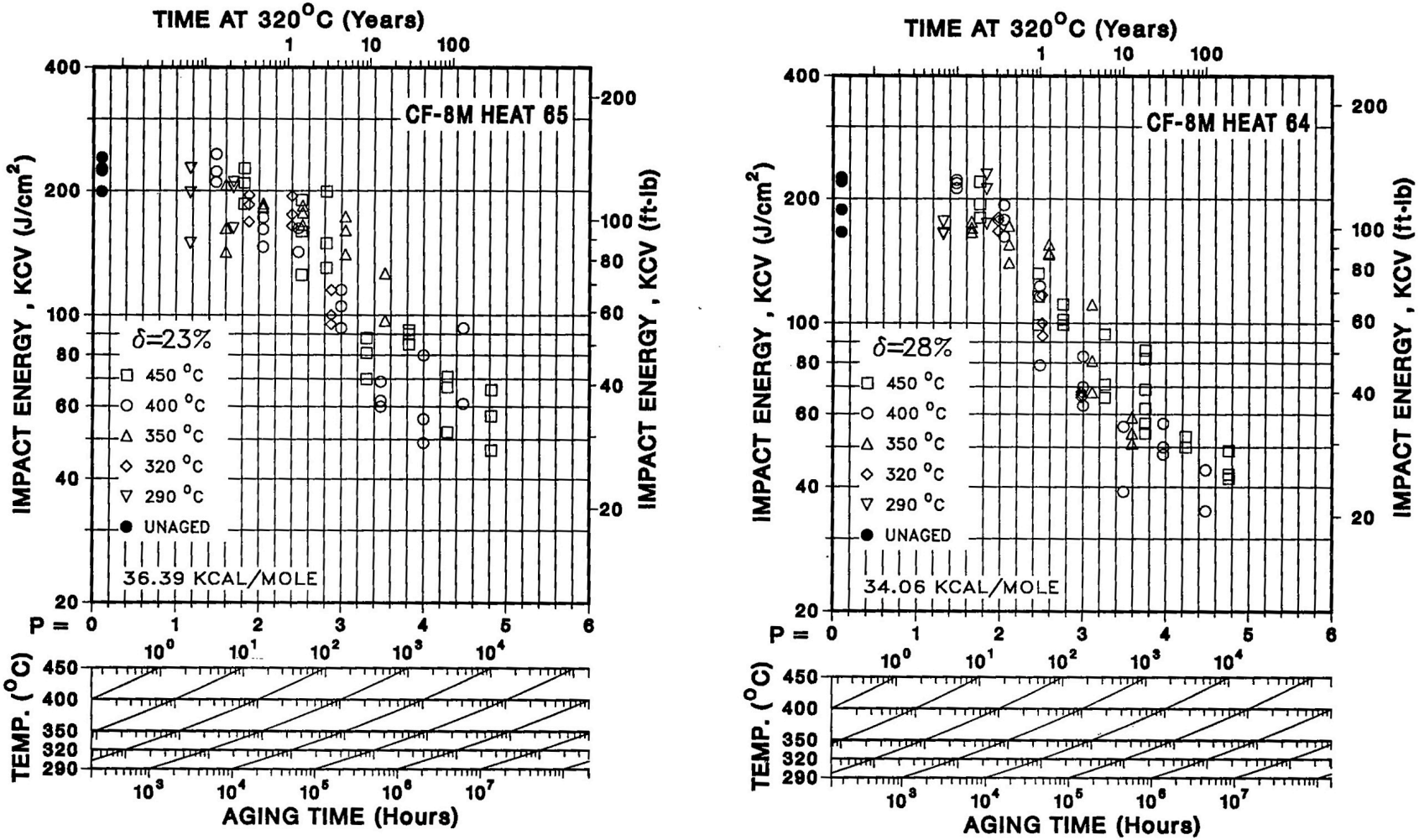

Figure 18. Influence of Thermal Aging on the Room Temperature Impact Energy of CF-8M Cast Stainless Steel.

The effects of aging temperature and time on the shifts in upper–shelf energy (USE) and transition temperature of the three grades of cast material are shown in Figs. 19–24. The impact energy data were fitted using a hyperbolic tangent function given by

$$KCV = K_o + B\{1 + \tanh[(T–C)/D]\}, \quad (4)$$

where K_o is the lower–shelf energy, T is the test temperature, B is half the distance between upper– and lower–shelf energy, C is the mid–shelf transition temperature in °C, and D is the half width of the transition region. The values of B, C, and D change with aging time whereas K_o is assumed to be unaffected by aging. The best–fit curves for the different heats are shown in Figs. 19–24 and the values of the constants are given in Table 7.

Table 7. Values of the Constants in Eq. (4) for Charpy Transition Curve of Cast Stainless Steels

Heat	Aging Condition		Constants			
	Temp. (°C)	Time (h)	K_o (J/cm^2)	B (J/cm^2)	C (°C)	D (°C)
69	Unaged	–	40	130.3	–186.8	222.7
	320	10,000		78.2	–154.1	37.8
	350	2,570		69.1	–113.2	50.4
	350	10,000		73.5	–34.6	43.5
	400	2,570		55.6	–60.7	87.4
	400	10,000		54.7	–16.9	98.0
	450	2,570		50.6	–85.0	126.5
I	Unaged	–	50	62.8	–307.9	106.2
	320	30,000		81.8	–184.0	127.9
	350	9,980		49.8	–125.4	51.7
	400	9,980		44.3	–120.9	70.4
P2	Unaged		50	162.1	–189.0	44.1
	320	30,000		172.7	–42.2	71.9
	350	10,000		148.7	–43.1	87.8
	350	30,000		157.0	–5.8	97.6
68	Unaged	–	15	138.3	–59.8	99.9
	320	10,000		97.4	–40.9	46.0
	350	5,780		78.5	–12.6	60.7
	350	10,000		97.0	28.0	67.3
	400	2,570		70.5	31.3	78.5
	400	10,000		68.6	64.0	64.3
	450	2,570		54.9	32.6	86.7
70	Unaged		15	119.7	–156.2	60.6
	350	2,570		105.6	–77.0	38.7
	350	10,000		89.2	23.6	121.7
	400	2,570		87.4	–1.7	116.2
	400	10,000		71.2	10.3	90.9
74	Unaged	–	15	89.5	–177.5	119.6
	320	10,000		91.1	–95.0	65.8
	350	2,570		89.0	–88.7	38.9
	350	10,000		71.5	–35.6	86.7
	400	2,570		61.6	–37.2	49.6
	400	10,000		65.6	19.2	123.7
	450	2,570		39.2	–47.0	63.5
75	Unaged	–	15	92.0	–156.5	43.7
	320	10,000		90.4	–16.0	37.9
	350	2,570		70.9	–10.2	105.2
	350	10,000		71.3	80.5	74.4
	400	2,570		52.7	45.5	83.1
	400	10,000		66.3	140.7	138.8
	450	2,570		34.0	20.8	99.4

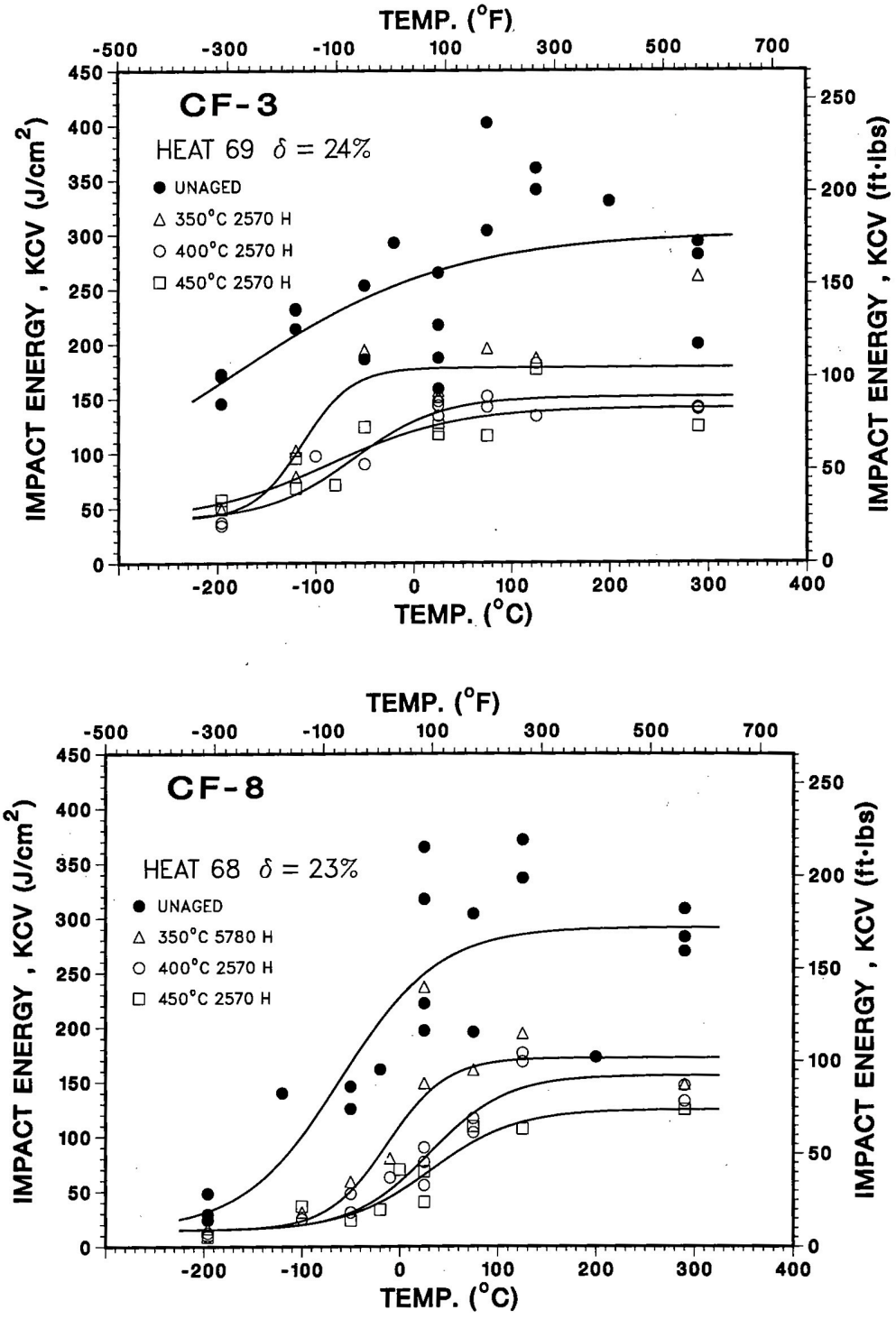

Figure 19. Effect of Aging Temperature on the Ductile–to–Brittle Transition Curves for CF-8, CF–3, and CF–8M Cast Stainless Steels Aged for ~3000 h.

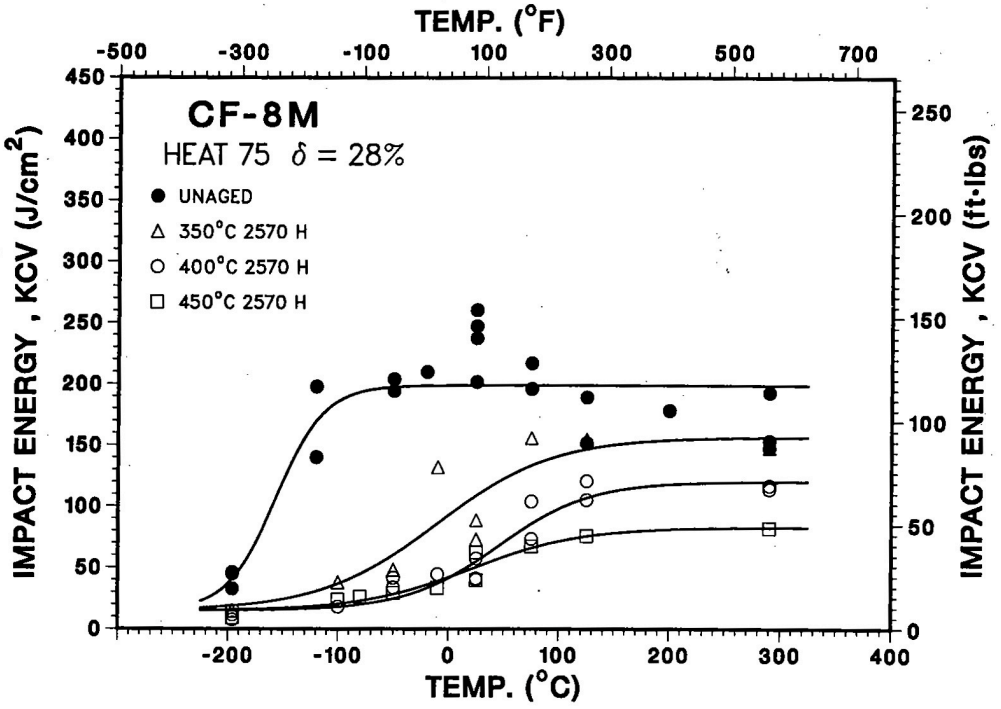

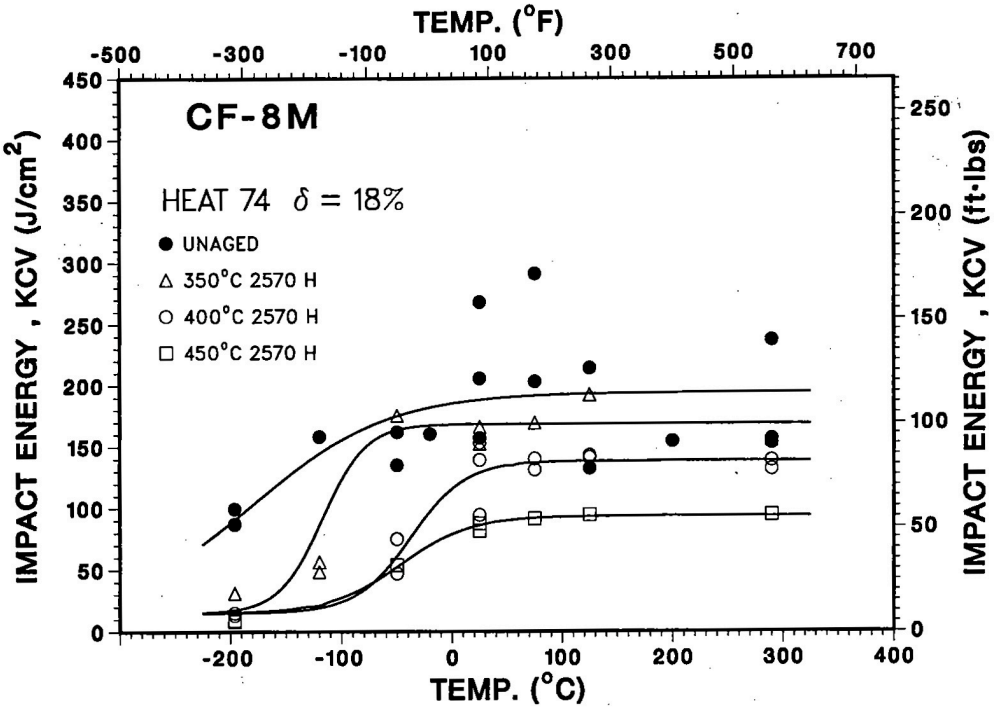

Figure 19. (Contd.)

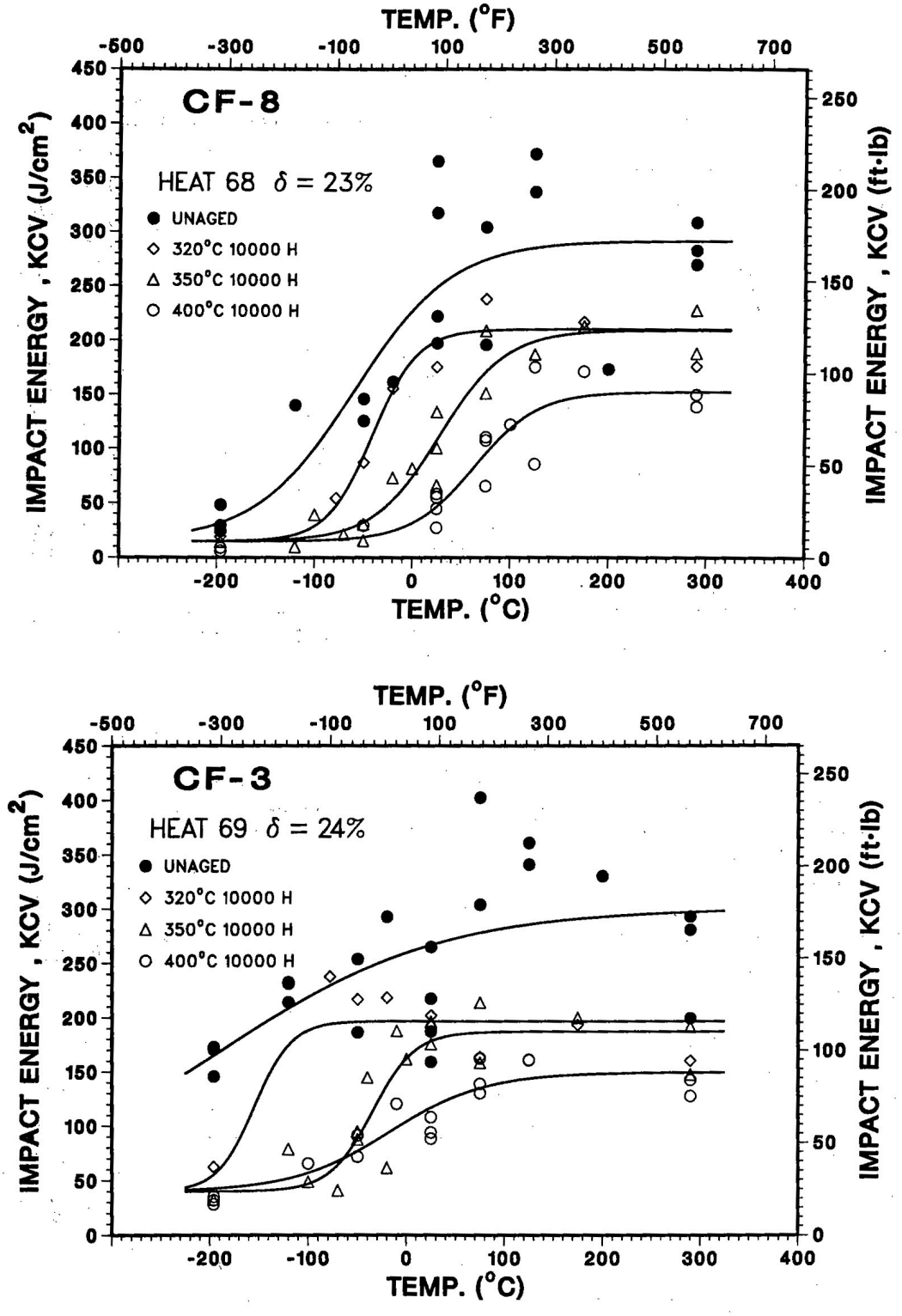

Figure 20. Effect of Aging Temperature on the Ductile–to–Brittle Transition Curves for CF-8, CF–3, and CF–8M Grades of Cast Stainless Steels Aged for 10,000 h.

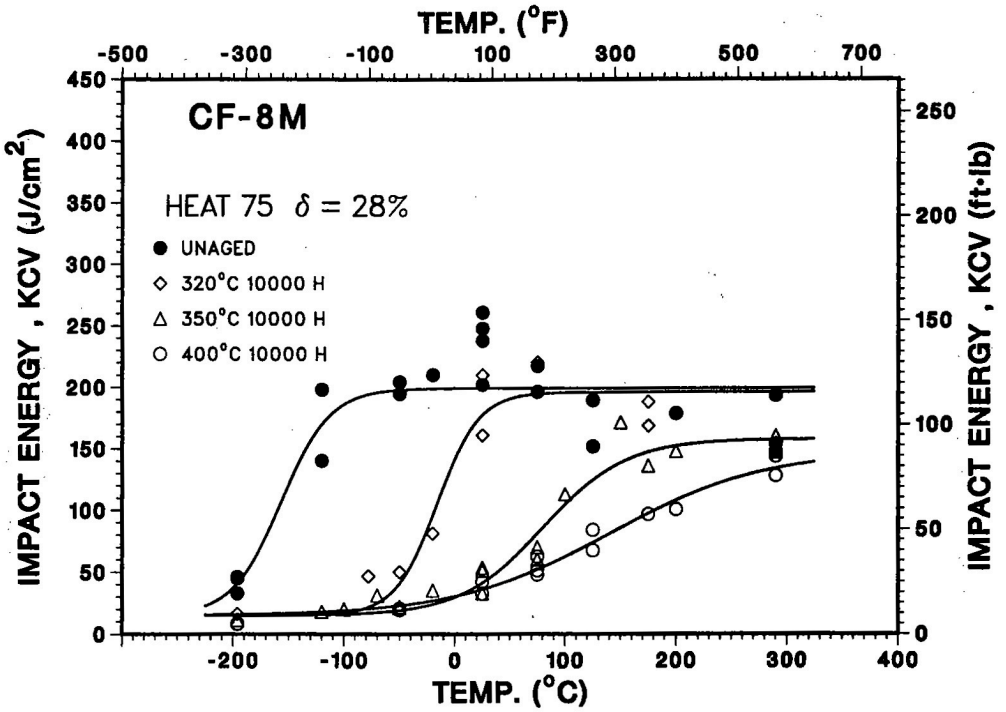

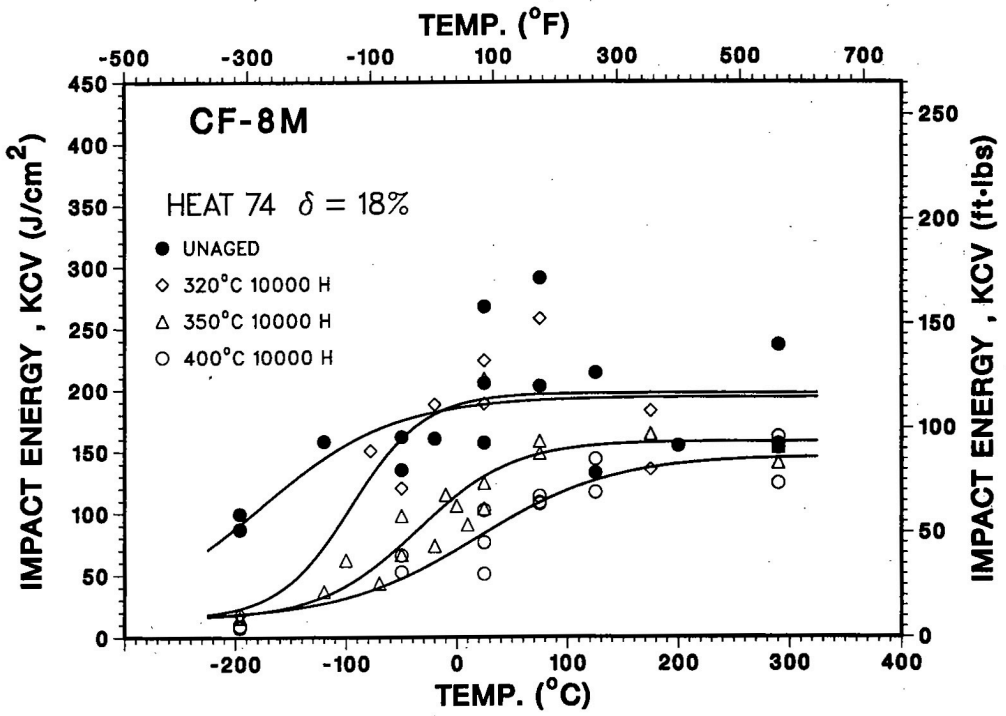

Figure 20. (Contd.)

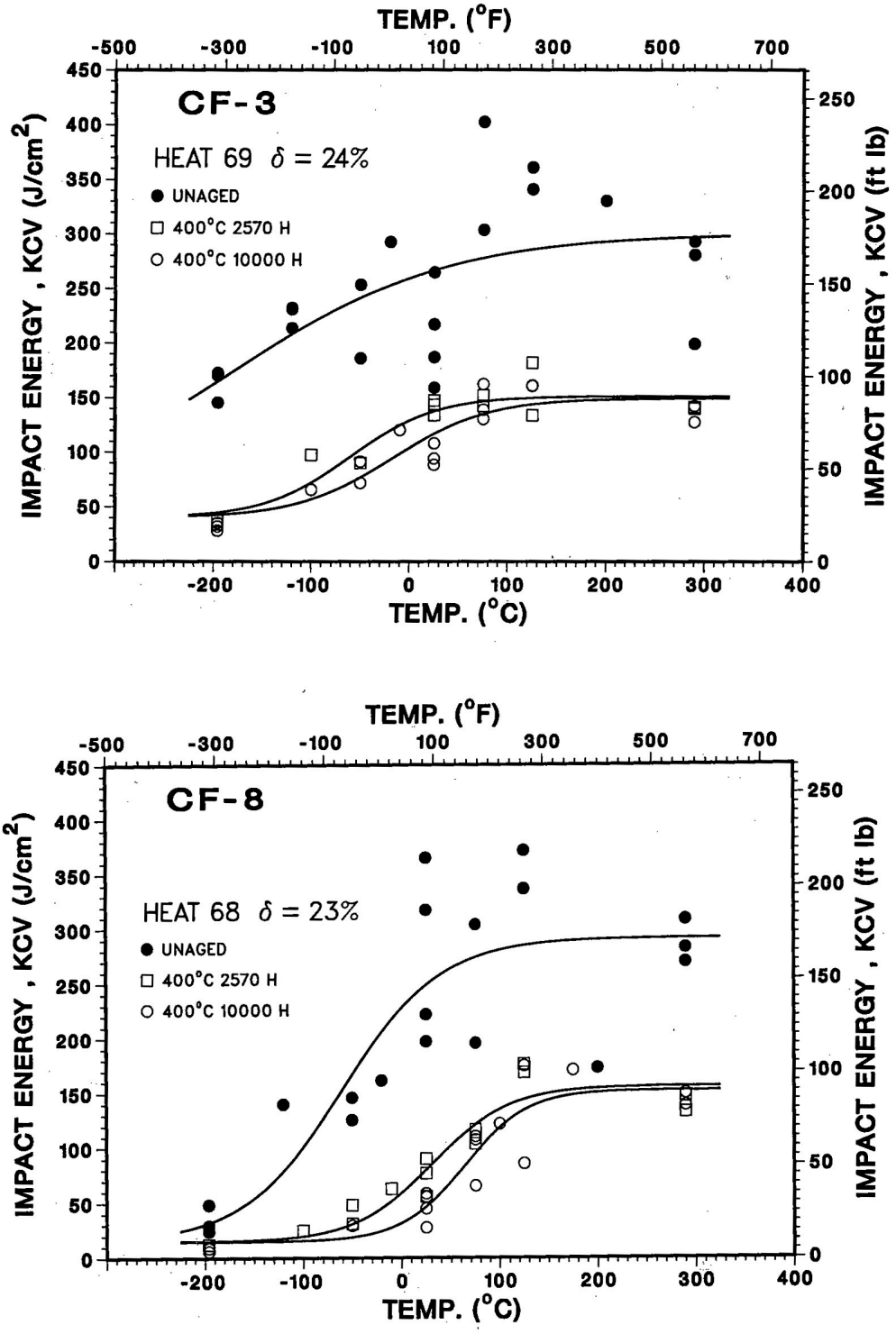

Figure 21. Effect of Aging Time on the Ductile–to–Brittle Transition Curves for CF–8, CF–3, and CF–8M Grades of Cast Stainless Steel Aged at 400°C.

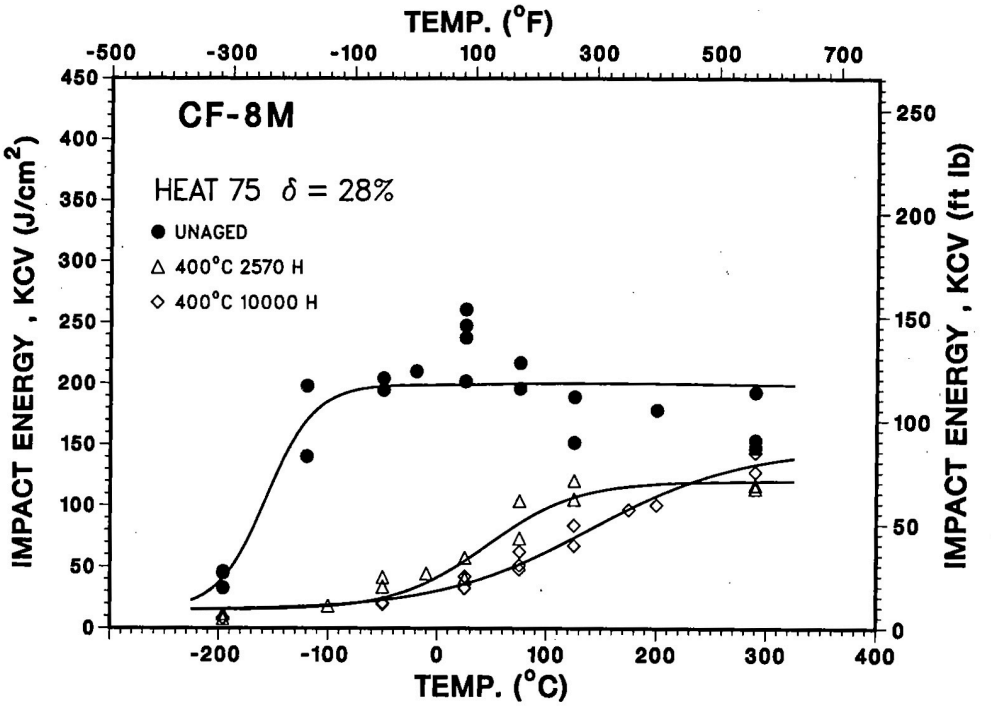

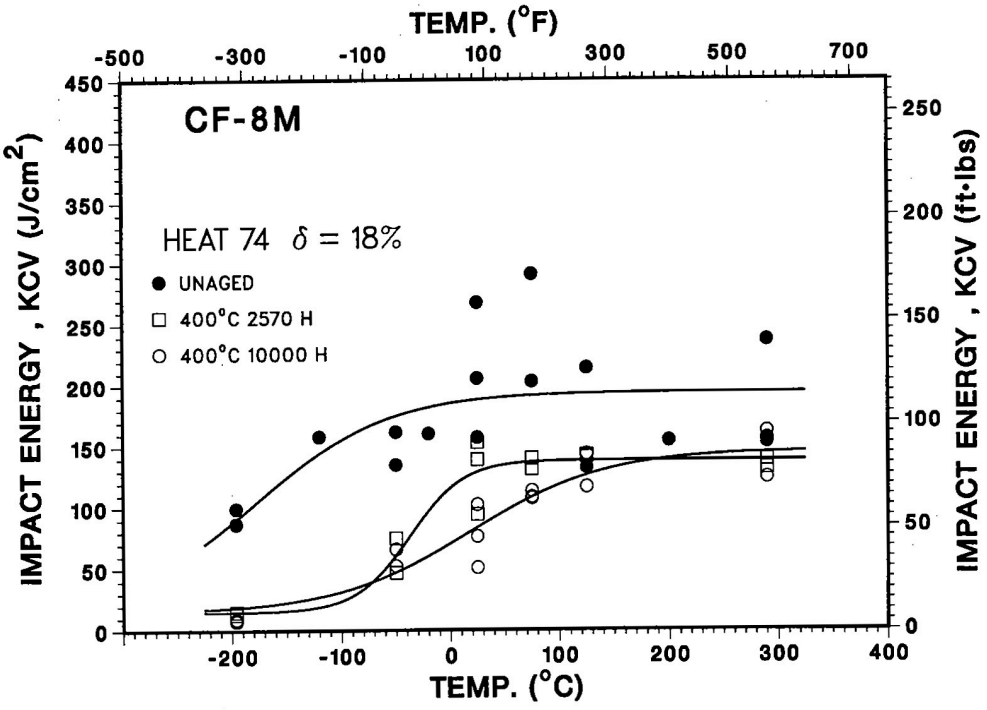

Figure 21. (Contd.)

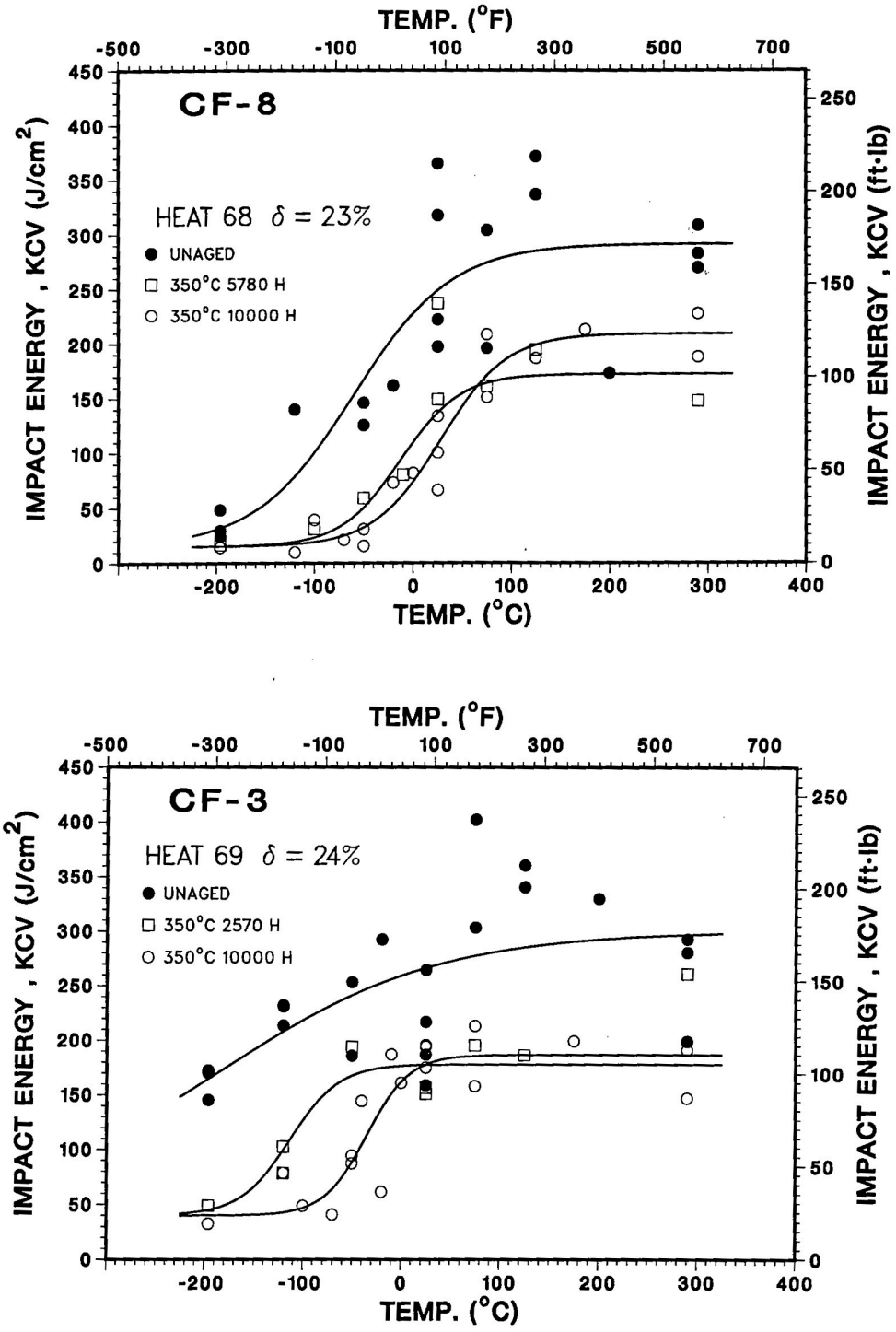

Figure 22. Effect of Aging Time on the Ductile–to–Brittle Transition Curves for CF–8, CF–3, and CF–8M Grades of Cast Stainless Steel Aged at 350°C.

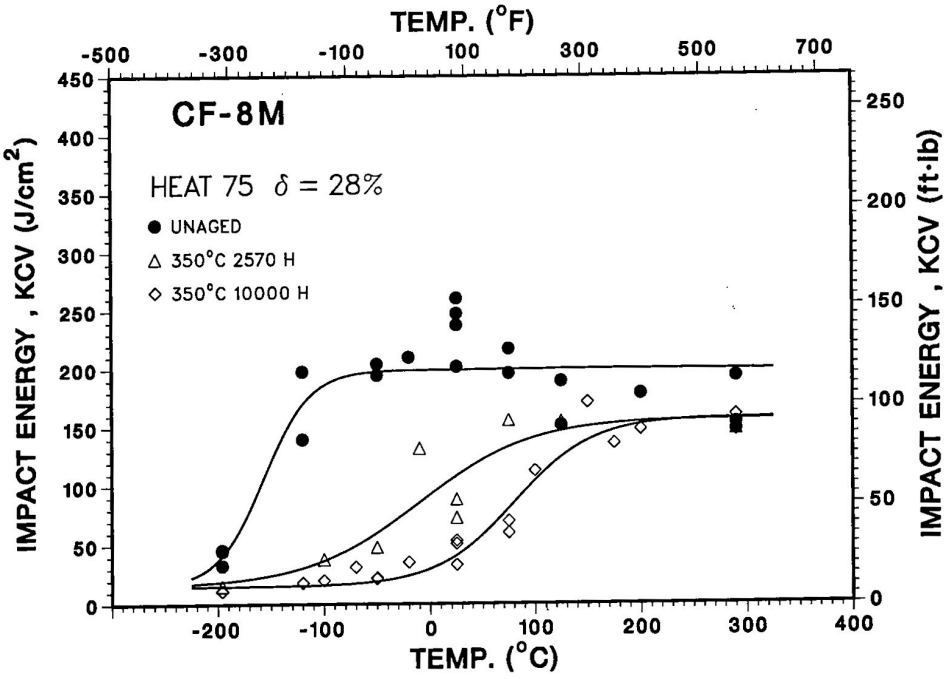

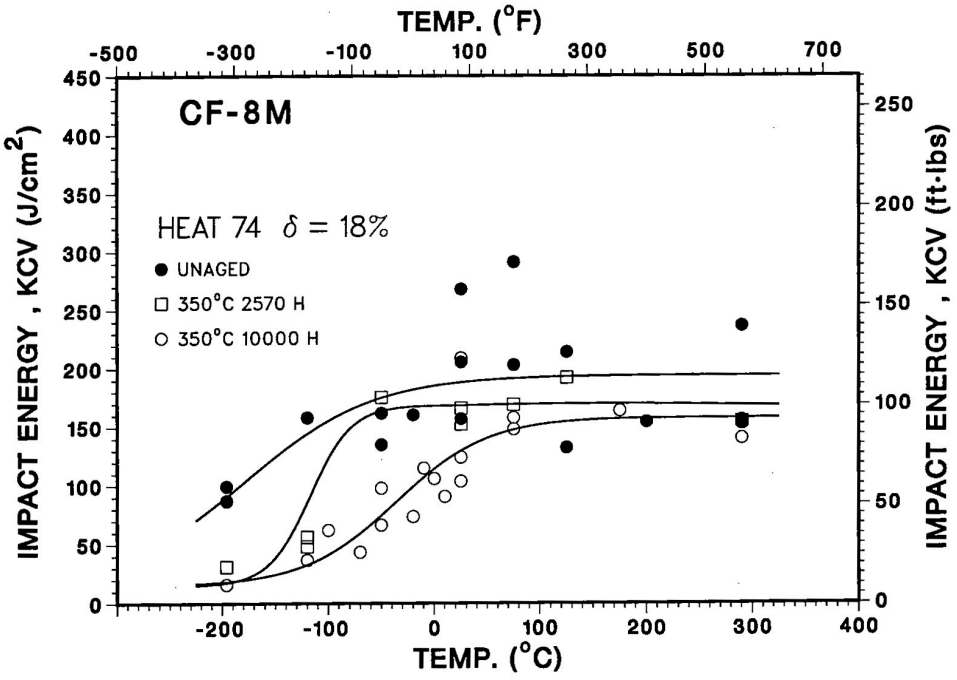

Figure 22. (Contd.)

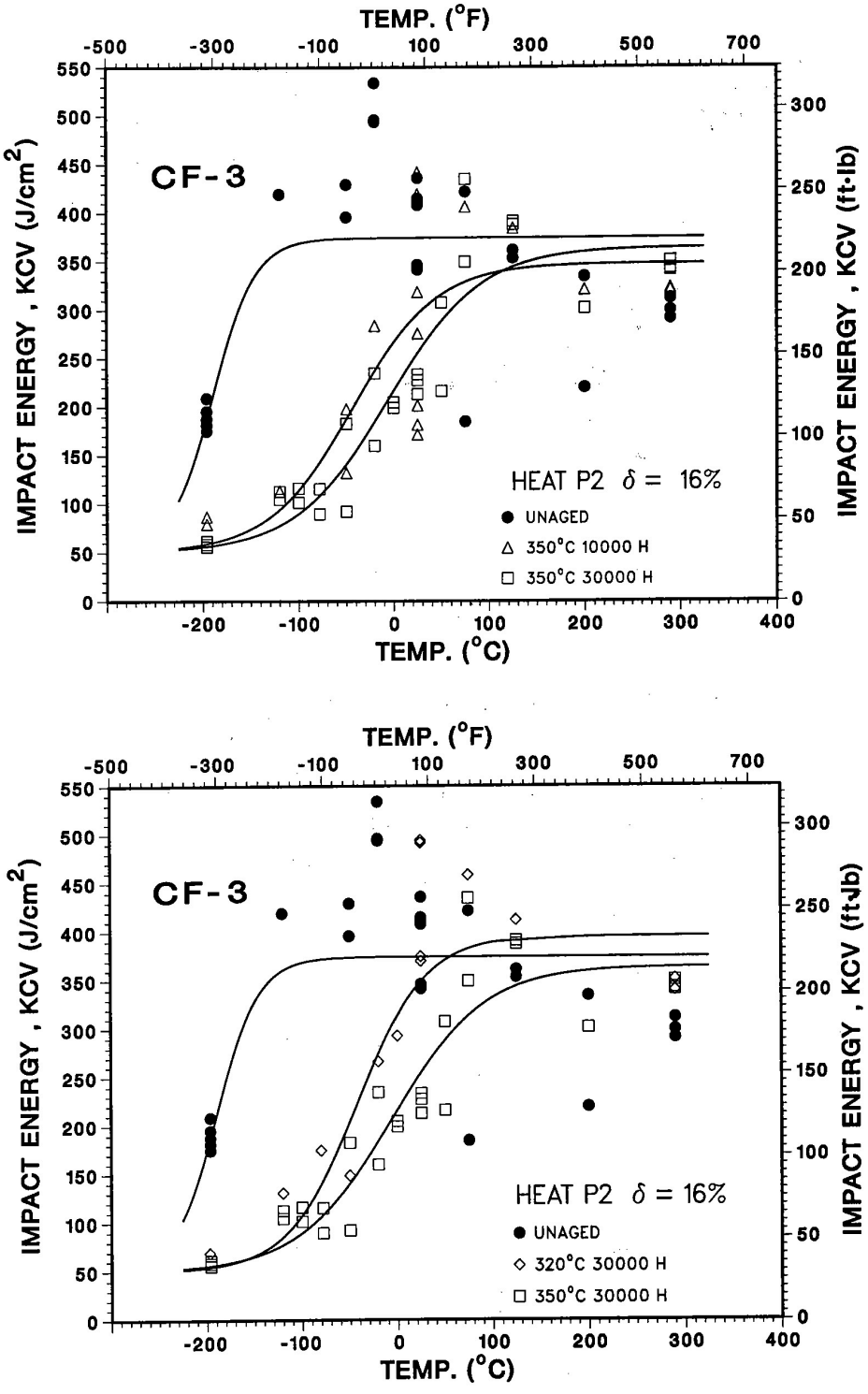

Figure 23. Effect of Aging Time and Temperature on the Ductile–to–Brittle Transition Temperature for the Centrifugally Cast Pipe P2 (CF–3 Grade).

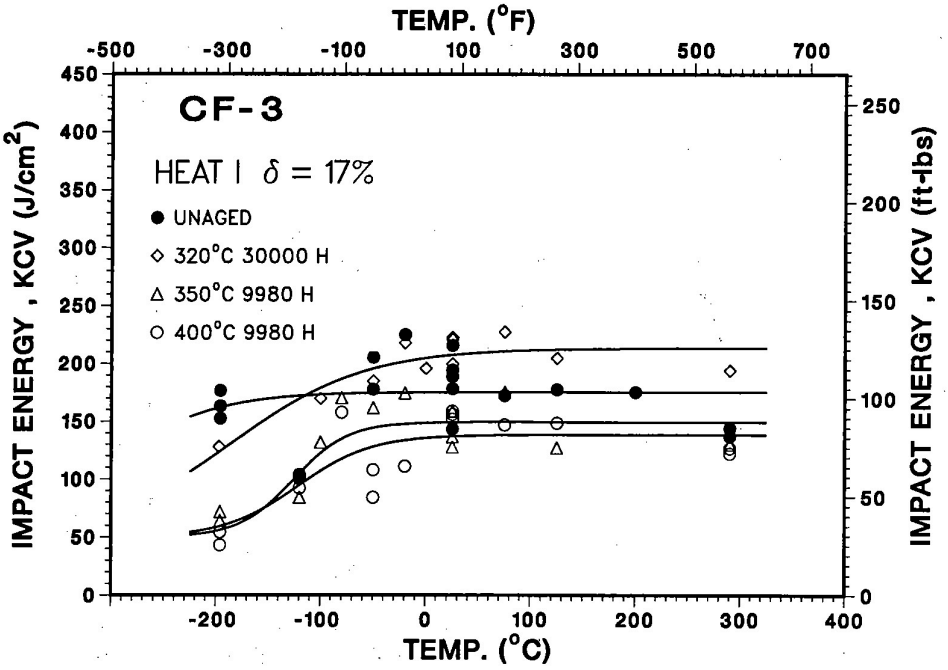

Figure 24. Effect of Aging Time and Temperature on the Ductile–to–Brittle Transition Temperature for the Pump Impeller I (CF–3 Grade)

The results indicate that thermal aging decreases the impact energy and shifts the ductile–to–brittle transition curves to higher temperatures. However, different heats exhibit different degrees of embrittlement. In general, the low–carbon CF–3 grades of cast materials are the most resistant, and the molybdenum–containing CF–8M grades are least resistant to embrittlement. For all grades of cast materials, the extent of embrittlement increases with an increase in ferrite content. The significant results are summarized below.

(1) High–carbon CF–8 stainless steels exhibit low lower–shelf energy and high mid–shelf transition temperature relative to the low–carbon CF–3 steels. The lower impact energy of CF-8 steels is attributed to $M_{23}C_6$ carbides that form at the ferrite/austenite phase boundaries during production heat treatment of the casting.

(2) The mid–shelf transition temperature of unaged CF–8M steels is lower than that of unaged CF–8 steels. The difference is due to the absence of phase boundary carbides in the as–cast CF–8M material.

(3) The results suggest a "saturation effect" for USE after aging. For example, the values of USE decrease significantly after aging for ~2600 h at 400°C and do not change for longer aging times, Figs. 21 and 22. This behavior is observed for materials of all grades.

(4) Thermal aging leads to a decrease in the ferrite content of all grades of cast stainless steel, Fig. 25; particularly after aging at 450°C. The decrease in ferrite content is significantly greater for CF–8M steels than for steels of other grades. The metallographic data on aged material indicate that additional precipitation of phase boundary carbides

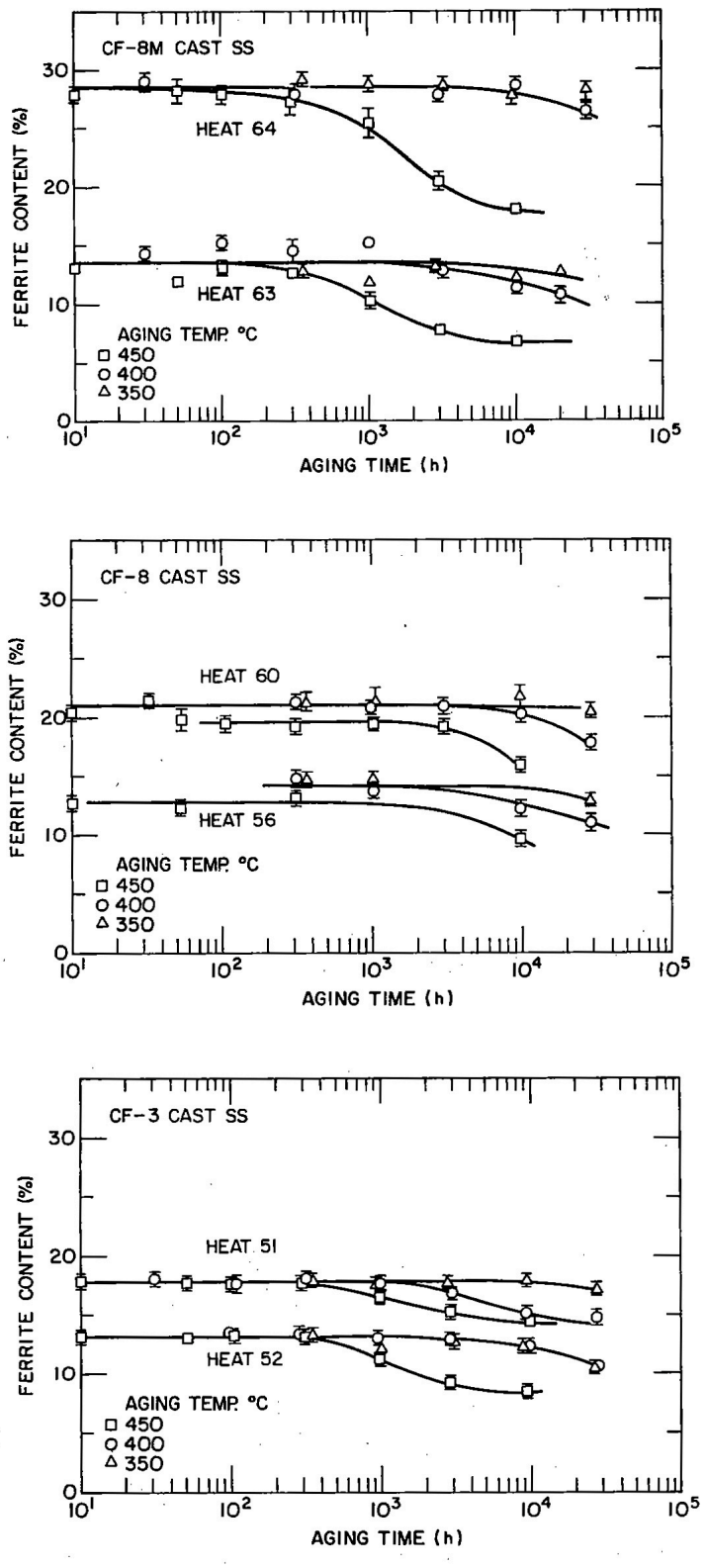

Figure 25. Decrease in Ferrite Content of Thermally Aged CF–8M, CF–8, and CF–3 Cast Stainless Steels.

and/or growth of existing carbides occurs in the CF–8 and CF–8M steels during aging, particularly at 450°C. The precipitation of chromium–rich carbides is always accompanied by a decrease in the ferrite content.[16] The depletion of chromium destabilizes the ferrite phase, leading to ferrite-to-austenite transformation along the phase boundary. The growth of austenite into the ferrite grain occurs as cellular precipitation along with the carbides.[16] This behavior may explain the decrease in ferrite amount in CF–8M steels aged at 450°C.

(5) Charpy–impact data for CF–3 and some CF–8M steels indicate an inversion in impact energy at temperatures in the transition region, i.e., the impact energy of samples aged at 450°C is higher than that of samples aged for similar times at 400°C. For example, the mid–shelf transition temperature (constant C in Table 7) for Heats 69, 70, 74, and 75, aged for 2570 h at 450°C, is lower than that after aging at 400°C for the same length of time. Furthermore, the room temperature impact energies of Heats 52, 47, 51, and P2, aged for 10,000 h at 450°C, were 10 to 15% higher than after aging for 10,000 h at 400°C. This behavior was observed for cast materials that contain no phase boundary carbides and have a very low mid–shelf transition temperature in the unaged condition, i.e., for most of the low–carbon CF–3 and some CF–8M steels. An inversion in impact energy has also been observed in studies at Electricité de France (EdF)* on CF–8 and CF–8M steels aged at 350 and 400°C for times up to 30,000 h. However, all heats that show inversion either contain <18.5 wt.% Cr or the content of ferrite formers (Cr+Mo+Si) is <23.5 wt.%.

(6) The kinetics of embrittlement vary significantly for the various heats of cast stainless steel; the activation energies range between 90 and 235 kJ/mole (20 and 56 kcal/mole). The activation energy is lower for the molybdenum–containing CF–8M steels and for steels with higher nickel content. The activation energy values obtained in the present study are significantly higher than those observed in the GF study,[1] where activation energies were between 70 and 105 kJ/mole (17 and 25 kcal/mole).

(7) The shape of the impact energy–vs–aging time curves also varies considerably for the various heats, e.g., the shape factor α in Table 6 varies between ~0.6 and 1.7.

These results indicate that the kinetics and extent of embrittlement are controlled by several mechanisms that depend on material parameters and aging temperature. The presence of cellular carbides along the phase boundaries and the large reduction in ferrite content further suggest that 450°C aging is not representative of low–temperature aging and, thus, embrittlement data therefrom should not be extrapolated to reactor operating temperatures.

The results also indicate that estimations of the kinetics of embrittlement from Eq. (2) are not accurate for most heats of cast stainless steel. The activation energies determined from Eq. (2) are significantly lower than those observed in the present study. For the heats investigated in this study, the minimum value of impact energy is achieved after 3,000 to 10,000 h at 400°C. Arrhenius extrapolation of this aging time and temperature to reactor operating conditions, for an activation energy of 90 kJ/mole (21.5 kcal/mole), would correspond to 3 to 10 yr of service at 320°C. Extrapolation based on a higher activation energy, e.g., 190 kJ/mole (45.4 kcal/mole), suggests that the laboratory aging conditions represent 33 to 111 yr of reactor service. Consequently, the predictions based on Eq. (2) will be

---

* M. Guttmann, EdF, private communications, October 1987.

conservative for most heats of cast stainless steel. However, because Eq. (2) does not consider the effects of nickel, carbon, or nitrogen, it may be nonconservative for some materials since these elements have a strong effect on the kinetics of embrittlement.

3.2 Fracture Morphology

The fracture surfaces of the Charpy–impact test specimens were examined to characterize the fracture mode. Examples of typical fracture behavior observed for aged specimens tested at room temperature are shown in Figs. 26 and 27. Four fracture modes were observed for these specimens, viz., cleavage of ferrite (C), separation of the ferrite/austenite phase boundary (B), ductile shear failure (D), and dimpled ductile tearing (T). Phase boundary separation and/or cleavage are associated with brittle fracture. The relative amount of each fracture mode depends on the test temperature, the time and temperature of aging, and the concentrations of carbon and nitrogen in the steel. The significant results are as follows:

(1) All fracture modes are observed at test temperatures in the range of the lower–shelf energy, i.e., at temperatures below the transition. For heats with a very low lower–shelf energy, e.g., Heats 68, 74, or 75, the fracture is predominantly by phase boundary separation and cleavage of ferrite (<20% of the fracture surface showed ductile failure). The amount of ductile fracture increases with an increase in temperature. The fracture is completely ductile at temperatures above the transition temperature.

(2) The changes in the fracture mode after thermal aging correspond to the shift in the transition curve. The fracture surfaces of unaged and aged specimens of Heat I, tested at different temperatures, are shown in Figs. 28a and 28b, respectively. In the unaged condition, this heat does not show a transition, and a dimpled ductile failure is observed at all test temperatures. Failure occurs by void formation and growth. This behavior is reflected in the size of the dimples, viz., the size increases with test temperature. Thermal aging of the material leads to cleavage of the ferrite phase when tested in the temperature range of the lower–shelf energy. However, only 40 to 50% of the fracture surface shows cleavage; the remaining material fractures by ductile shear (D) or tearing (T). The amount of cleavage decreases with an increase in temperature, with a complete ductile failure occurring above 25°C.

(3) The amount of cleavage observed on the fracture surfaces is generally much larger than the ferrite content of the material. These results indicate that fracture occurs preferentially along the ferrite. The ferrite phase fractures by cleavage, and then the interconnecting regions fail by either ductile shear and tearing or phase boundary separation, Fig. 29.

(4) Phase boundary separation is observed only in the high-carbon cast stainless steels and is attributed to $M_{23}C_6$ carbides that form during production heat treatment of the casting. For CF–8 cast steels, large carbides precipitate predominantly at the ferrite/austenite phase boundaries, whereas for the molybdenum–containing CF–8M steels, carbides form at the phase boundaries and in the austenite matrix. The presence of large carbides weakens the phase boundaries and the fracture surfaces of Charpy–impact specimens, tested at temperatures below the transition temperature, show a significant amount of phase boundary separation. The fracture surfaces of unaged specimens of

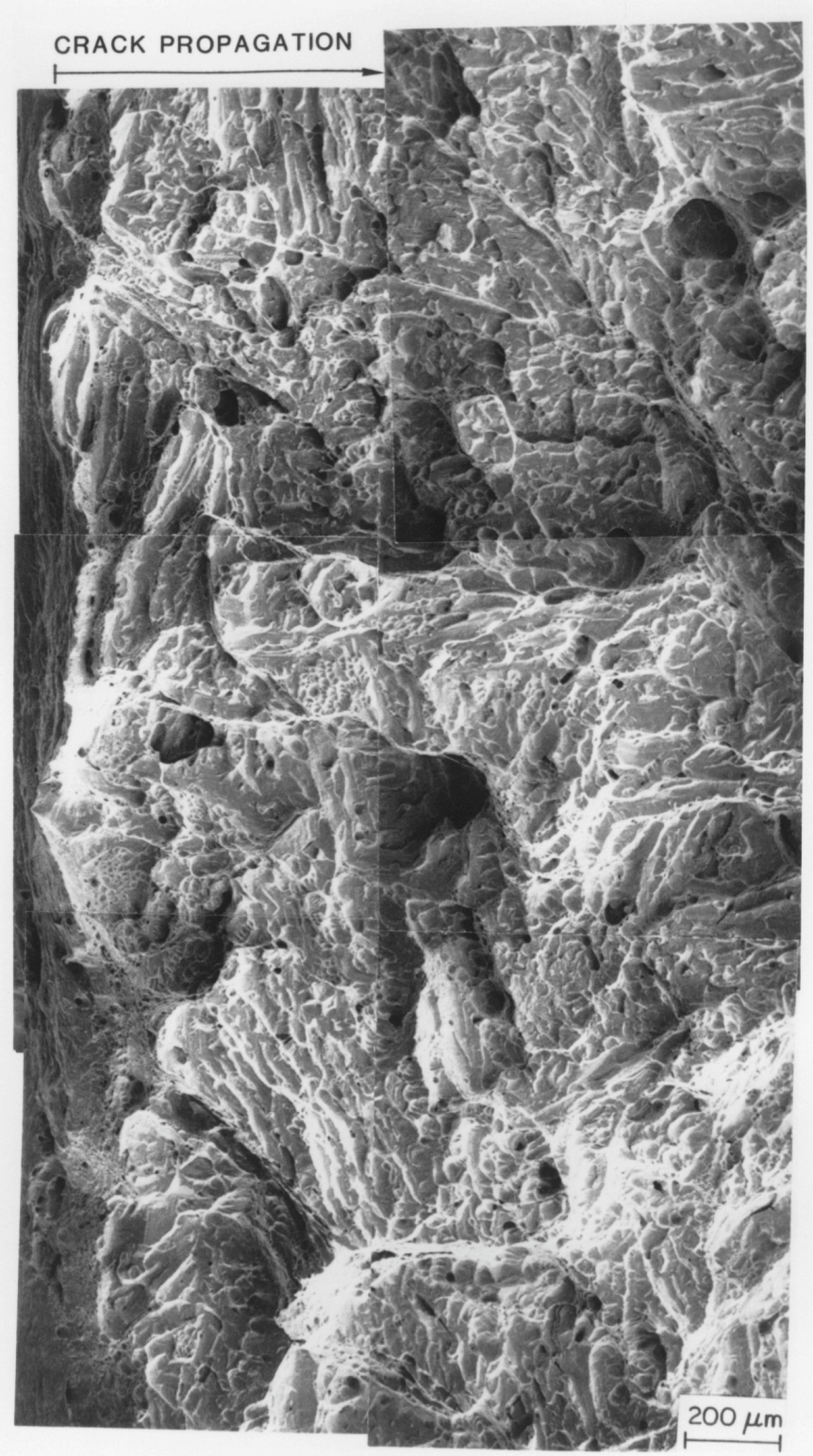

Figure 26. Fracture Surfaces of Aged CF–3 Cast Steel Tested at Room Temperature. (a) Heat 69, 24% ferrite and (b) Heat 51, 18% ferrite. Crack propagation from left to right.

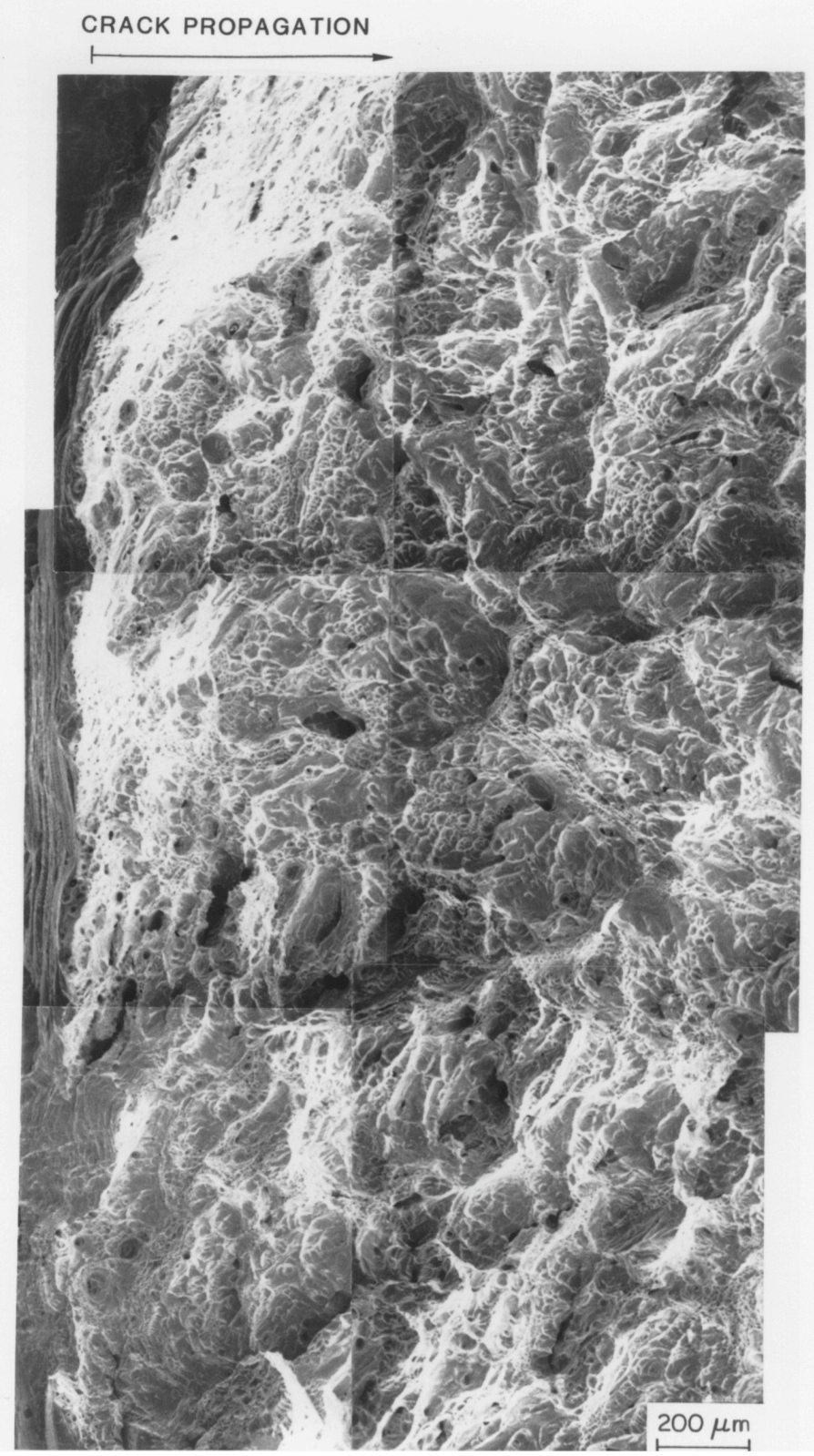

Figure 26. (Contd.)

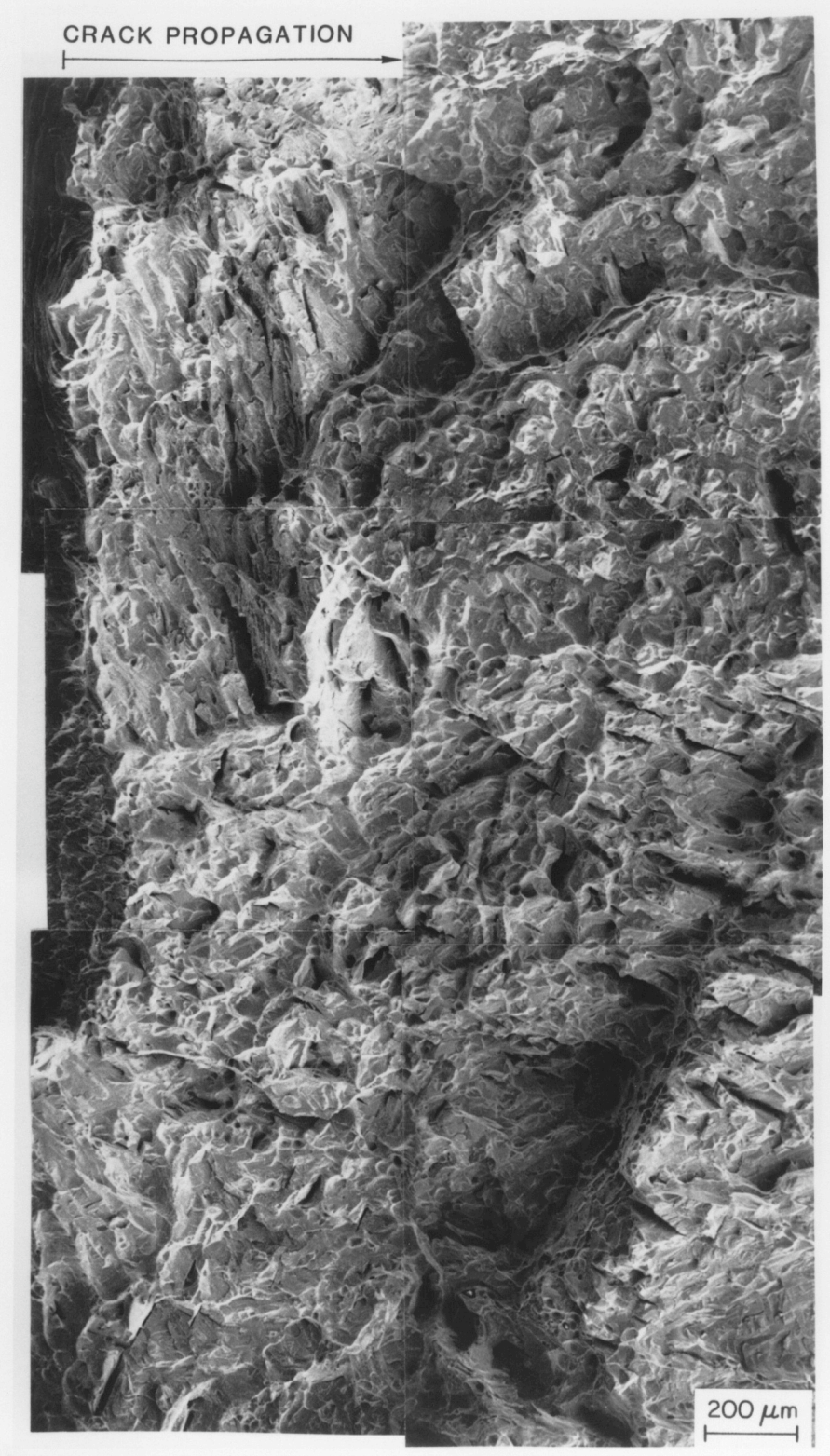

Figure 27. Fracture Surfaces of Aged CF–8 Cast Steel Tested at Room Temperature. (a) Heat 68, 21% ferrite and (b) Heat 60, 21% ferrite. Crack propagation from left to right.

Figure 27. (Contd.)

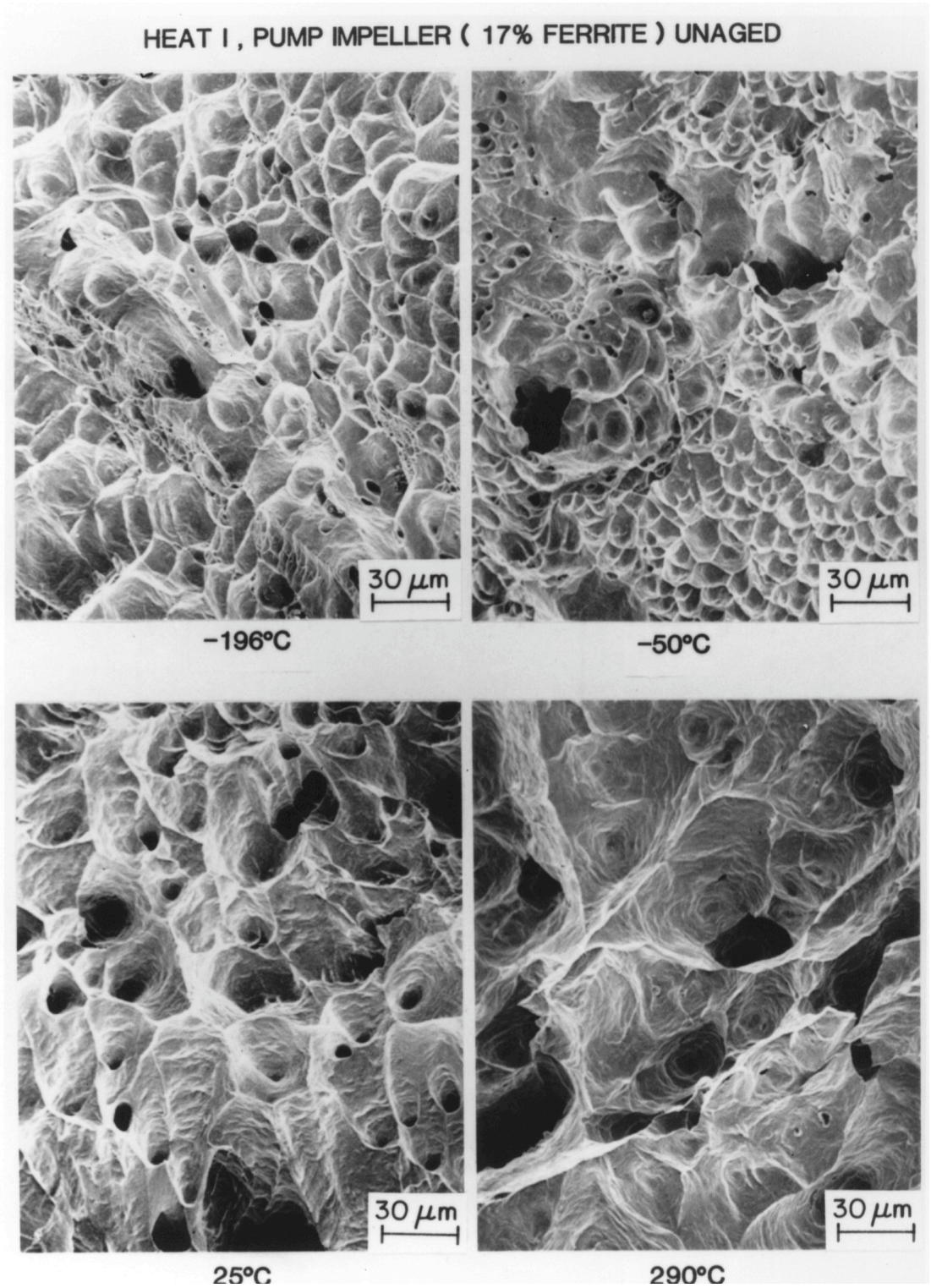

Figure 28. Fracture Surfaces of Impact Test Specimens of (a) Unaged and (b) Aged Heat I Tested at Different Temperatures.

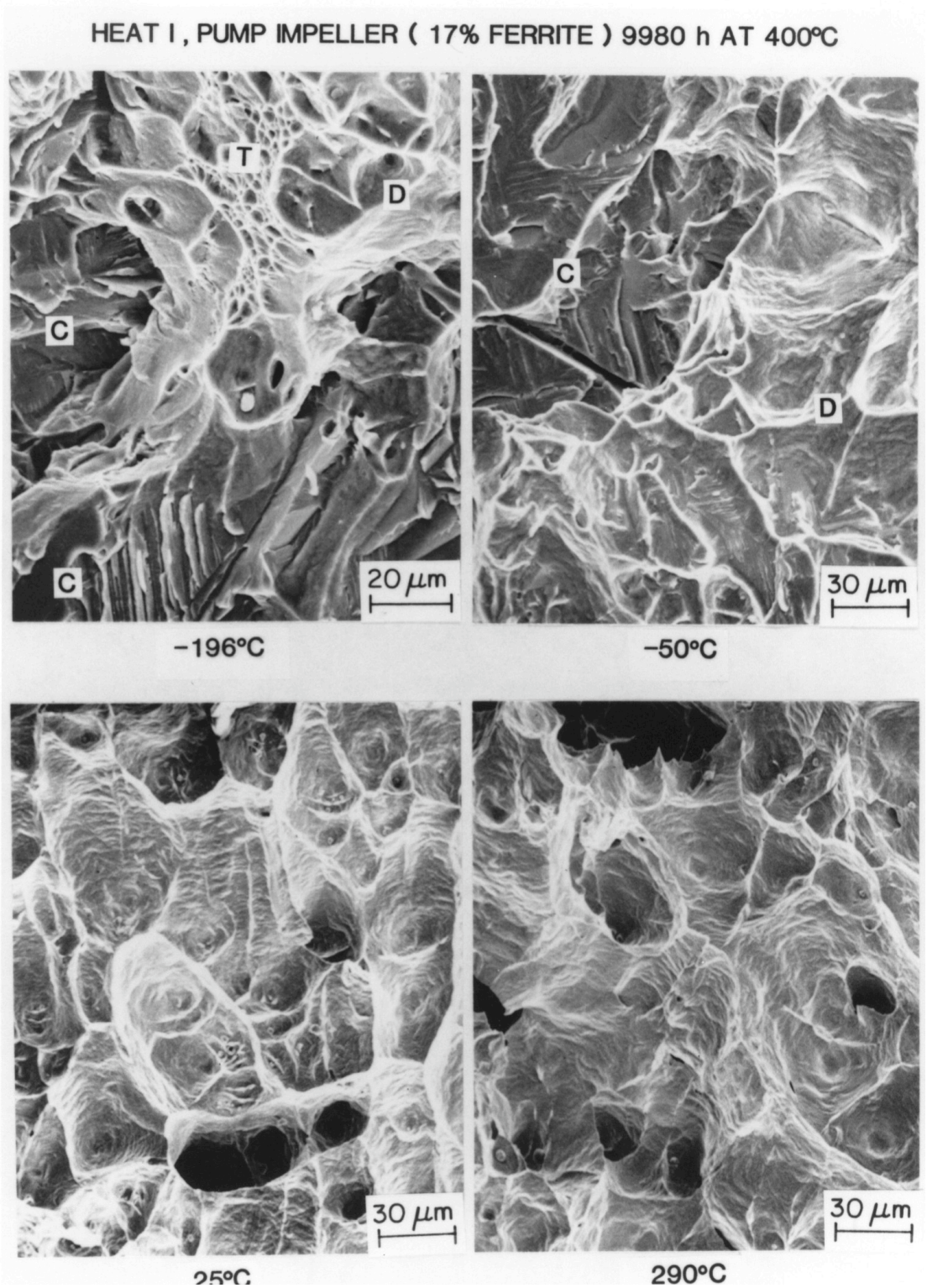

Figure 28. (Contd.)

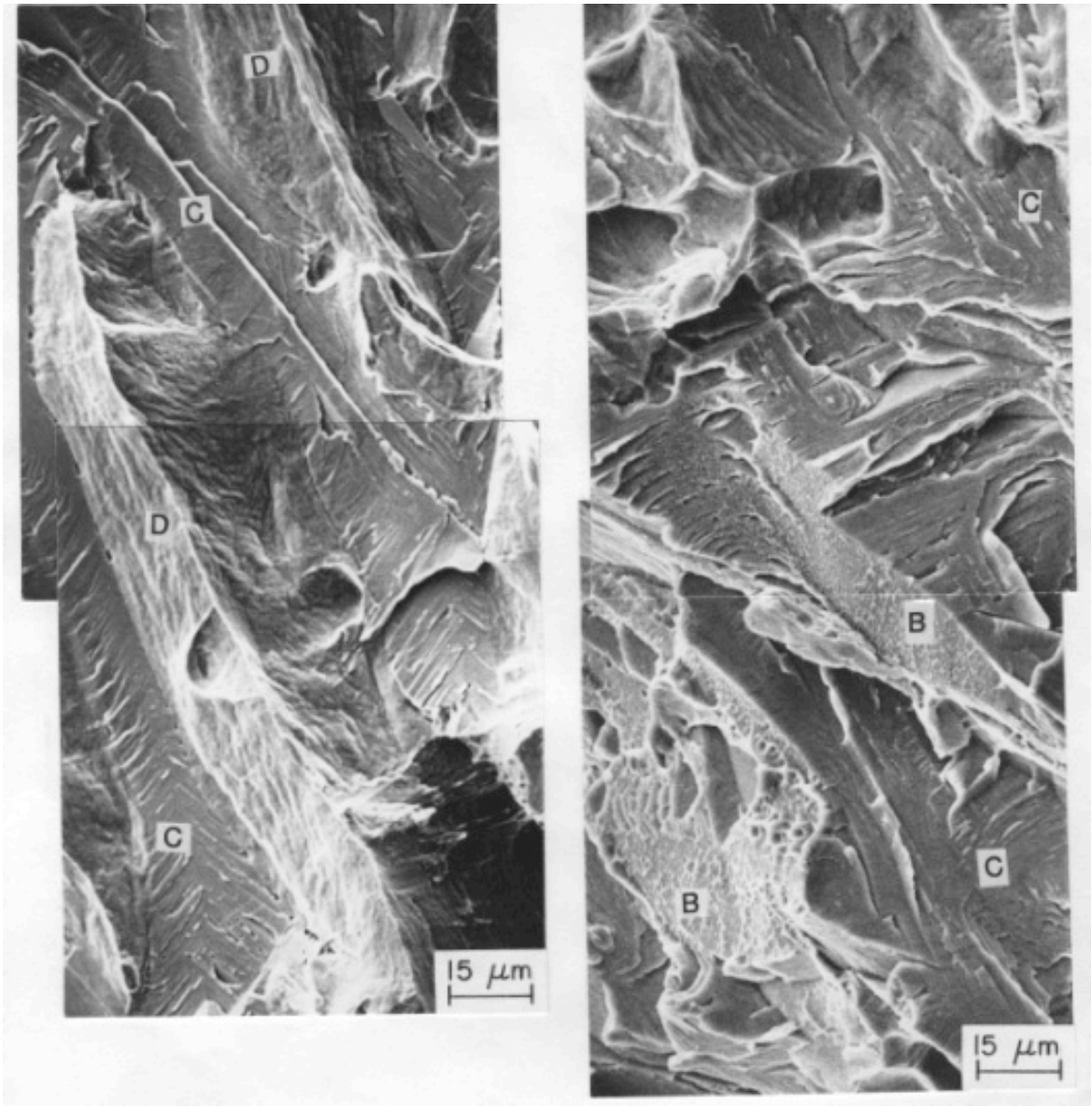

Figure 29. Fracture Surfaces of Impact Test Specimens of Heat 68 Aged for 10,000 h at 400°C and Tested at Room Temperature.

Heats 68 and 60, tested at –196°C, are shown in Fig. 30. The fracture mode for both heats is predominantly phase boundary separation and cleavage of ferrite. The presence of phase boundary separation was confirmed by energy dispersive X-ray analyses of the mating regions on the two fracture surfaces. The ratios of X-ray peaks of chromium to iron, or nickel to iron were indicative of ferrite on one surface and austenite on the other surface. Similar fracture behavior was also observed for some unaged heats of CF–8M steel, depending on whether or not the material contained phase boundary carbides. The high transition temperature and the low lower–shelf energy for CF–8 steels may be attributed to phase boundary carbides and boundary separation.

(5) The differences in the fracture mode of CF–8 and CF–3 steels are reflected in the load–time curves of the Charpy tests, Fig. 31. The unaged CF–8 steels exhibit a sudden drop in load before general yielding, whereas the unaged CF–3 steels show significant strain

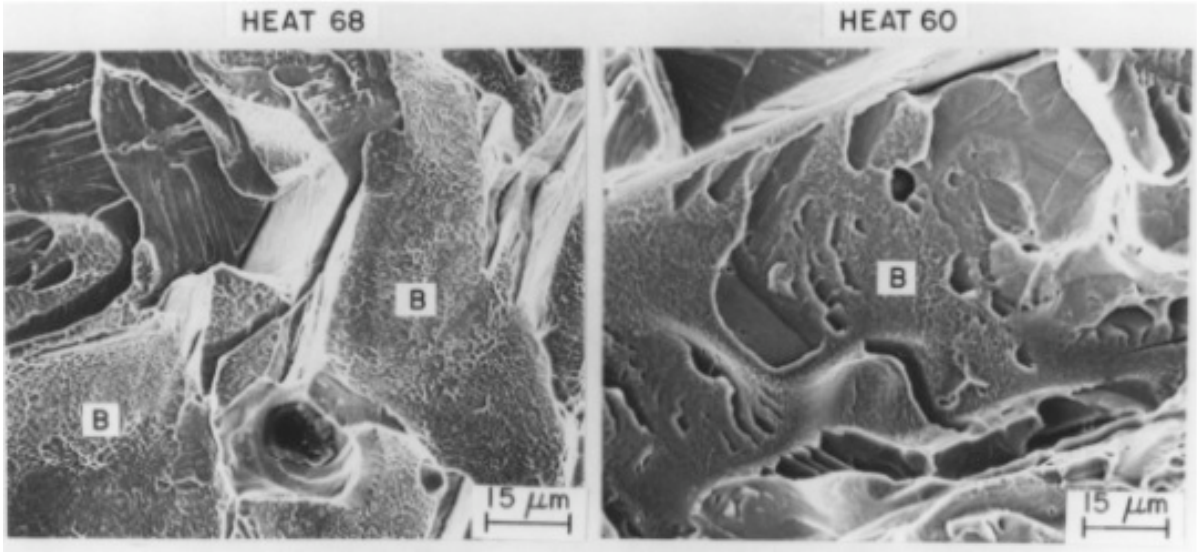

Figure 30. Fracture Surfaces of Impact Test Specimens of Unaged CF–8 Cast Steel Tested at –196°C.

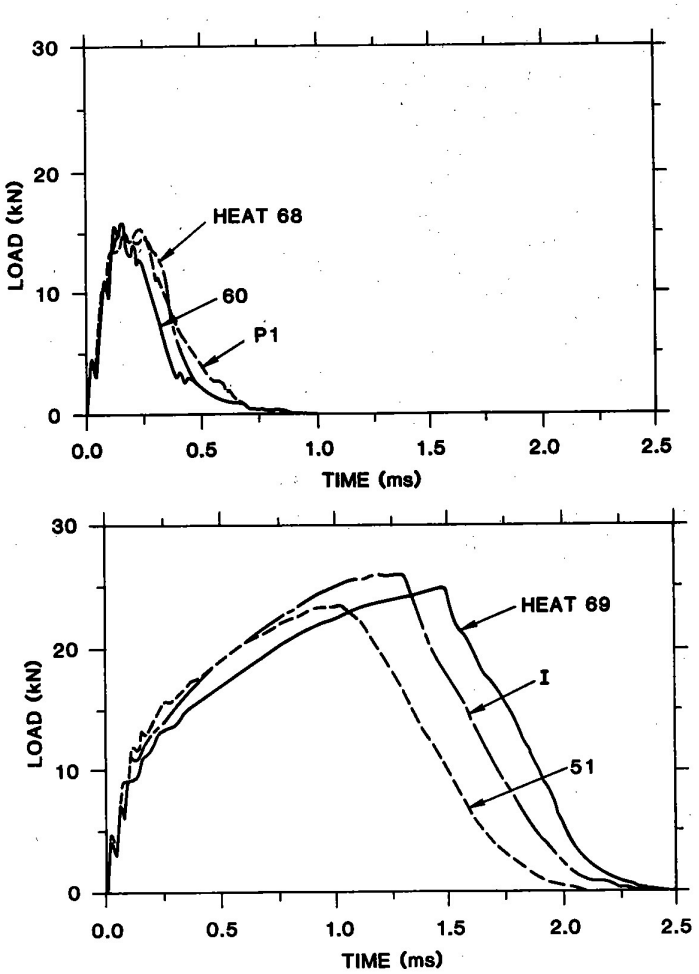

Figure 31. Load–Time Curves for Charpy V–Notch Impact Specimens of CF–8 and CF-3 Steels Tested at –196°C.

hardening and gradual load decrease at fracture. The sharp drop in load indicates brittle fracture. At low temperatures, e.g., –196°C, the ferrite phase in the duplex cast structure is brittle and fails by cleavage. The weak phase boundaries in the CF–8 steels provide an easy fracture path and, consequently, brittle fracture occurs. Furthermore, cracking of the large phase boundary carbides can initiate cleavage cracks in the ferrite matrix, resulting in very low impact strength. For CF–3 steels, although the ferrite fails by cleavage at low temperatures, the surrounding austenite provides ductility. Also, the initiation of cleavage occurs by mechanisms other than carbide cracking, which require higher loads and result in relatively high impact strength.

(6 The fracture surfaces of unaged and aged specimens of Heat 60 (CF–8 grade), tested at –196°C, are shown in Fig. 32. The fracture mode for the specimen aged at 450°C is predominantly phase boundary separation.

(7) The morphology of cleavage varies with the grade of cast stainless steel and the test and aging temperatures. In general, a herringbone cleavage fracture of ferrite was observed for all heats and grades of cast material in the unaged condition or aged at temperatures ≥350°C. It was not observed in the KRB material aged at the reactor operating temperature of 284°C. Examples of typical herringbone cleavage are shown in Fig. 33. The river pattern cleavage was observed only for heats with high ferrite content, e.g., >20%, and large ferrite spacing. A third type of cleavage, with a stepped or terraced appearance, occurred in CF–3 steels. Terraced cleavage fractures in Heat 51, tested at –196°C, and Heat 69, tested at -50°C, are shown in Figs. 34 and 35, respectively. The different cleavage morphology indicates differences in the mechanism for initiation of cleavage in low–carbon CF–3 and high–carbon CF–8 or CF–8M steels as well as in steels aged at different temperatures. Cleavage of ferrite can be initiated by different mechanisms, viz., cracking of second–phase particles (e.g., carbides or nitrides), dislocation pileup, or cracking of twin boundary intersections. Metallographic results indicate that cleavage in CF–8 or CF–8M steel occurs by either of the three mechanisms, viz., cracking of phase boundary carbides, dislocation pileup, or cracking at twin intersections. In the absence of phase boundary carbides, cleavage in CF–3 steels most likely occurs by dislocation pileup or at twin intersections. The latter occurs at higher stress levels and may explain the terraced cleavage morphology. Twinning is a dominant deformation mode in single–phase Fe–Cr–Ni alloys containing >4% nickel.[18–21] Deformation by twinning can occur at temperatures up to 500°C in nickel ferrite alloys that are strengthened by α' particles.[20]

3.3 Tensile Properties

Tensile tests were conducted at room temperature and at 290°C (554°F) on three commercial and five experimental heats that were aged up to 30,000 h at 320, 350, 400, and 450°C. The results and the data obtained by MEA[25] are given in Appendix C. At both test temperatures, thermal aging of the material led to an increase in yield stress and ultimate stress and a slight decrease in ductility. The increase in tensile strength varied significantly for the different heats. Specimens aged for short times at high temperatures, e.g., ~3,000 h at 400 or 450°C, often showed a decrease in yield and ultimate stresses. This behavior can be attributed to the relative contributions of precipitation of second–phase particles in the ferrite and of reduction in ferrite content of the material. The decrease in ferrite content is significant for materials aged at high temperatures, Fig. 25, and, thus, would have a greater effect on the change in tensile stress after thermal aging.

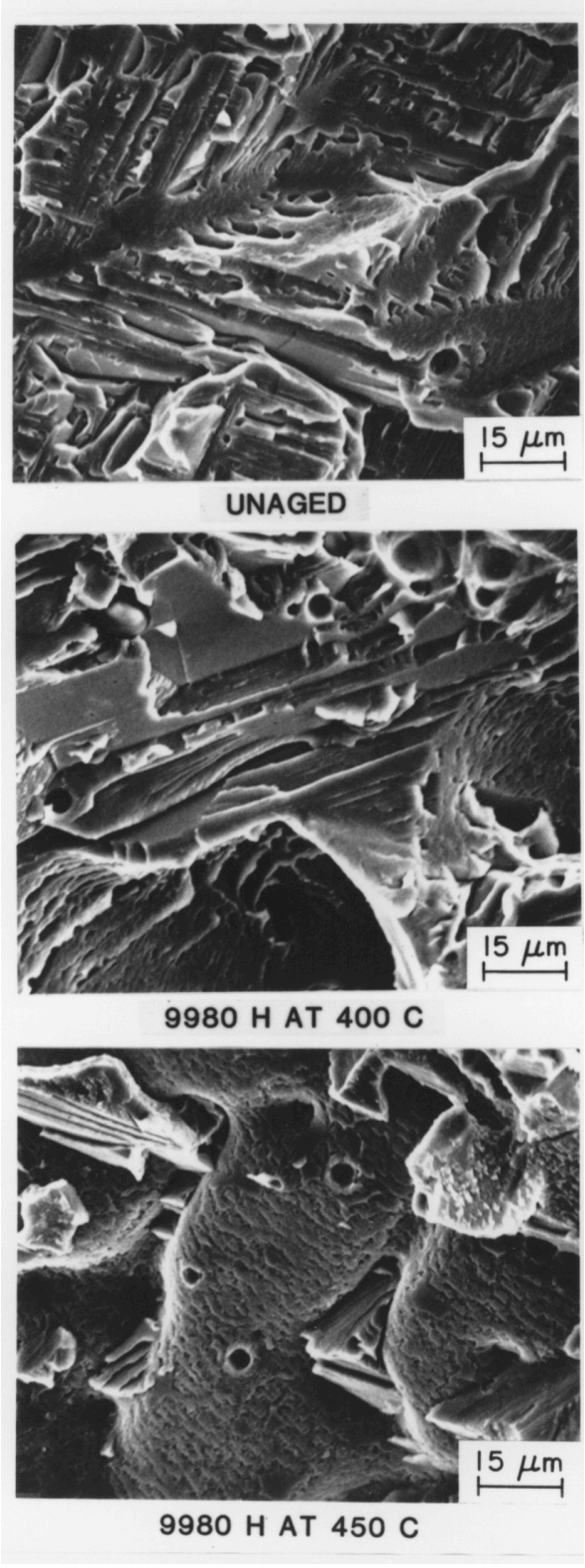

Figure 32. Fracture Surfaces of Impact Test Specimens of Unaged and Aged CF–8 Cast Steel (Heat 60, 21% Ferrite) Tested at –196°C.

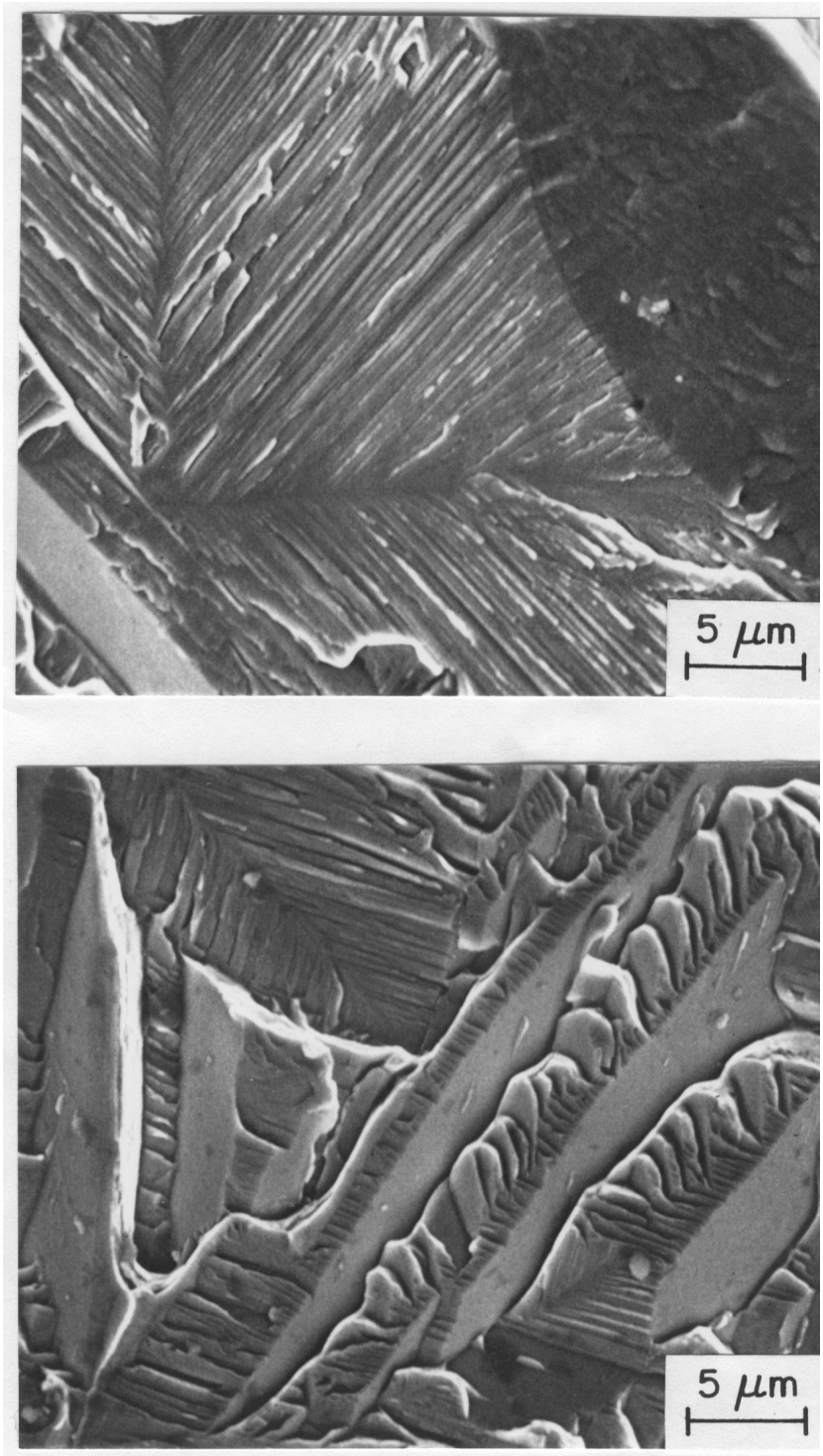

Figure 33. Herringbone Cleavage in Heat P4 Aged for 10,000 h at 400°C and Tested at Room Temperature.

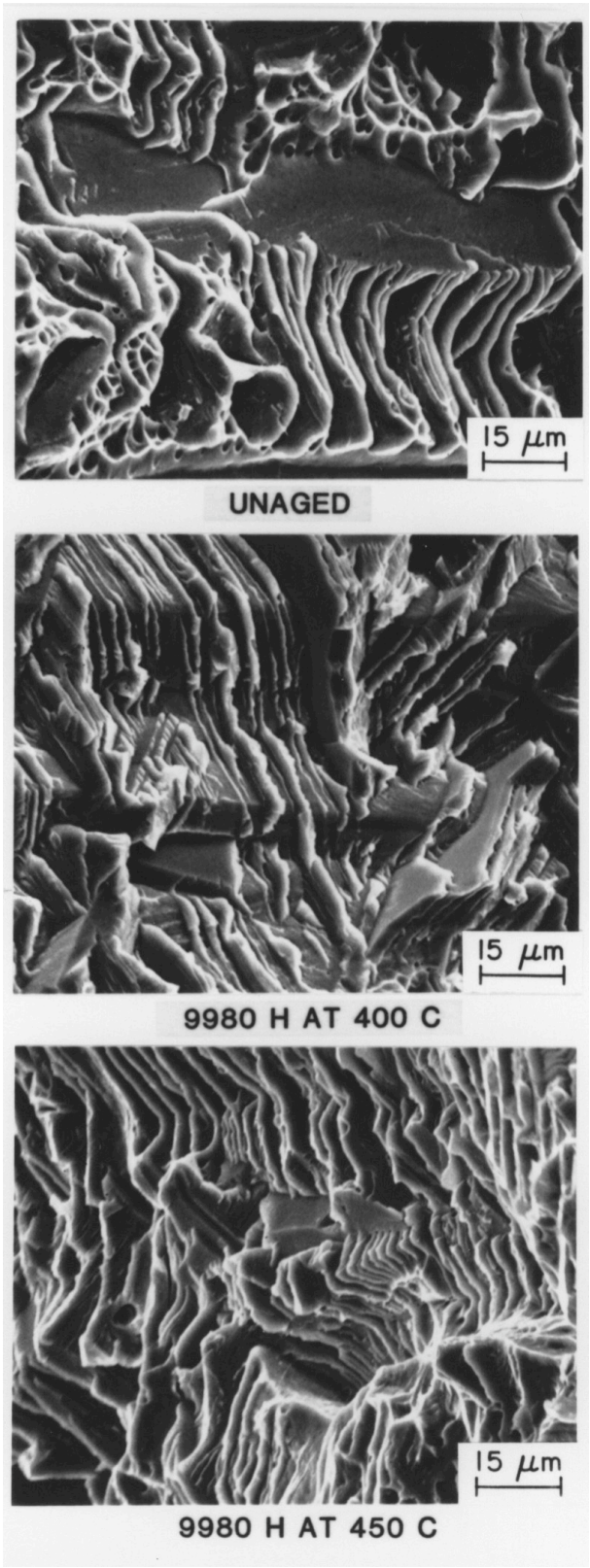

Figure 34. Fracture Surfaces of Impact Test Specimens of Unaged and Aged CF–3 Cast Steel (Heat 51, 18% Ferrite) Tested at –196°C.

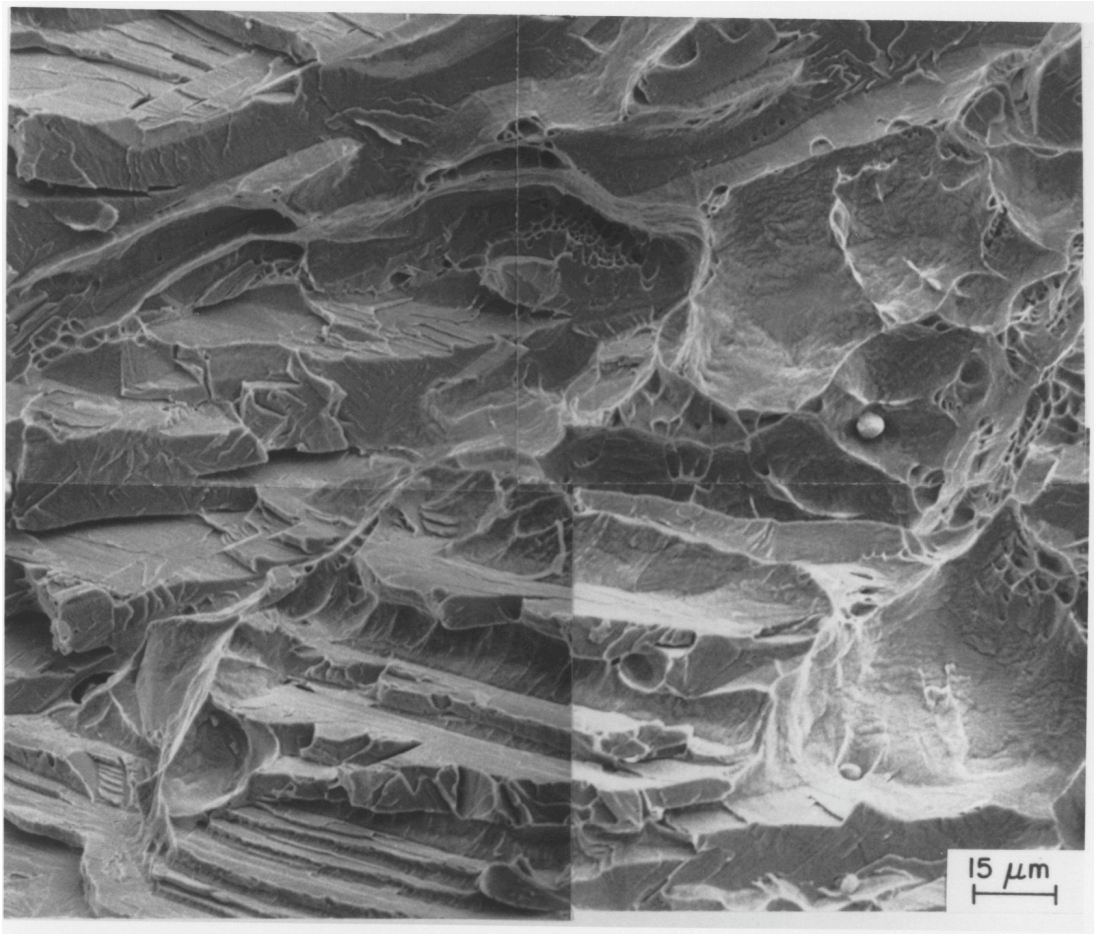

Figure 35. Fracture Surface of Impact Test Specimen of Heat 69 (24% Ferrite) Aged for 10,000 h at 400°C and Tested at Room Temperature.

In Fig. 36, the changes in the yield and ultimate stress of several heats of aged cast stainless steel are plotted as a function of the aging parameter P. The results from tensile tests conducted at Framatome (FRA)[11] on four heats of CF–8 and CF–8M steel are also shown in the figure. The data show considerable scatter. However, for the various aged materials, an increase in yield and ultimate stress is observed for values of P ≥2, which corresponds to aging times of ≥100 h at 400°C. These results are consistent with the Charpy data, i.e., for all heats, the decrease in Charpy-impact energy also occurs when P ≥2. The increase in ultimate stress is substantially greater than the increase in yield stress. The changes in yield and ultimate stress range from –5 to 20% and from –5 to 25%, respectively.

Tensile properties of the cast materials can also be obtained from the Charpy–impact data. For a Charpy specimen, the yield stress is estimated from the expression

$$\sigma_y = CP_y\, B/Wb^2 , \qquad (5)$$

taken from Ref. 27, where Py is the yield load, W is the specimen width, B is the specimen thickness, b is the uncracked ligament, and C is a constant. The yield load was obtained from the load–time traces of the Charpy tests. Deviation from linearity in the load–time

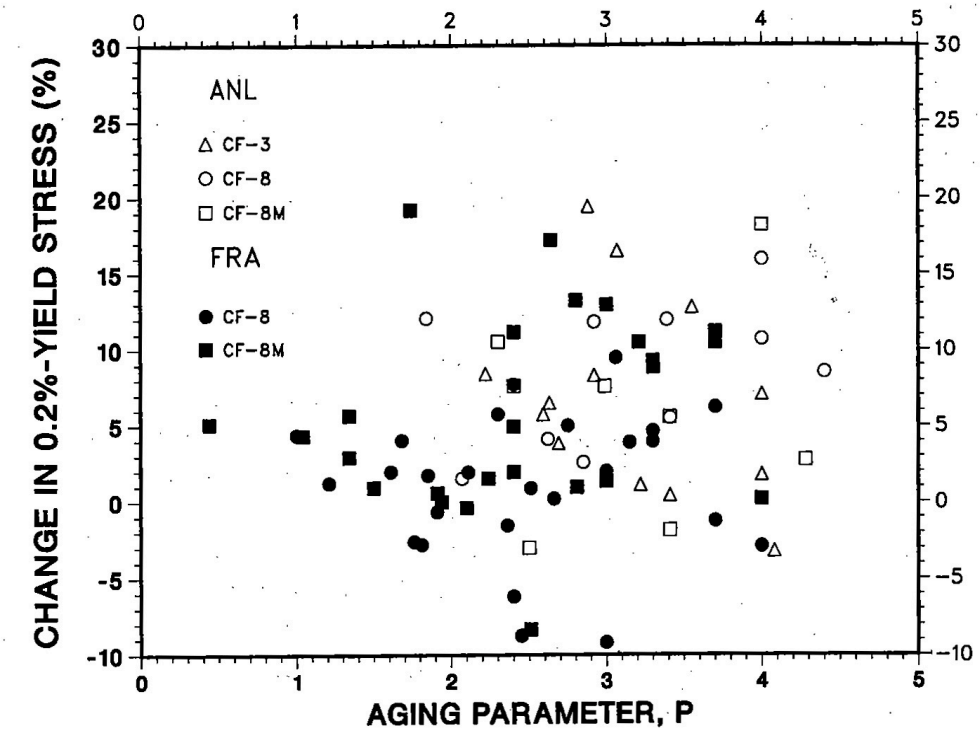

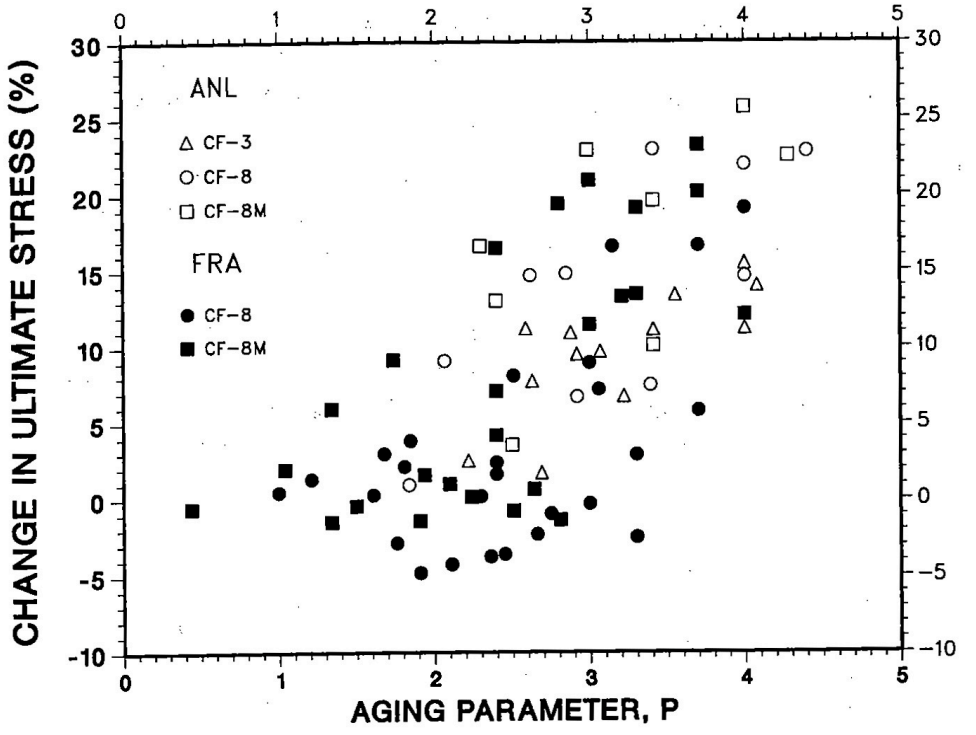

Figure 36. Change in Yield and Ultimate Stress of Aged Cast Stainless Steel as a Function of the Aging Parameter.

trace occurred at 125 to 150 μs for the various heats. The load at 200 μs was estimated to represent 0.2% yield stress. The ultimate stress was also obtained from the impact data by means of Eq. (5) and the maximum load. The yield and maximum loads for all Charpy tests are listed in Appendix B. The constant C was determined by comparing the tensile and Charpy-impact data. The best value of the constant for yield stress was 1.50 for steels of all grades. The constant for ultimate stress was 2.28 for CF-3 and CF-8 steels and 2.54 for CF-8M steel. The estimated values of tensile stress are based on the assumption that strain rate effects are approximately the same for all heats and aging conditions. The estimated values of tensile stress may not be accurate at temperatures corresponding to lower–shelf and transition region.

The yield and maximum loads for unaged Heats 68 (CF–8) and 69 (CF–3) are plotted as a function of test temperature in Fig. 37. The tensile yield and ultimate stresses, estimated from Eq. (5), are shown along separate axes at the right of the figure. Both heats contain approximately the same amount of ferrite. The results show the expected decrease in yield and maximum loads with an increase in test temperature. The yield loads for the low–carbon Heat 69 are lower than those for the high–carbon Heat 68. The maximum loads, however, reflect the differences in the fracture mode for the two heats. For Heat 69, although the ferrite fails by cleavage at low temperatures, the surrounding austenite provides toughness and the material shows significant strain hardening and high maximum loads before fracture. Heat 68 exhibits very little strain hardening at low temperatures because of a weak fracture path via phase boundary separation.

The difference in fracture mode is more obvious in the aged specimens. The yield and maximum loads for Heats 68 and 69, aged for 10,000 h at 400°C, are shown in Fig. 38. For both heats, thermal aging increases the yield and maximum loads at all test temperatures. For Heat 68, critical stress for phase boundary separation is achieved before general yielding at temperatures up to room temperature; the maximum and yield loads are the same. Heat 69 shows strain hardening at all temperatures and fractures at higher loads. Failure occurs at ~16 kN load in Heat 68 and ~20 kN load in Heat 69. The difference in the maximum load at failure suggests a difference in fracture mechanism. The fracture behavior of unaged CF-8M steel, e.g., Heat 75, is similar to that of CF-3 steel, because of the absence of phase boundary carbides in the as–cast structure, Fig. 39. However, thermal aging leads to the formation of phase boundary carbides and a fracture mode for aged CF-8M steels that is identical to that of CF-8 steels, i.e., failure occurs at ~16 kN load. The load vs temperature data shown in Figs. 37–39 are very useful in evaluating the effects of aging on fracture behavior of cast stainless steels, and to evaluate the applicability of high–temperature data to reactor operating conditions.

3.4 J–R Curves

The data for J–R tests conducted at MEA[25] and ANL on eight heats of cast stainless steel are given in Appendix D. The results indicate that thermal aging decreases J_{IC} and the tearing modulus of the material at room temperature as well as at 290°C. The reduction in toughness is greater for materials aged at 400 or 450°C than for those aged at 350°C for similar lengths of time. The fracture toughness of CF–8 steels is lower than for the CF–3 steels. After aging for 10,000 h at 400°C, the J_{IC} value for Heat P1 (CF–8 steel) at room temperature decreased from ~520 to 210 kJ/m^2 (~2,970 to 1,200 in.–lb/in.^{2}), and the tearing modulus decreased from ~680 to 210.

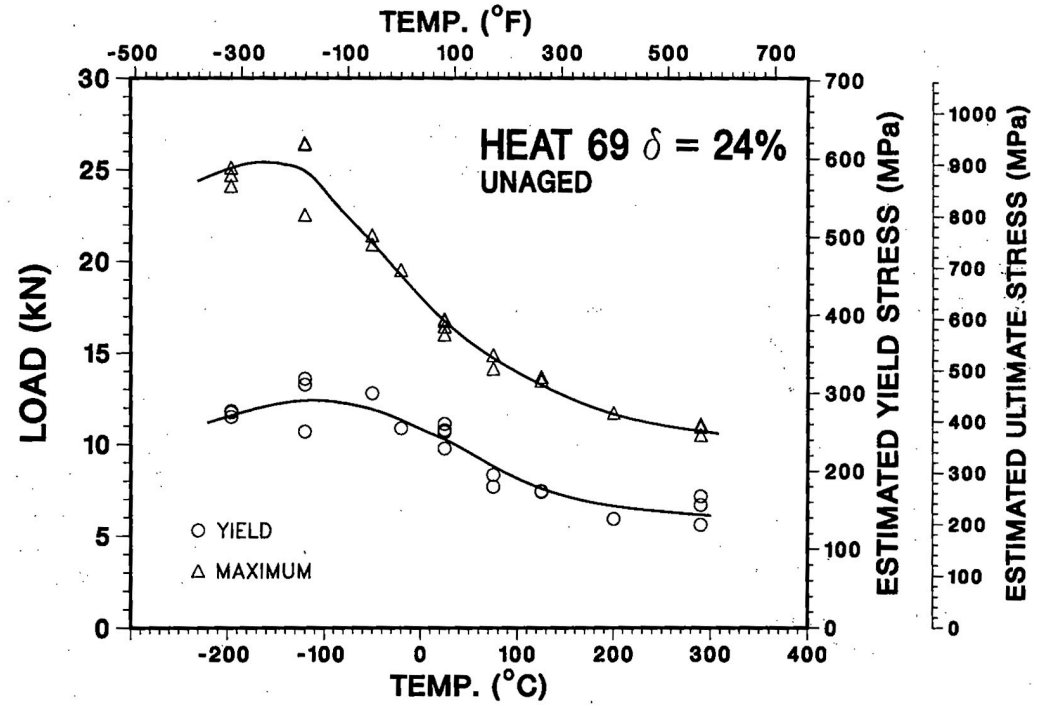

(a)

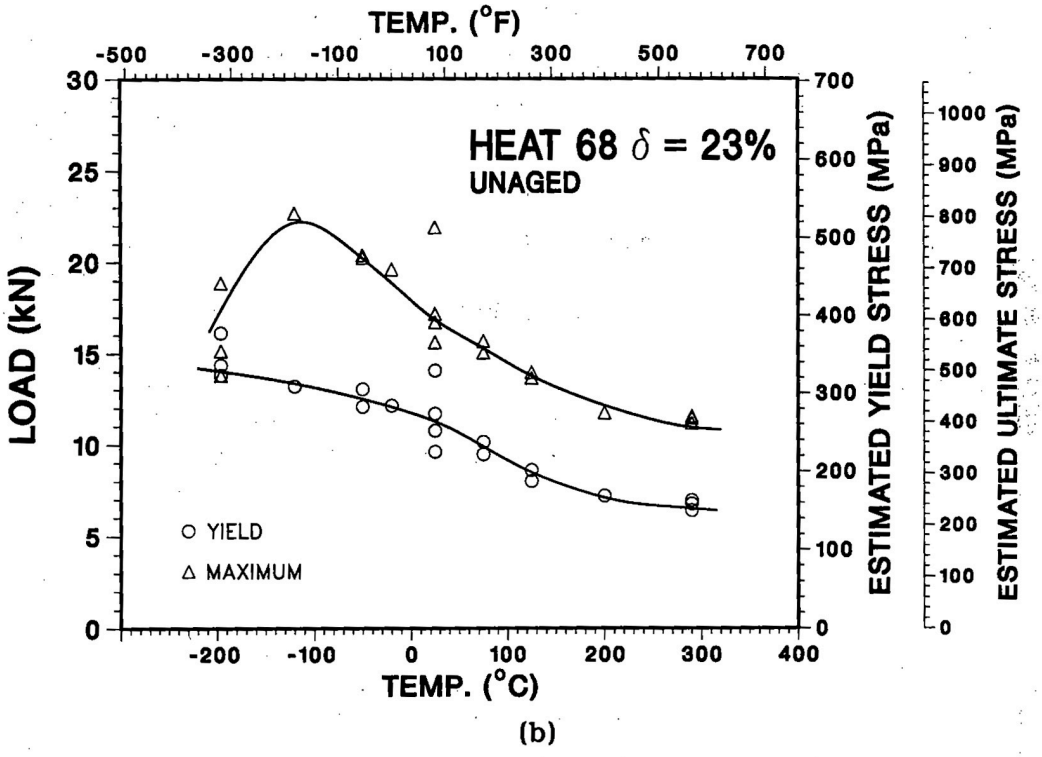

(b)

Figure 37. Yield and Maximum Loads from Charpy Impact Tests for Unaged (a) CF–3 and (b) CF–8 Cast Stainless Steel.

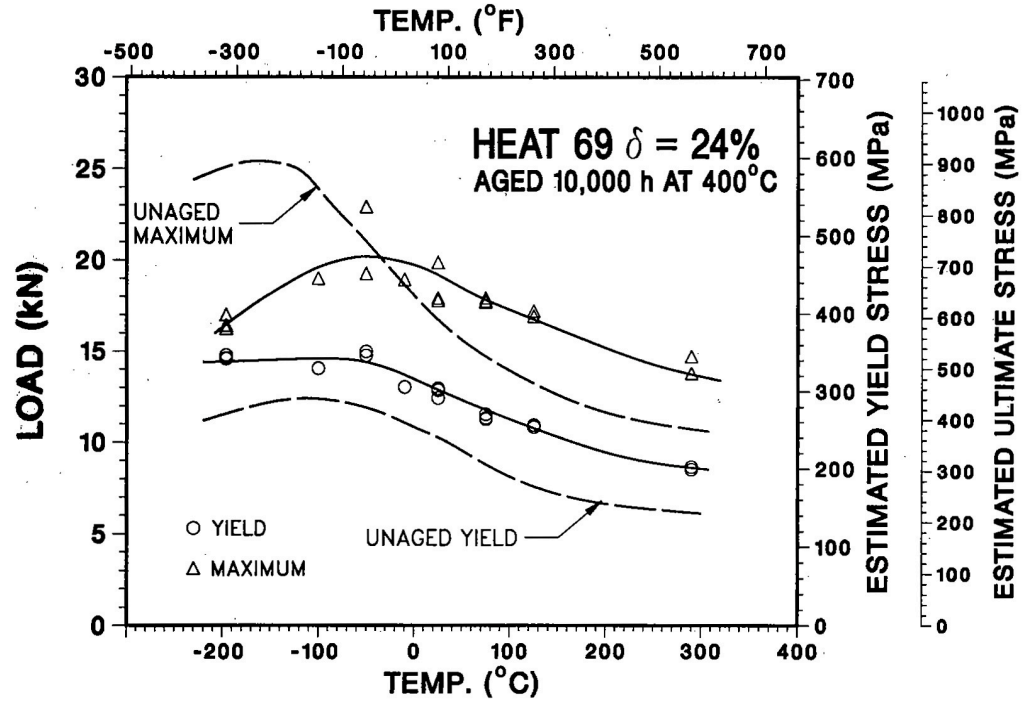

(a)

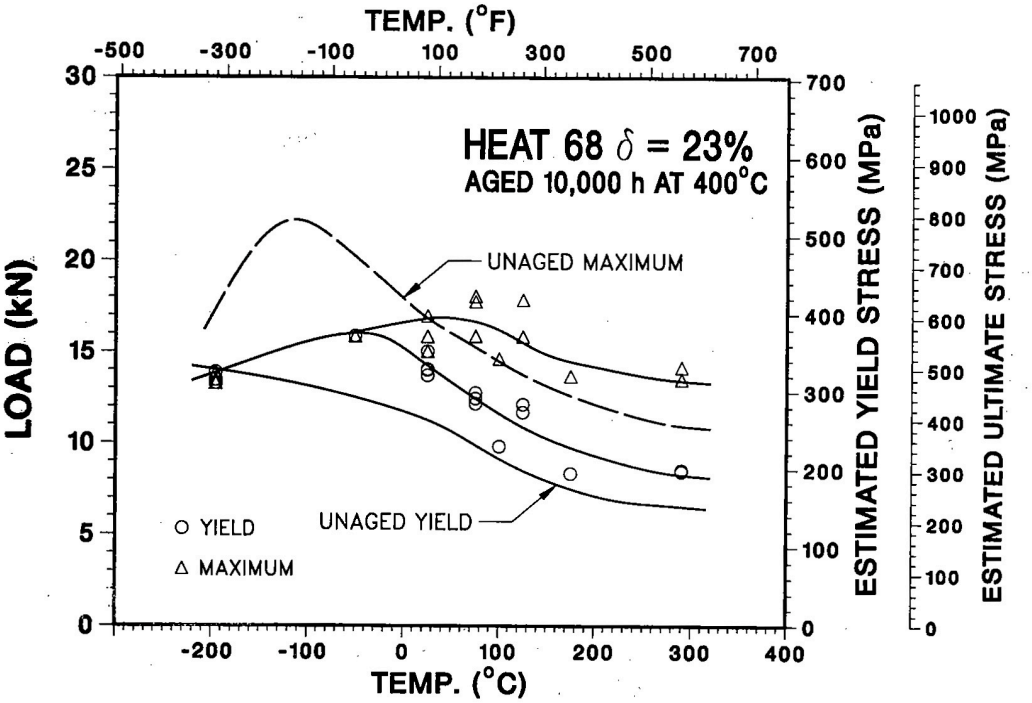

(b)

Figure 38. Yield and Maximum Loads from Charpy Impact Tests for (a) CF–3 and (b) CF–8 Cast Stainless Steel Aged for 10,000 h at 400°C.

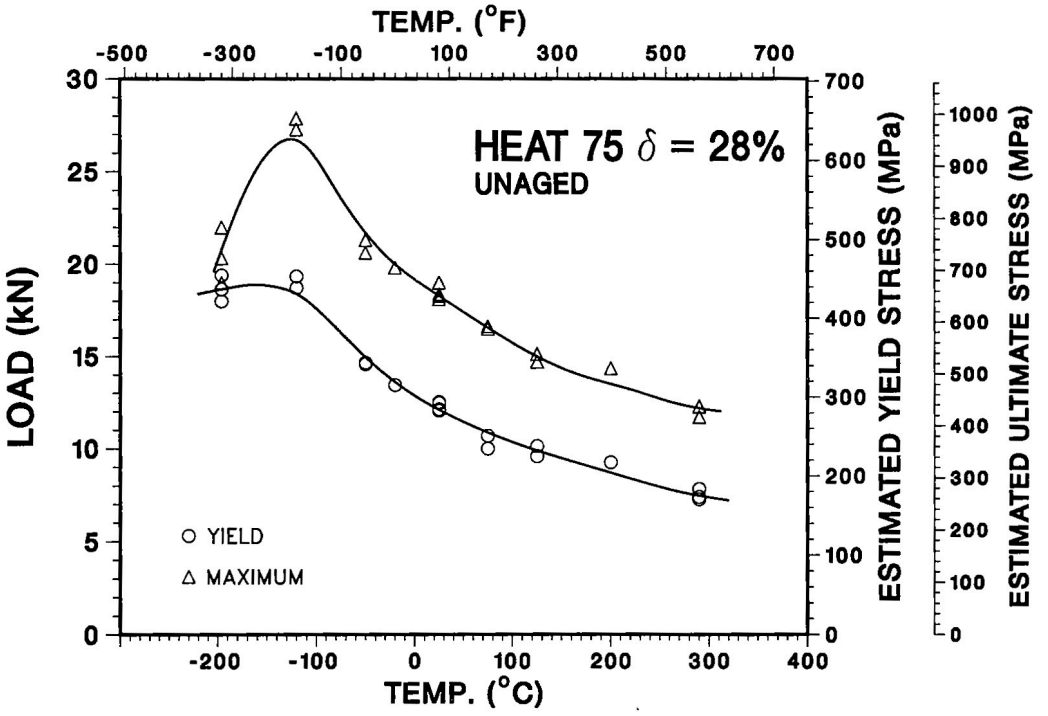

(a)

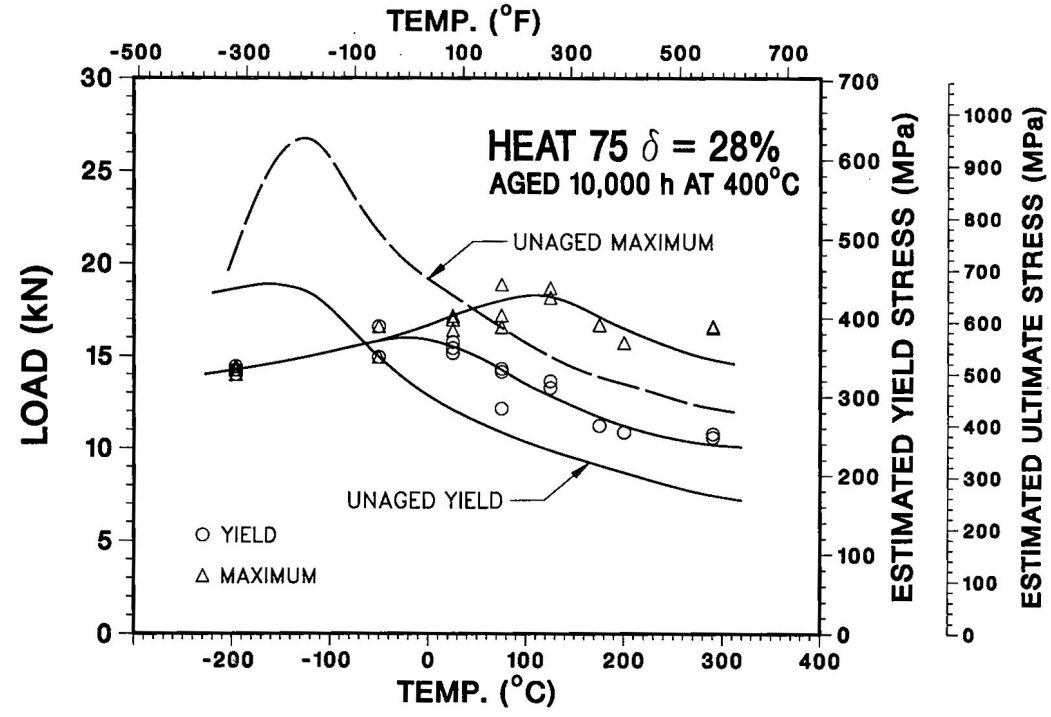

(b)

Figure 39. Yield and Maximum Loads from Charpy Impact Tests for (a) Unaged and (b) Aged CF–8M Cast Stainless Steel.

The fracture toughness results are consistent with the Charpy-impact data, i.e., unaged and aged materials that show low impact strength also exhibit lower fracture toughness. The J_{IC} values and Charpy V-notch impact energies obtained at room temperature are plotted in Fig. 40a. Results from the studies at Westinghouse (WH),[10] FRA,[11,28] and EPRI[29] are also shown. For low values of toughness (i.e., J_{IC} <500 kJ/m^2), J_{IC} decreases linearly with impact energy. The average value of J_{IC} as a function of the impact energy is shown as solid line while the dashed line represent a lower–bound value for J_{IC}. The slopes of the average and lower–bound curves are 3.3 and 1.2, respectively. The lower bound agrees well with the correlation between J and KCV proposed for flaw evaluation procedures for ferritic steel piping.[30] Figure 40a indicates that, for materials with room temperature impact energies <30 J/cm^2 (<18 ft·lb), the J_{IC} values would be <40 kJ/m^2 (<230 in.–lb/in.^{2}).

The influence of thermal aging on impact energy at reactor temperatures is difficult to determine accurately from the present data. However, as shown in Fig. 40b there is a reasonable correlation between J_{IC} values at 290°C and room–temperature impact energy. The slope of the lower bound curve for J_{IC} at 290°C is 1.8. Thus, for a specific aging condition, the J_{IC} values at 290°C are 50% higher than that at room temperature.

The tearing modulus also decreases with thermal aging. The tearing modulus and J_{IC} value for various heats and aging conditions are shown in Fig. 41. At both test temperatures, the tearing modulus decreases with a decrease in J_{IC}. The dashed line represents the lower–bound value for T; the slope is 0.36 at both temperatures. Fracture toughness data for other aging conditions, as well as other heats, are being obtained to better establish the correlation between J_{IC}, tearing modulus, and Charpy–impact energy.

4 Mechanisms of Embrittlement

The embrittlement of cast duplex stainless steel results in a brittle fracture associated with either cleavage of the ferrite phase or separation of the ferrite/austenite phase boundary. A schematic representation of the fracture mechanism of cast duplex stainless steel is shown in Fig. 42. The degree of embrittlement and, hence, the toughness of the material, is controlled by the amount of brittle fracture. Cast stainless steels with poor toughness and impact strength exhibit >80% brittle fracture. For some cast steels, although a fraction of the material may fail in a brittle fashion, the surrounding austenite provides ductility and toughness. Such steels have adequate toughness even after long–term aging. A predominantly brittle failure occurs when either the ferrite phase is continuous, e.g., in cast material with large ferrite content, or the ferrite/austenite phase boundary provides an easy path for crack propagation, e.g., in high–carbon cast steels that contain large phase boundary carbides. Consequently, the amount, size, and distribution of the ferrite phase in the duplex structure and the presence of phase boundary carbides are important parameters in controlling the fracture mode of duplex cast stainless steels.

Cleavage of ferrite occurs when the local tensile stress reaches the critical cleavage fracture stress. At low temperatures, (i.e., high values of yield stress), cleavage cracks nucleate in the ferrite in the plastic zone near the notch tip at loads that are below general yielding. At high temperatures (i.e., low values of yield stress), strain hardening is needed to raise the local tensile stress to the cleavage fracture stress. Ductile fracture results when

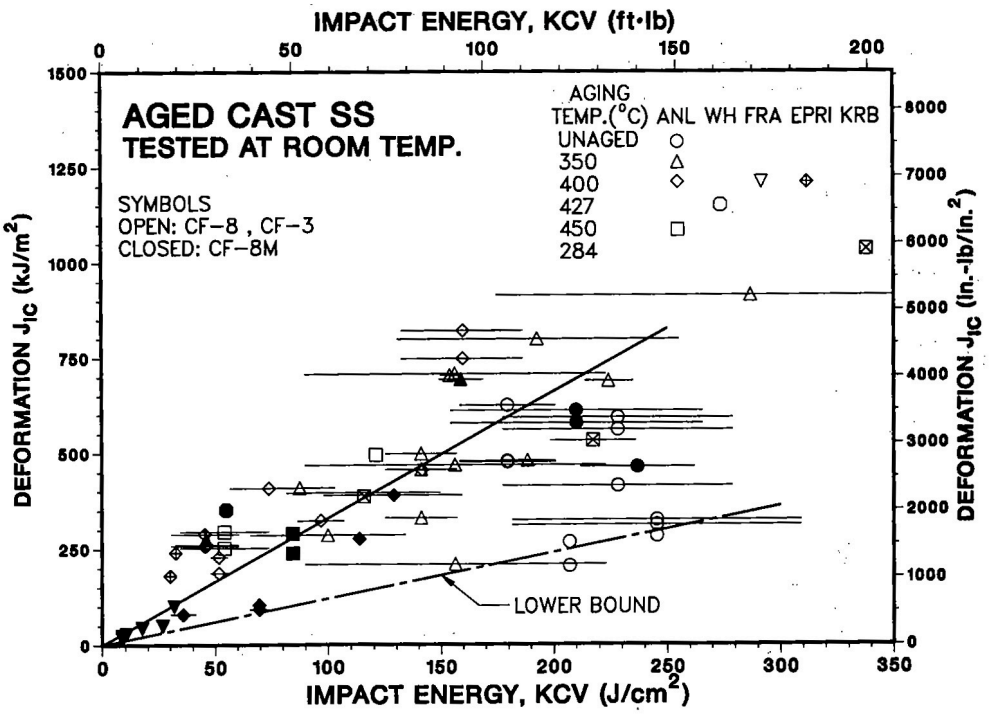

(a)

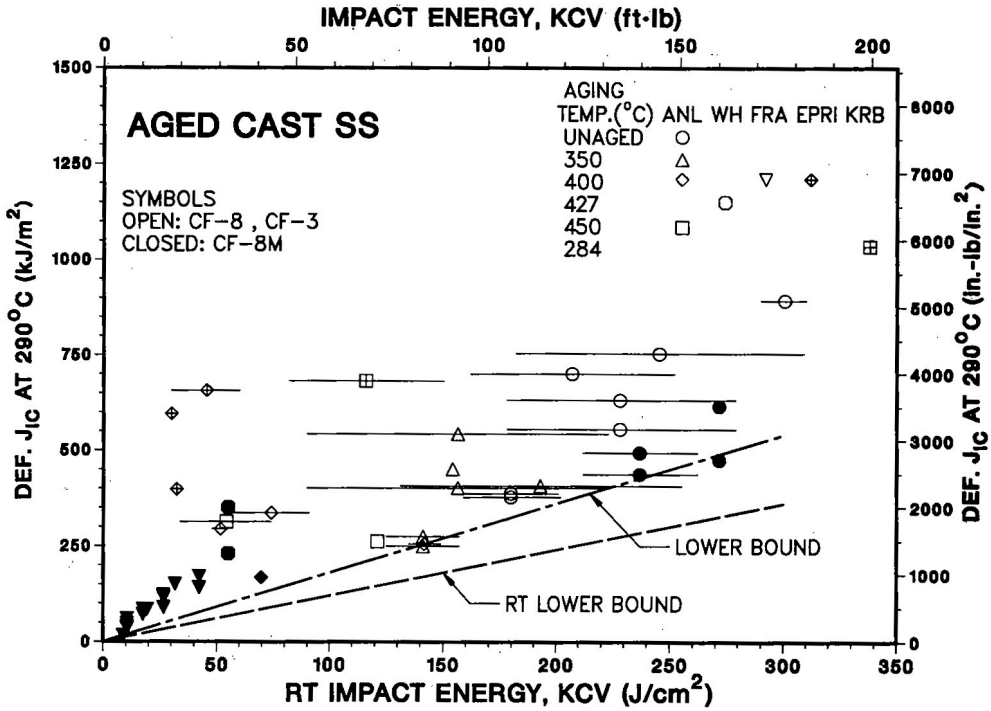

(b)

Figure 40. Correlation between (a) Room Temperature J_{IC} and Impact Energy and (b) J_{IC} at 290°C and Room Temperature Impact Energy for Unaged and Aged Cast Stainless Steel.

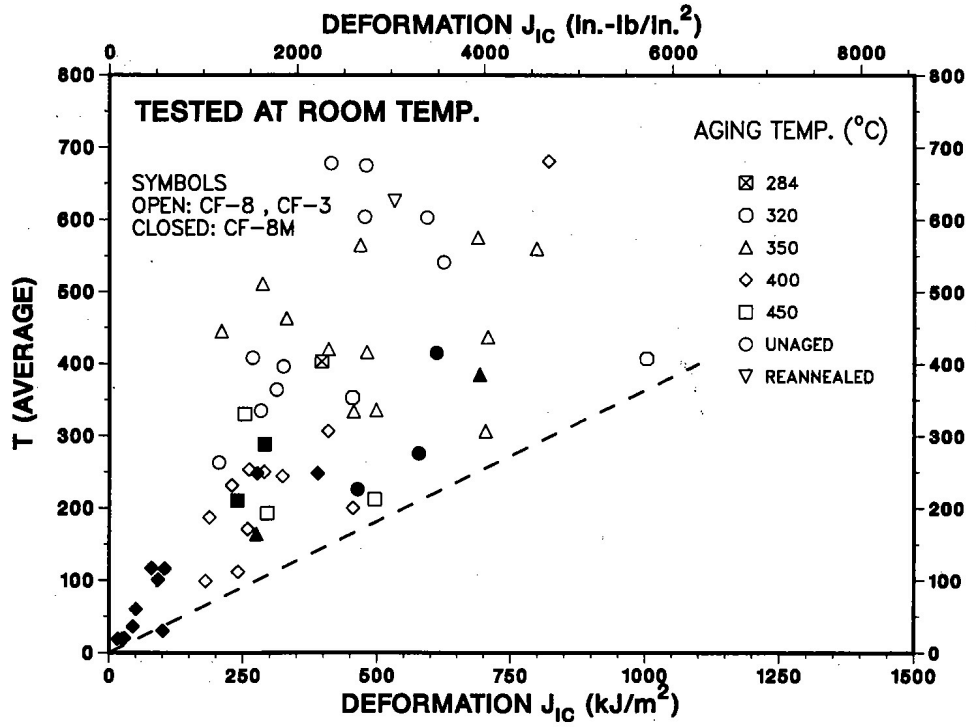

(a)

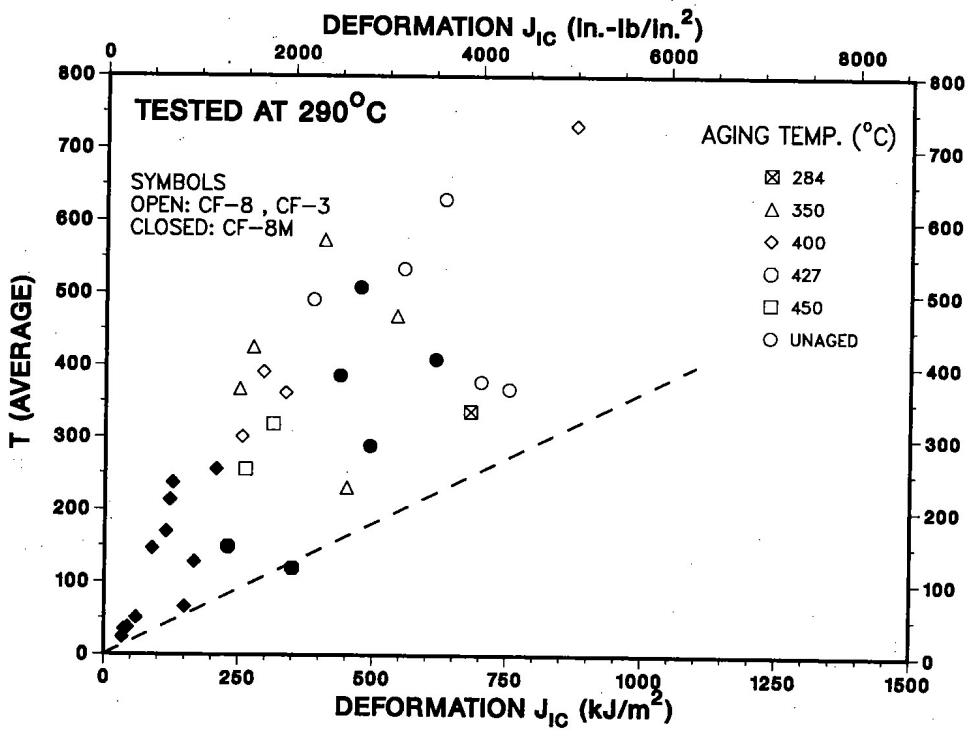

(b)

Figure 41. Correlation between Tearing Modulus and J_{IC} for Unaged and Aged Cast Stainless Steel Tested at (a) Room Temperature and (b) at 290°C.

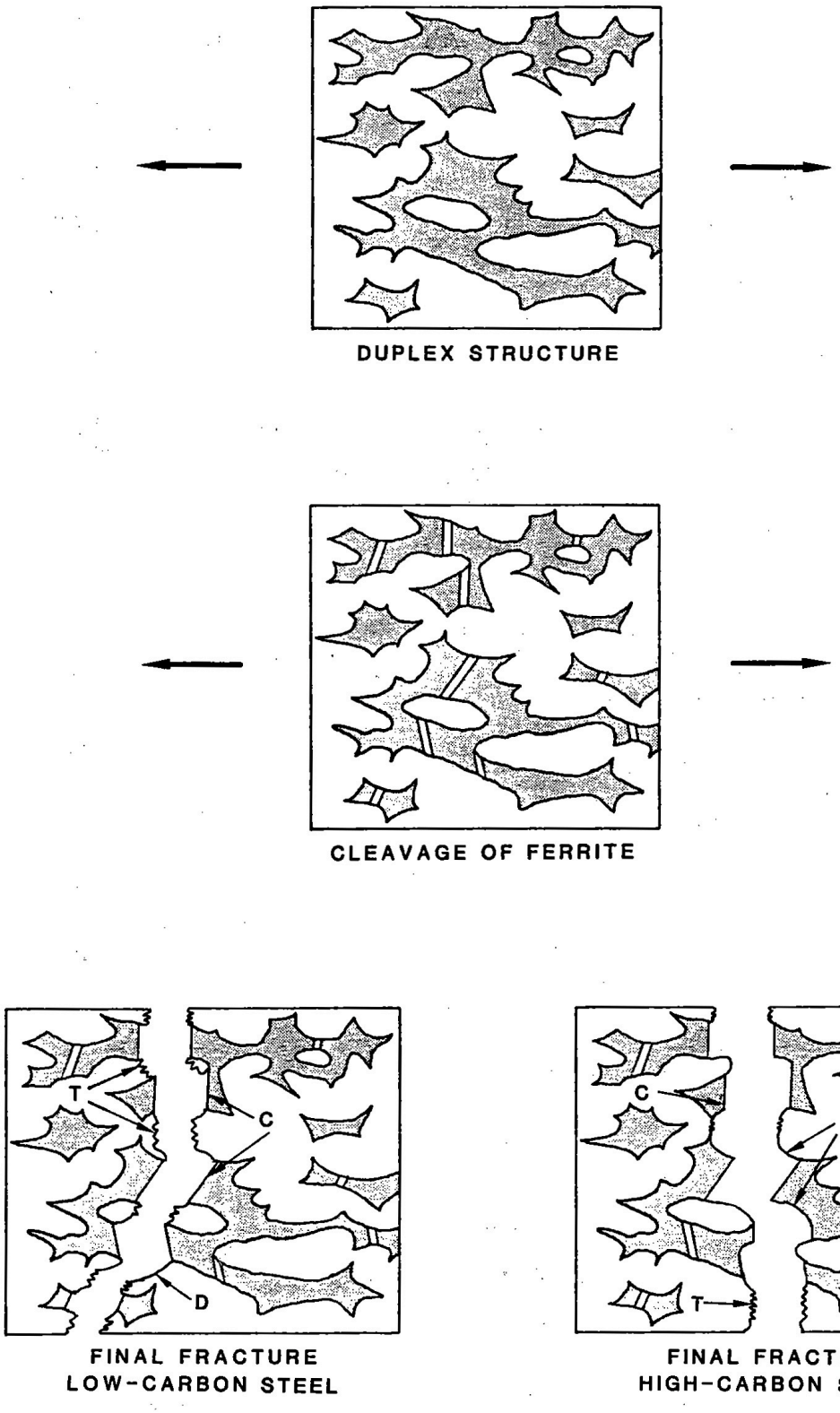

Figure 42. Fracture Mechanisms of Cast Duplex Stainless Steel.

strain hardening is insufficient to raise the tensile stress to the critical value. The relationship between the degree of cleavage fracture and toughness, however, is complex since cleavage cracks can be initiated by several mechanisms, i.e., dislocation pile up, cracking of carbide or nitride particles, and cracking of twin intersections. Each of the mechanisms requires a unique stress level. Thus, for the same amount of cleavage fracture, the toughness may vary in different cast materials.

For unaged cast stainless steels, the critical stress levels for cleavage fracture are achieved only at very low temperatures and the transition temperatures of unaged materials are low. The differences in the transition temperature for the various unaged heats and grades of cast steels are due to the amount of ferrite and the differences in the mechanism of brittle fracture. The high–carbon CF–8 steels have a higher transition temperature because of the presence of phase boundary carbides. The carbides weaken the boundaries and lead to phase boundary separation, an additional low toughness mode of fracture; they also initiate cleavage of ferrite at lower stress levels by carbide cracking. The fracture surfaces of CF–3 and CF–8 steels, Figs. 28 and 30, and the tensile loads, Fig. 37, show the differences in the fracture mode. The transition temperature of CF–8M steels depends on whether or not the material contains phase boundary carbides in the as–cast condition.

Thermal aging of cast stainless steels leads to the precipitation of second–phase particles in the ferrite matrix of the duplex structure. Microstructural studies of cast stainless steels aged at temperatures between 300 and 450°C,[31–33] have identified five phases in the ferrite, i.e., formation of Cr–rich α' phase by spinodal decomposition, nucleation and growth of α', and precipitation of nickel– and silicon–rich G phase, γ_2 (austenite), and $M_{23}C_6$ carbides. The additional phases provide a strengthening mechanism to increase the yield stress. Consequently, the critical stress level for brittle fracture is achieved at higher test temperatures, Figs. 37–39. Large $M_{23}C_6$ carbides and/or Cr_2N nitrides can also precipitate at the ferrite/austenite phase boundaries.[31–33] The presence of phase boundary carbides leads to failure by phase boundary separation. Both these factors, viz., precipitation of additional phases in the ferrite matrix and formation and/or growth of phase boundary carbides, contribute to embrittlement and the observed shift in transition temperature.

The contribution of various precipitate phases to embrittlement of ferrite has been determined from annealing studies conducted to restore the toughness of the embrittled material.[13,32,33] The time-temperature transformation curves for Fe-Cr alloys show that α' is not stable at temperatures ≥550°C.[16] However, the Fe-Cr alloys are embrittled after aging for >10 h at 550°C, owing to the formation of sigma phase.[16] Hence, a short term anneal, e.g., ~1 h, at 550°C, is sufficient to dissolve the α' phase and yet avoid the formation of sigma phase. Microstructural examination of embrittled material, annealed for 1 h at 550°C and water quenched, shows no α' but the size and distribution of the G phase are not affected.[31,33] However, the toughness is virtually restored after the annealing treatment.[13] These results suggest that the formation of α' by spinodal decomposition is the primary mechanism of ferrite embrittlement. Other precipitate phases have a secondary effect on embrittlement. Consequently, the kinetics of two processes, viz., spinodal decomposition of ferrite and carbide or nitride precipitation at phase boundaries, should control the overall kinetics of low–temperature embrittlement of cast stainless steel.

The spinodal decomposition and G–phase precipitation in low–temperature–aged cast duplex stainless steel have been investigated by transmission electron microscopy (TEM),

atom probe field ion microscopy (APFIM), small angle neutron scattering (SANS), and extraction replica techniques.31–38 The activation energy of the spinodal reaction in CF–3 stainless steel is 250 ± 30 kJ/mole (~60 ± 7 kcal/mole).37 This value is comparable to that for chromium diffusion in Fe–Cr alloys and is significantly higher than the activation energy of low–temperature embrittlement obtained from mechanical–property data (i.e., in the range 65 to 200 kJ/mole). The difference cannot be attributed to a competing mechanism associated with phase boundary carbides since carbide precipitation and failure by phase boundary separation do not occur in the low–carbon CF–3 steel. Thus, the lower values of the activation energy of embrittlement of cast stainless steels are most likely due to other factors, such as, the effect of G-phase or γ_2 precipitation in ferrite or changes in the mechanism of cleavage for the aged material.

As discussed above, different mechanism of cleavage of ferrite can occur for the aged cast materials. For example, precipitation of carbides or nitrides at the phase boundaries can initiate cleavage by particle cracking. For aged materials with large second–phase particles, brittle fracture can occur at lower stresses. Consequently, a lower degree of spinodal decomposition, i.e., a smaller amplitude of chromium fluctuation, is needed for a given change in mechanical properties. The material would show a faster reduction in impact strength relative to a material without phase boundary carbides. However, precipitation of carbides or nitrides occurs primarily at 400 or 450°C and is extremely slow at lower temperatures. Thus, the influence of phase boundary carbides would tend to increase the apparent activation energy of embrittlement measured from mechanical–property data.

The other factor that can influence the overall activation energy for embrittlement is the precipitation of other second–phase particles in ferrite, in particular, G phase, a multicomponent phase consisting of nickel, silicon, molybdenum, chromium, iron, and some manganese, and carbon.34,38 The kinetics of G–phase precipitation depend on the chemical composition of the cast material.32,33 For some heats, G phase is observed after times as short as 10,000 h at 400°C, while other heats require up to 70,000 h of aging at 400°C for G–phase formation. In general, precipitation of G phase is faster in the molybdenum–containing CF–8M steels.31–33,38 The aging conditions for which G phase has been detected by TEM or SANS techniques, in various cast stainless steels, are shown in Fig. 43. The kinetics for the decrease in the Charpy impact energy of the aged cast stainless steel are also plotted in the figure. The actual aging times for a given decrease in impact energy (shown by the horizontal scatter bars in Fig. 43) varied significantly for the various heats. Generally, the aging times for the CF–8M steels were lower than those for the CF–3 or CF–8 steels.

At 400°C, the reduction in impact energy appears to be essentially complete before G phase is detected in any of the heats. For example, G phase was not detected in any of the heats aged for 3,000 h, whereas an 80% reduction in impact energy occurred by 4,600 h in all heats. However, at temperatures <350°C, G–phase precipitation and the decrease in impact energy occurred simultaneously. At 320°C, only a 50% reduction in strength occurred in most heats by 30,000 h, and G phase was observed in the specimens. These results indicate that the influence of G–phase precipitation on embrittlement would be greater at low temperatures, since at 400°C, the kinetics of spinodal decomposition are much faster than G-phase precipitation, which follows nucleation and growth.

The exact nature of the effects of G phase on embrittlement are not well understood. The precipitation of G phase can influence the kinetics of embrittlement by either directly altering the kinetics of spinodal decomposition or by changing the deformation and fracture

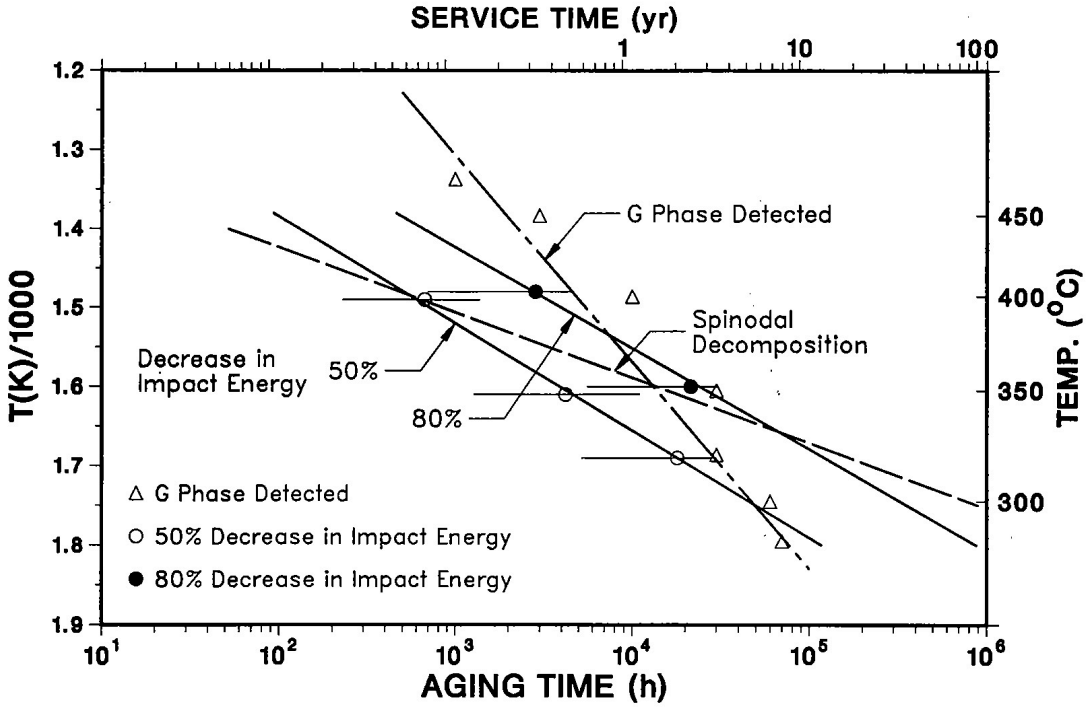

Figure 43. Arrhenius Plots for the Precipitation of G Phase and Reduction in Charpy–Impact Energy for Aged Cast Stainless Steels.

behavior of the ferrite matrix and thereby influencing the effectiveness of spinodal decomposition. The only experimental data on the kinetics of spinodal decomposition in cast duplex stainless steel were obtained by modeling the amplitude of chromium fluctuations, measured by APFIM, in aged CF–3 steel.37 The results yield an activation energy of 250 kJ/mole. No G phase was observed in the steel after 5,000 h at 400 or 350°C. As shown in Fig. 43, most heats require ≥10,000 h at 400°C and ≥30,000 h at 350°C before G–phase precipitates are detected. APFIM studies on aged cast materials that exhibit low activation energy for embrittlement and also contain G phase are needed to establish the effect of G–phase precipitation on the kinetics of spinodal decomposition.

The low values of activation energy obtained from mechanical property data can be attributed to the effect of G–phase precipitation on the deformation behavior of the ferrite matrix. The concomitant precipitation of G phase may alter the frequency (spacing) of chromium fluctuations produced by spinodal decomposition. The strengthening behavior due to second–phase particles depends both on the size and spacing of the particles. A finer dispersion of chromium fluctuations would be more effective in strain hardening. Thus, a lower degree of spinodal decomposition, i.e., a lower amplitude of the chromium fluctuations, would be needed for a given change in mechanical properties; embrittlement would be faster. APFIM studies on CF–8M steels indicate that the spacing of chromium fluctuations is finer for samples aged at 350°C than those aged at 400°C.** However, the results have not been correlated with either G phase precipitation or the kinetics of embrittlement.

** M. Guttmann, EdF, private communications, October 1987.

Another possible effect is the depletion of nickel and molybdenum from the ferrite matrix. The ferrite matrix typically contains ~5% nickel. The presence of nickel in single–phase Fe–Cr alloys is known to promote spinodal decomposition,17 but, alloys with >4% nickel take longer to embrittle than the alloys with <4% nickel.18 For example, the times for 80% reduction in impact energy (measured at 0°C) after aging at 400 and 425°C, respectively, were ~43 and 15 h for an Fe–26Cr alloy and ~123 and 42 h for an Fe–26Cr–6Ni alloy,18 i.e., a factor of ~3 slower for the alloy containing nickel. Furthermore, at temperatures between 400 and 475°C, the embrittlement of ferritic steels is faster than that of duplex stainless steels, e.g., the aging time at 427°C to achieve a 20 J impact energy is 100 h for the Fe–18Cr alloy and 20 h for the Fe–18Cr–2Mo alloy.6 The minimum time for 80% reduction in impact strength for cast stainless steels at 427°C is ~450 h, Fig. 43. The seemingly contradictory effects of nickel on spinodal decomposition and embrittlement in Fe–Cr alloys are attributed to the promotion of twinning as a mode of deformation in Fe–Cr alloys containing >4% nickel.18–21 Addition of molybdenum to Fe–Cr alloys also promotes twinning.19,21 Deformation twins in body–centered cubic metals are formed by the motion of partial screw dislocations. Spinodal decomposition of the ferrite inhibits the motion of screw dislocations and, thus, enhances their dissociation into partials, which facilitates twinning.19,20 Although spinodal decomposition is faster in nickel–containing alloys, it is less effective as a strengthening mechanism because of twinning as a mode of deformation, i.e., the strain hardening will be lower for the Fe–Cr alloys with >4% nickel. Consequently, a greater degree of spinodal decomposition, i.e., higher amplitude of the chromium fluctuations, would be needed to increase the local tensile stress above the critical value for brittle fracture. The Fe–Cr–Ni alloys would take longer to embrittle relative to the Fe–Cr alloys.

The precipitation of G phase can change the composition of ferrite, and thus, alter the deformation behavior and fracture mode of aged cast stainless steels. Deformation twins in ferrite are observed in aged cast stainless steels at all test temperatures. Figure 44 shows twins in fractured Charpy specimens of Heat P1 aged for 30,000 h at 350°C and tested at room temperature and 290°C. At high temperatures, the phase boundaries have a jagged appearance and have moved to accommodate the deformation due to twinning. Such adjustments in the phase boundaries are difficult at lower temperatures and cracks can form at twin/phase boundaries or twin/twin intersections. Twin boundary cracks are observed in aged cast steels. Heat P1 has a high activation energy, thus, the contribution of G phase is expected to be negligible. The twinning behavior of heats with low activation energies is being investigated to establish the role of G phase in deformation and fracture mode of aged cast stainless steels.

In summary, the kinetics of low–temperature embrittlement of cast stainless steels are controlled by the kinetics of three processes, viz., spinodal decomposition of ferrite, precipitation and/or growth of existing carbides/nitrides at the ferrite/austenite phase boundaries, and formation of G phase in the ferrite matrix. The spinodal reaction provides a strengthening mechanism necessary to raise the local tensile stress above the critical value for brittle fracture. The degree of spinodal decomposition required for a specific change in mechanical properties depends on deformation and fracture mechanisms. The kinetics of spinodal decomposition follow chemical diffusion in Fe–Cr alloys and have an activation energy between 230 and 250 kJ/mole (55 and 60 kcal/mole). Precipitation of phase boundary carbides facilitates cleavage of ferrite by carbide cracking, and also failure by phase boundary separation. It occurs primarily at aging temperatures >350°C and, therefore, tends to increase the apparent activation energy of embrittlement. An understanding of the effects of G phase on embrittlement is still elusive. In general, aged cast

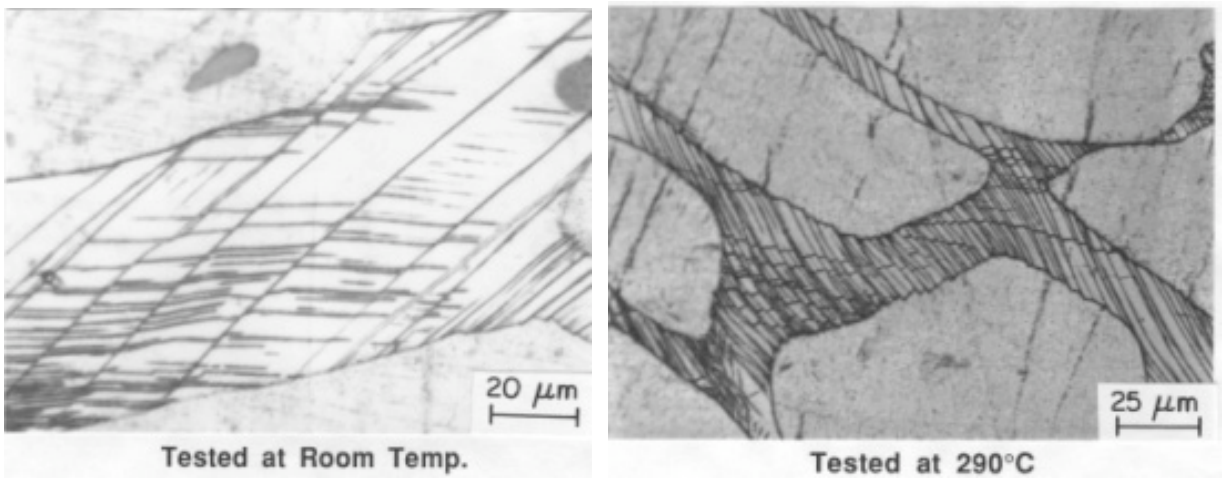

Figure 44.. Deformation Twins in Charpy–Impact Specimens of CF–8 Steel Aged for 30,000 h at 350°C and Tested at Room Temperature and 290°C.

stainless steels that contain G phase exhibit faster kinetics of embrittlement, i.e., the activation energy is low.

The contributions of the three processes on the kinetics of low–temperature embrittlement of cast stainless steels are shown schematically in Fig. 45. Curve A represents the kinetics of single phase Fe–Cr alloys and is primarily controlled by the spinodal reaction, i.e., an activation energy of ~230 kJ/mole (~55 kcal/mole). The influence of nickel is shown in Curve B, which represents cast duplex stainless steels and Fe–Cr alloys containing >4% nickel. Curve B is a translation of curve A to the right; the actual shift would depend

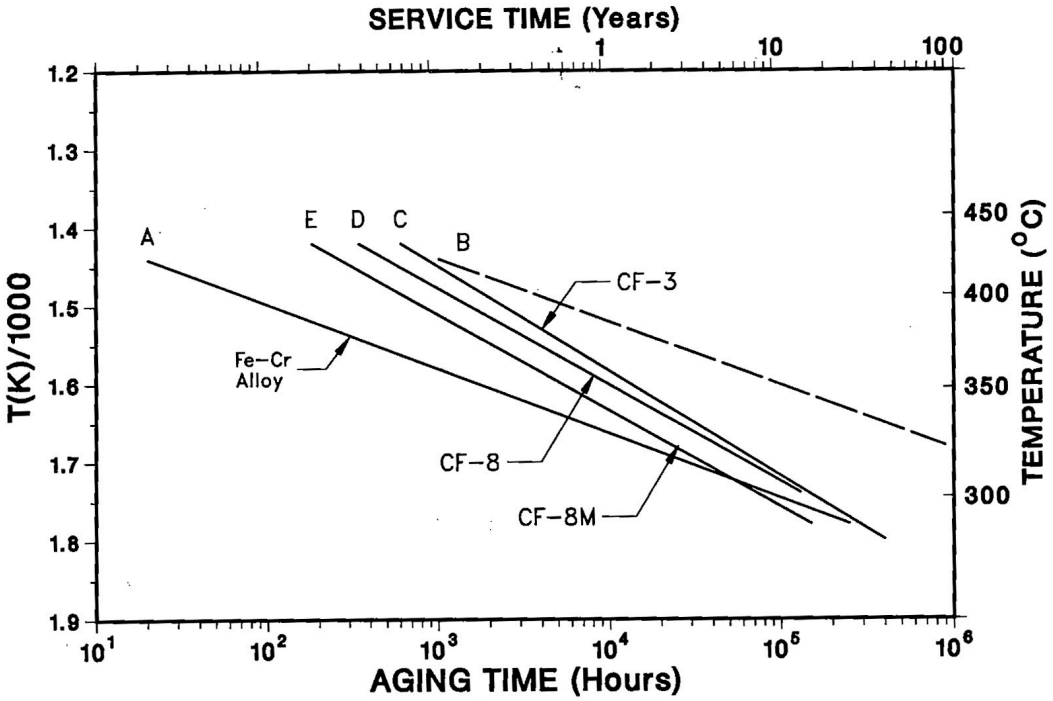

Figure 45. Schematic Representation of the Kinetics of Embrittlement.

on the extent of twinning in the material. This is a hypothetical curve since G–phase precipitation should occur, to some extent, in all alloys containing >4% nickel. The effects of G phase are considered in curve C, which represents CF–3 steels. Since G–phase precipitation is slower than spinodal decomposition at high temperatures and comparable at reactor temperatures, the apparent activation energy of embrittlement will be lower than that for spinodal decomposition, depending on the extent of G–phase precipitation, i.e., in the range of 70–230 kJ/mole (17–55 kcal/mole). The kinetics of embrittlement for high–carbon CF–8 steels would be influenced by phase boundary carbides; these are represented by curve D. The activation energy for CF–8 steels will depend on the extent of G phase and phase boundary carbide precipitation. The kinetics of CF–8M steels are represented by curve E. Since molybdenum is known to accelerate the spinodal reaction, curve E is a lateral shift of curve D to the left.

5 Correlations and Estimation of Embrittlement

5.1 Extent of Embrittlement

The Charpy–impact data were analyzed to obtain a correlation between material variables and the extent of embrittlement, i.e., minimum impact energy [K_m in Eq. (3)] that would ever be achieved after long–term aging. It is well established that the extent of embrittlement increases with an increase in the ferrite content of the cast stainless steel. Furthermore, Charpy–impact data for several heats of CF–8 and CF–8M steels, aged for 10,000 h at 350 or 400°C, indicate that the impact energy decreases with an increase in the Cr content, irrespective of the ferrite content of the steel.† A better correlation was obtained when the total concentration of ferrite formers (i.e., Cr, Mo, and Si) is considered. A sharp decrease in impact energy occurs when either the Cr content exceeds 18 wt.% or the concentration of Cr + Mo + Si exceeds 23.5 wt.%. The concentrations of C and N in the steel also increase the extent of embrittlement because of their contribution to phase–boundary carbides or nitrides and the subsequent fracture by phase–boundary separation. Consequently, an exponential function of the various material variables was used to analyze the data on the minimum room–temperature impact energy. Best–fit curves of the data were obtained with a material parameter Φ given by

$$\Phi = \delta_m^2 \, (C + 0.4\, N) \, (Cr + Mo + Si) \, \lambda \, / \, 1000, \qquad (6)$$

where the measured ferrite content δ_m is in %, the Cr, Mo, Si, C, and N contents are in wt.%, and the mean ferrite spacing λ is in μm. The results indicate that both the amount and spacing of ferrite influence the extent of embrittlement. A similar correlation, but without the effect of ferrite spacing, has been proposed earlier by investigators at Electricité de France (EdF).

Minimum impact energy is plotted as a function of the material parameter Φ in Fig. 46. Results from the studies at FRA,[28] Central Electricity Generating Board (CEGB),[37] and EPRI[29] are also shown in the figure. In most cases, the data show a good correlation with the material parameter. However, the impact energy for one of the FRA heats (4331) is

† M. Guttmann, EdF, private communication, October 1987.

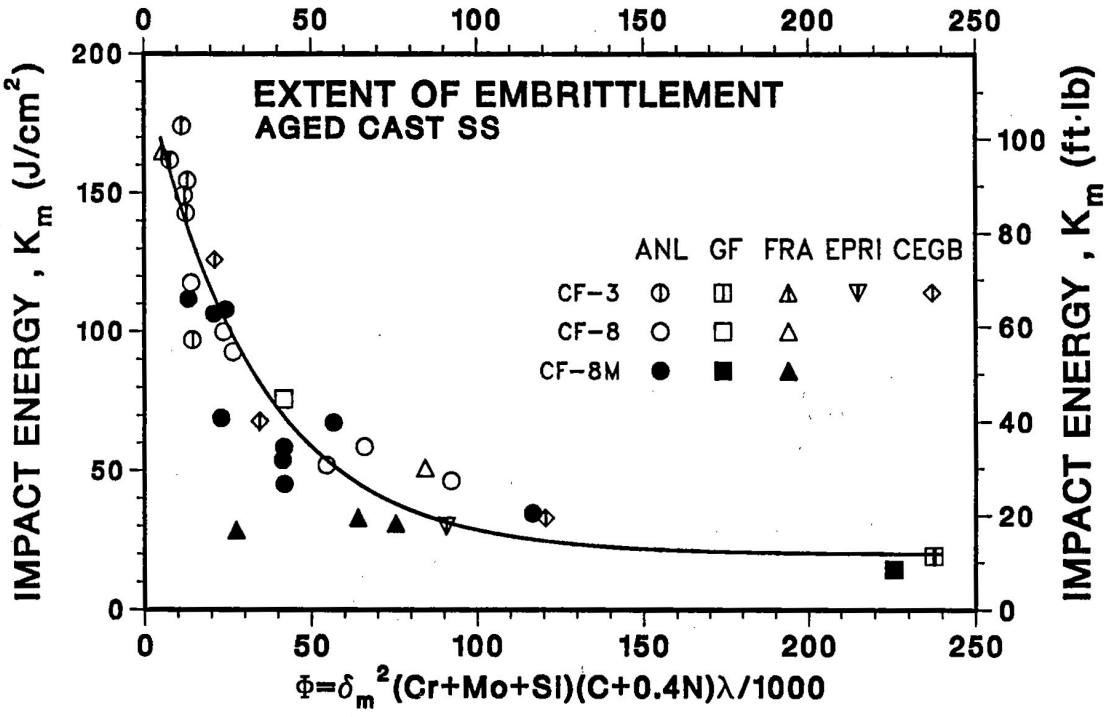

Figure 46. Correlation between Minimum Room Temperature Impact Energy and Material Parameter Φ for Aged Cast Stainless Steel.

significantly lower than that predicted from Fig. 46. This heat contains 0.2% Nb. The fracture surface of the impact test specimen (Fig. 47) shows that the phase boundaries are decorated with very large Nb carbides that crack easily. The large phase–boundary carbides alter the deformation and fracture behavior of the material, i.e., initiation of cleavage by carbide cracking. A difference in fracture mode is reflected in the values of the yield and maximum loads for the instrumented Charpy tests, shown in Fig. 48 for FRA Heat 4331 and Argonne National Laboratory (ANL) Heat 74. The corresponding Charpy transition curves are shown in Fig. 49. Both heats are CF–8M and contain ~20% ferrite, yet the transition

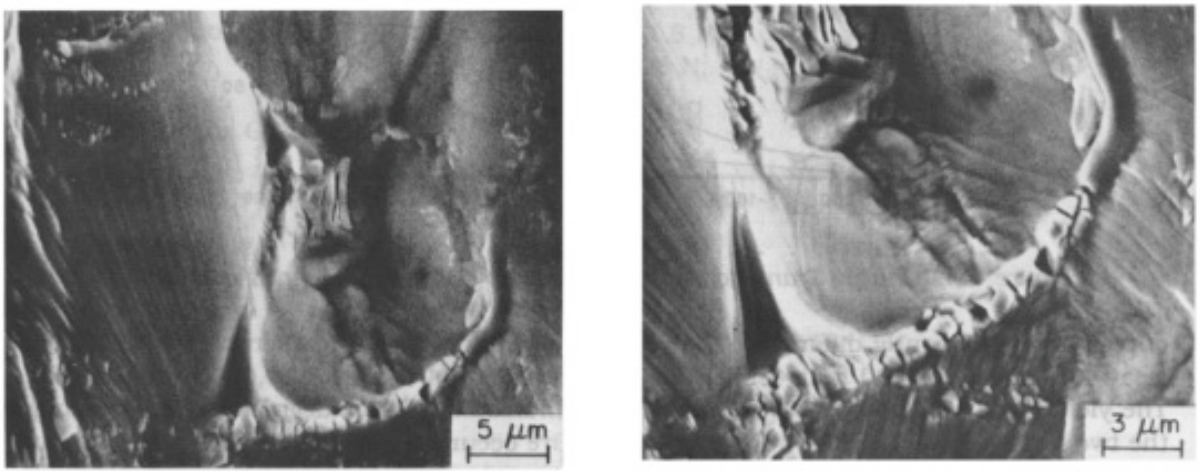

Figure 47. Fracture surface of Charpy–Impact Specimen of FRA Heat 4331 Aged for 700 h at 400°C and Tested at Room Temperature.

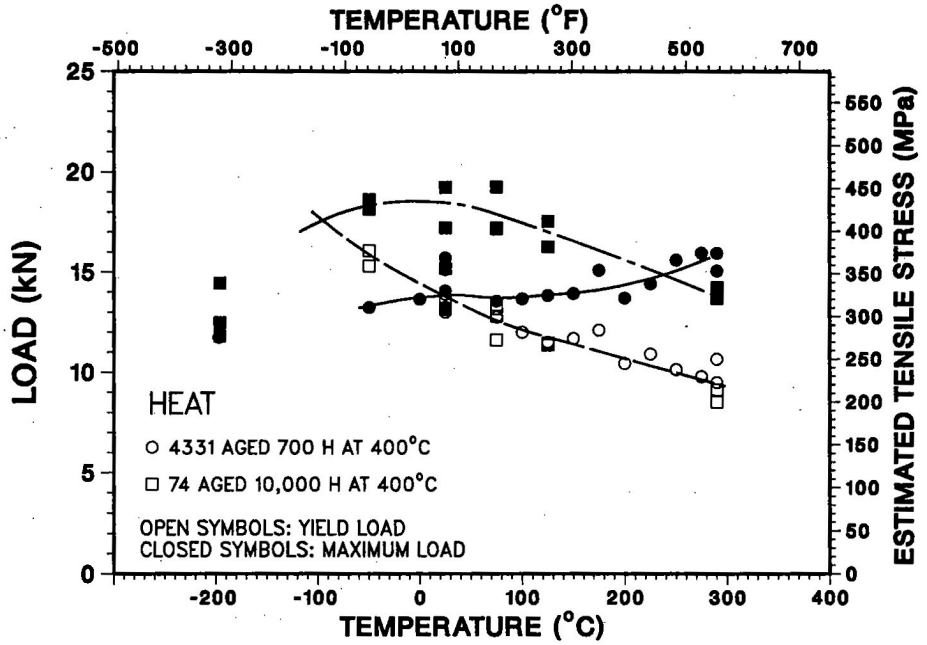

Figure 48. Yield and Maximum Loads from Charpy Data for FRA Heat 4331 Aged for 700 h at 400°C and ANL Heat 74 Aged for 10,000 h at 400°C.

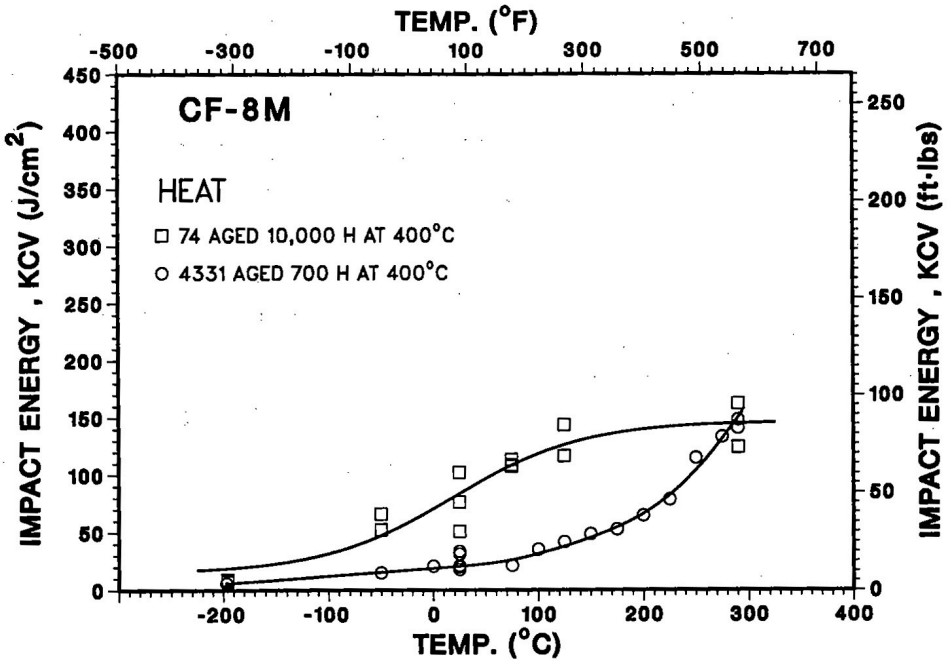

Figure 49. Charpy Transition Curves for Heats 4331 and 74 Aged at 400°C.

curves are significantly different. The 65–J (~50 ft·lb) transition temperature is 220°C for Heat 4331 (aged for 700 h at 400°C) and 20°C for Heat 74 (aged for 10,000 h at 400°C). The yield loads are comparable for both heats, indicating similar degree of strengthening in the two heats. However, Fig. 48 shows that failure occurs at ~14 kN load in Heat 4331 and at ~18 kN load in Heat 74. The difference in the maximum load at failure suggests a difference in fracture mechanism. The present correlation does not consider the effects of Nb on embrittlement.

The correlation indicates that the impact energy will be less than 50 J/cm^2 (~30 ft·lb) for those cast stainless steels for which the material parameter is greater than ~60. For cast stainless steels containing >10% ferrite, the mean ferrite spacing is in the range of 40 to 200 μm; Cr + Mo + Si concentration is ~22% for CF–8 or CF–3 and ~24% for CF–8M stainless steels; and nitrogen content is typically 0.04%. Thus, for cast materials with 0.06% carbon and 100 μm ferrite spacing, the impact energy will be below 50 J/cm^2 when the ferrite content is above 20%. Cast materials with 10 or 15% ferrite can also reach very low impact strength when the ferrite spacing or the nitrogen content is high.

Figure 46 can be used to estimate the extent of embrittlement, i.e., the lowest room temperature impact energy, that would ever be achieved for any given cast stainless steel component. The variables in the material parameter can be determined nondestructively. The compositions are generally known, ferrite content can be calculated from the composition or measured with a magne–gage or ferrite scope (nonsaturation magnetic saturation principle). The ferrite spacing is the variable least readily available; it can be determined by surface replica techniques. However, a conservative estimate of the possible extent of embrittlement can be obtained by assuming the largest value observed in the ANL material data base, i.e., ferrite spacing of ~180 μm for Heat P4 or the KRB pump cover plate.

5.2 Kinetics of Embrittlement

Data from the present study and from FRA[11,28] and GF[8] studies were analyzed to develop a correlation between the activation energy for embrittlement and the chemical composition of the cast material. Initially, all major elements and carbon and nitrogen were included in the correlation. Elements with poor coefficients of correlation were then excluded. The analyses yielded two separate correlations: one for the ANL and FRA data, given by

$$Q(\text{kJ/mole}) = 90.54 + 9.62\,Cr - 8.12\,Ni - 7.53\,Mo + 20.59\,Si - 123.0\,Mn + 317.7\,N$$

or

$$Q(\text{kcal/mole}) = 21.64 + 2.30\,Cr - 1.94\,Ni - 1.8\,Mo + 4.92\,Si - 29.40\,Mn + 75.93\,N; \quad (7)$$

and the other for the GF data, given by

$$Q(\text{kJ/mole}) = -66.65 + 6.90\,Cr - 5.44\,Ni + 8.08\,Mo + 17.15\,Si + 44.1\,Mn + 297.1\,N$$

or

$$Q(\text{kcal/mole}) = -15.93 + 1.65\,Cr - 1.30\,Ni + 1.93\,Mo + 4.10\,Si + 10.54\,Mn + 71.00\,N. \quad (8)$$

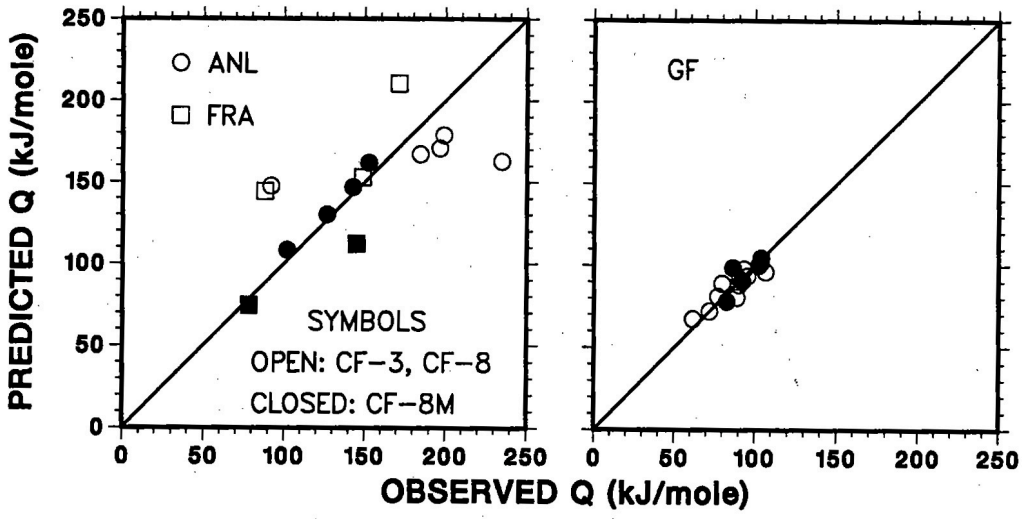

Figure 50. Observed and Predicted Activation Energy of Low–Temperature Embrittlement of Cast Stainless Steel.

The observed and predicted activation energies for the two data sets are plotted in Fig. 50. The coefficients for chromium, nickel, silicon, and nitrogen show the same behavior in the two correlations, however, the constants and the coefficients for molybdenum and manganese have opposite signs.

Equation (7) represents a wide range of material composition and was used to predict the activation energy of two heats of cast material not used in obtaining the correlation. In Fig. 51, the impact energies for the heats are plotted as a function of the aging parameter. The data obtained for different aging temperatures group together fairly well.

The reason why a unified expression could not be obtained for the two data sets is not clearly understood. The GF data set covers a relatively narrow range of compositions and the ferrite contents of most heats are above 30%. The ANL/FRA data set is more representative of compositions defined by ASTM Specification A 351. Furthermore, Eq. (7) accurately predicts the activation energies for heats which were not included in the statistical analyses used to develop the correlations. Activation energies predicted from Eq. (8) are significantly lower than the observed values. Equation (7) also predicts accurately the kinetics of embrittlement observed in the CEGB study on three heats of CF-3 steel.[37]

It is not clear why the two expressions indicate significantly different effects of the constituent elements. The correlations are also not always in qualitative agreement with some of the mechanistic ideas discussed earlier. For example, the contribution of Ni, Si, Mo, and Mn is expected on the basis of their effects on G–phase precipitation. These elements should promote G-phase precipitation, and hence the coefficients for these elements should have a negative sign, since G–phase precipitation decreases the activation energy for embrittlement. The Si coefficient has a positive sign in both expressions, and the Mo and Mn coefficients are positive in Eq. (8). These results indicate that other factors, not included in the analysis, influence the kinetics of embrittlement. The precipitation or growth of phase–boundary carbides or nitrides during aging would increase the apparent activation energy for embrittlement. An increase in C or N in the steel will promote carbide or nitride precipitation and thus increase the activation energy. The positive sign of the

coefficient for N agrees with this behavior; correlation for C content in the steel was poor. A better mechanistic understanding of the variations in activation energy is desirable to avoid "surprises." Information on the role of G phase in embrittlement could provide a unified correlation for all compositions.

6 Recovery Anneal

Tests were conducted to investigate the possibility of recovering the loss of toughness of embrittled cast stainless steel. Studies on ferritic and martensitic steels have shown that the loss of toughness can be recovered by a short–term anneal at 550°C (1022°F). The time–temperature transformation curves for Fe–Cr alloys indicate that the α' phase is not stable at 550°C. However, these alloys are embrittled after aging for >10 h at 550°C owing to the formation of sigma phase. Consequently, the embrittled cast materials were annealed for 1 h at 550°C and water quenched to dissolve the α' and yet avoid the formation of sigma phase. The toughness of cast stainless steel was recovered virtually completely by this heat treatment.[12–14] The dissolution of α' was confirmed by microstructural studies.[32,33]

The Charpy transition curves for the KRB pump cover plate material, after reactor service and subsequent annealing for ~1 h at 550°C and water quenching, are shown in Fig. 52. The data for archive material from the KRB reactor pump cover plate are also included in the figure for comparison.* The results show an essentially complete recovery of toughness. The USE of the material increases from 247 to 330 J/cm^2 after reannealing and the mid–

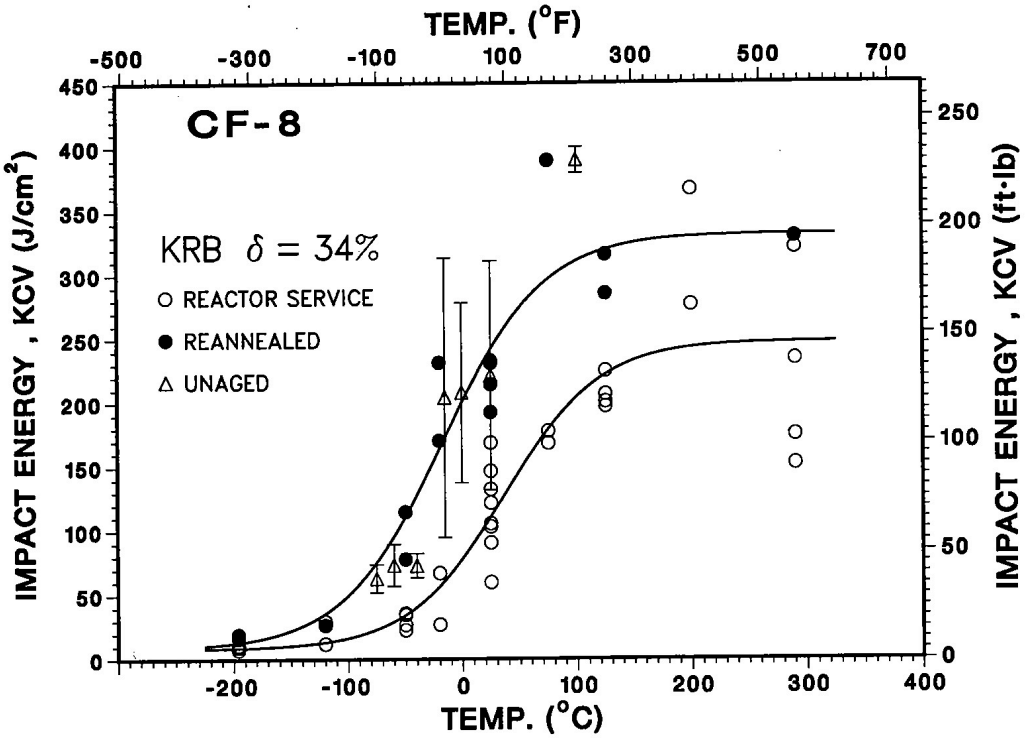

Figure 52. Effect of Reannealing on the Ductile–to–Brittle Transition Curve for the KRB Pump Cover Plate Material.

* A. Trautwein, Georg Fischer Co., private communication, February 1986.

shelf transition temperature decreases from 37 to –16°C. Microstructural examination of the reannealed material showed no α'; however, the size and distribution of the carbides and G phase were essentially the same as in the reactor–aged material.[32,33] These results indicate that formation of α' phase is the primary mechanism for strengthening of the ferrite in cast duplex stainless steels. The microstructural changes are reflected in the fracture mode of the reannealed material.

The fracture surfaces of Charpy specimens of the reactor–aged material, tested at four different temperatures, are shown in Fig. 53. At lower-shelf temperatures, the fracture mode is predominantly phase boundary separation or cleavage and <5% of the fracture

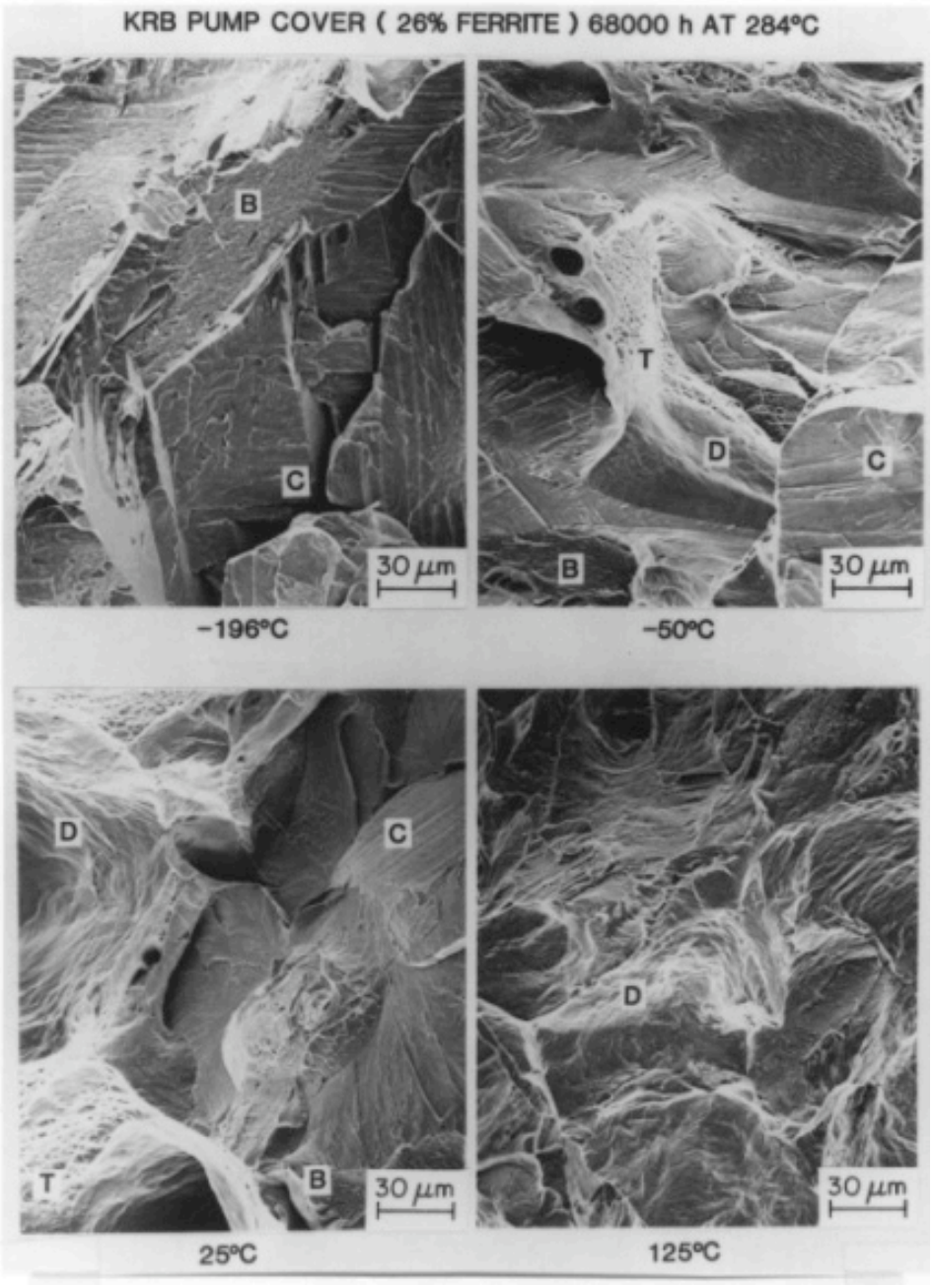

Figure 53. Fracture Surfaces of Impact Test Specimens of the KRB Pump Cover Plate Material Tested at Different Temperatures.

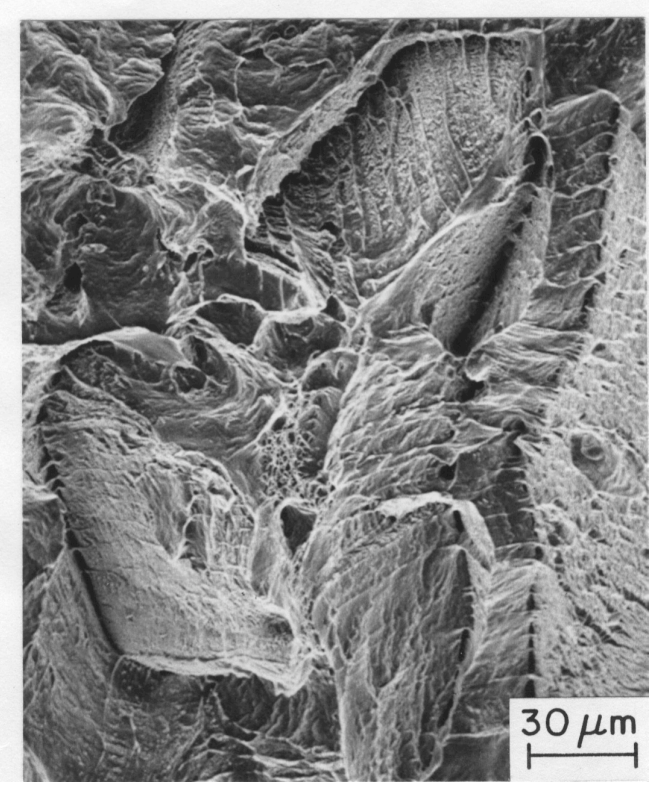

Figure 54.
Fracture Surface of Impact Test Specimen of Reannealed KRB Material Tested at Room Temperature.

surface shows ductile fracture. The amount of ductile fracture increases with an increase in test temperature; at 125°C (257°F), the fracture mode is completely ductile. The fracture surface of the reannealed specimen, tested at room temperature (Fig. 54), shows phase boundary separation and ductile failure. Cleavage of the ferrite phase is not observed. The surface morphology of the regions that fail by phase boundary separation, is, however, different from that seen in the reactor–aged specimens. The boundaries appear to unzip, leaving parallel ridges on the fracture surface. These results indicate that reannealing the material for 1 h at 550°C modifies the phase boundary region.

Tensile tests were also performed on the reannealed material; the results are given in Appendix C. The effect of the recovery anneal on the tensile properties was minimal. The 0.2% yield stress was slightly reduced, but the ultimate stress and reduction in area were essentially the same as for the reactor–aged material.

The recovery annealed material was aged up to 10,000 h at 320, 350, and 400°C. The material reembrittles in a relatively short time, as is shown in Fig. 55. For example, aging for 100 h at 400°C or 3,000 h at 320°C decreased the impact energy to the value observed after reactor service. After 3,000 h of aging at 400°C, the impact energy decreased to ~20 J/cm^2, a value close to the lower–shelf energy for the material.

It is not clear whether this behavior is typical of all reannealed cast stainless steels or is unique to this material. The results are consistent with the mechanisms of embrittlement discussed in Section 4. Since G phase does not dissolve during the recovery anneal, the ferrite matrix is depleted in nickel and spinodal decomposition should be more effective as a strengthening mechanism. Therefore, reembrittlement is faster, as indicated in Fig. 55. Furthermore, as computed from the data in Table 1, the material parameter ϕ for the KRB

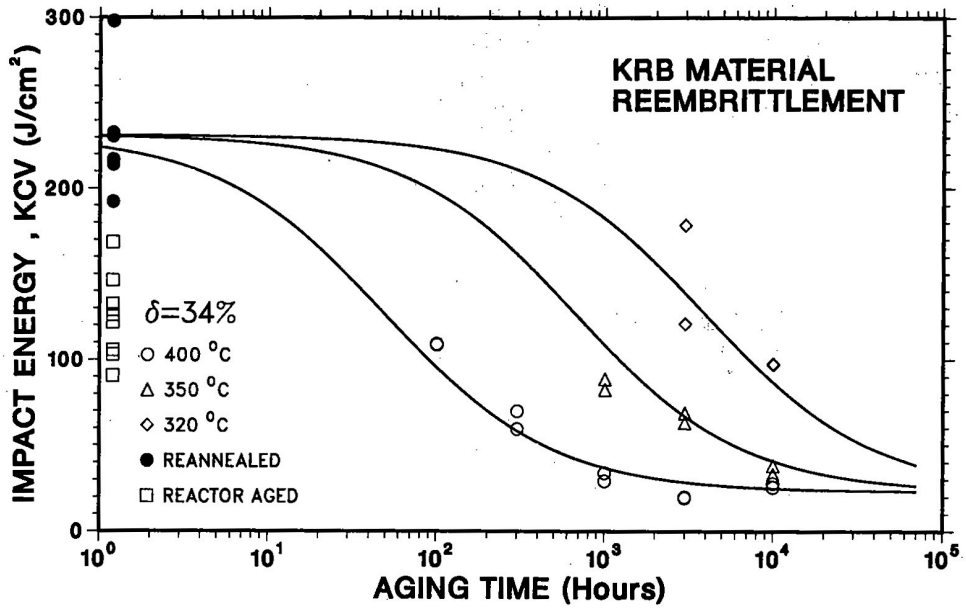

Figure 55. Reembrittlement Behavior of Recovery–Annealed KRB Pump Cover Plate.

material is >200. Figure 46 indicates that the minimum room temperature impact energy for the KRB material is ~20 J/cm^2. This value was obtained for the reannealed and aged specimens. A service time of ~8 yr at 284°C was insufficient to reach this minimum impact energy.

The reembrittlement data yield an activation energy of 180 kJ/mole (43 kcal/mole), a value lower than the 230 kJ/mole expected for chromium diffusion. In the absence of the effects of G–phase or carbide precipitation, the activation energy of embrittlement should be the same as that for spinodal decomposition, i.e., between 230 and 260 kJ/mole. It is possible that G–phase precipitation was not complete after reactor service and continued during the reembrittlement tests. Recovery annealed material from other heats and grades of cast stainless steel are being aged to better establish the reembrittlement behavior.

7 Preliminary Assessment of Embrittlement

The embrittlement of any cast stainless steel component during reactor service can be estimated from the data obtained in the present study and the correlations presented in Section 5. Realistic estimates of impact strength and fracture toughness for a specific heat of cast stainless steel, as a function of time and temperature of reactor service, can be obtained in two steps. First, it is necessary to establish the extent or degree of embrittlement, i.e., the minimum toughness that would ever be achieved for the material after long–term aging, and then the rate of decrease, or the kinetics of embrittlement, can be determined.

The material information required for estimation of the degree of embrittlement is the chemical composition and the ferrite content and spacing. The minimum impact energy K_m, is determined from the correlation between the material parameter ϕ and impact

energy, Fig. 46. At present, only the correlation between room temperature impact energy and material parameter is available. The relationship between reactor temperature impact energy, and material parameter is being developed. The fracture toughness parameters, i.e., J_{IC} and tearing modulus, are estimated from the correlations between J_{IC} and impact energy, Fig. 40, and between tearing modulus and J_{IC}, Fig. 41. In the present study, Heat 75 (CF–8M grade, 29% ferrite) is the worst heat, with a material parameter of 117. Figure 45 predicts a minimum room temperature impact energy of 30 J/cm^2 for the material. Figure 40 yields the average and lower bound J_{IC} values (at room temperature) of 100 and 36 kJ/m^2 (~565 and 205 in.–lb/in.^{2}), respectively. The lower–bound tearing modulus corresponding to the average J_{IC}, from Fig. 41, is 36. A very conservative value of tearing modulus, e.g., 13, is obtained from the lower–bound J_{IC} value.

Figure 46 also indicates that the minimum room temperature impact energy for the worst heat of cast stainless steel can be as low as 20 J/cm^2 (i.e., a material parameter of >200). This corresponds to a lower–bound J_{IC} of 25 kJ/m^2 (143 in.–lb/in.^{2}) and a tearing modulus of 24. Correlations to estimate the toughness at reactor temperatures have not been developed yet. Available data[28] indicate that the lower–bound values of toughness at reactor temperatures are ~50% higher than those at room temperature. These values may be too conservative. The correlations will be validated and refined as the information for material parameter and long–term aging data become available.

The rate of decrease of toughness, i.e., the kinetics of embrittlement can be estimated from Eqs. (1), (3), and (7). The chemical composition and initial impact energy of the cast material is needed for the assessment. The constant β in Eq. (3) is the difference between the initial strength and minimum impact energy, K_m. The activation energy, Q, is determined from Eq. (7). The average value of the constant α in Eq. (3) is 1.0; θ is 3.0 for CF–3 and CF–8 steels and 2.6 for CF–8M steel. The decrease in impact energy, as a function of time and temperature of reactor service, is determined from Eqs. (1) and (3).

Examples of the predicted embrittlement behavior of heats susceptible to embrittlement and typical heats of CF–8M and CF–8 cast stainless steel are shown in Fig. 56. The corresponding J_{IC} and tearing modulus can be determined from Figs. 40 and 41, respectively. The theoretical chemical composition and the ferrite content and spacing of the heats are given in Table 8. All compositions are within ASTM Specification A 351. The compositions of Heats A and C are selected to give high ferrite content and fast kinetics of embrittlement i.e., low activation energy. The mean ferrite spacing for most cast stainless steels with >10% ferrite varies between 40 and 200 μm; the average value for thick castings (e.g., GF heats or the KRB pump cover in Table 1) is ~175 μm. A large value of the ferrite spacing was selected for Heats A and C to obtain a conservative estimate of the extent of embrittlement.

The results show that the impact energies of Heats A and C will decrease to below 40 J/cm^2 (~20 ft·lb) after 4 or 5 yr of service at 320°C. Heats B and D, with lower ferrite content (15%), exhibit much less embrittlement, i.e., the impact energy will not decrease below 90 J/cm^2 even after long–term service. The kinetics of embrittlement are also slower for these heats; the activation energy is >170 kJ/mole (>40 kcal/mole), compared with 75 kJ/mole (18 kcal/mole) for Heats A and C. The results also show that the minimum impact energy is the important factor in estimating the embrittlement behavior. Slow

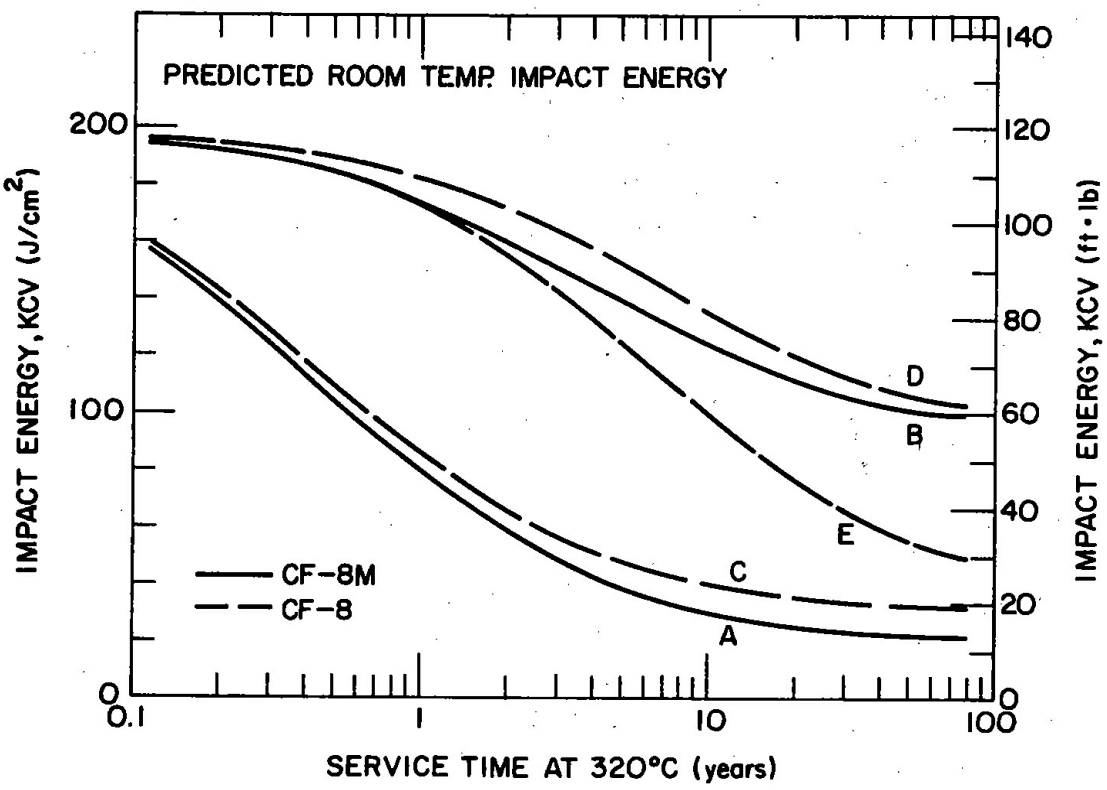

Figure 56. Predicted Embrittlement Behavior of CF–8M and CF–8 Cast Stainless Steel.

Table 8. Theoretical Chemical Composition and Ferrite Morphology of Cast Stainless Steel used for Predicting Embrittlement under LWR Conditions

Heat	Grade	Composition (wt.%)							Ferrite[a]		Q^b	K_m^c
		C	N	Mn	Si	Ni	Cr	Mo	Content (%)	Spacing (μm)	(kJ/mole)	(J/cm^2)
A	CF–8M	0.05	0.02	1.2	1.2	10.0	21.0	2.6	28	180	75	20
B	CF–8M	0.05	0.05	0.5	1.0	9.0	19.5	2.0	15	80	170	90
C	CF–8	0.04	0.02	1.3	0.5	8.4	21.0	0.4	24	200	75	30
D	CF–8	0.05	0.05	0.5	1.0	8.5	20.5	0.4	15	80	188	90
E	CF–8	0.04	0.02	1.3	0.5	8.4	21.0	0.4	24	200	188	30

a Ferrite content calculated from chemical composition with Hull's equivalent factor and ferrite spacings are assumed values.

b Calculated from Eq. (7), value for heat E was arbitrarily assumed.

c Determined from Fig. 46.

kinetics of embrittlement, i.e., high activation energy, delay the decrease in impact strength, but the material would reach the lowest value of impact strength after long–term reactor service. This behavior is seen in Heat E, which has the same material parameters as Heat C, but the activation energy was arbitrarily assumed to be 188 kJ/mole, rather than the calculated value of 75 kJ/mole, to illustrate the effect of slower kinetics. Even with very slow kinetics, the impact energy decreases to ~40 J/cm^2 after ~40 yr of service.

8 Conclusions

Charpy–impact, tensile, and J–R curve data for several experimental and commercial heats of cast stainless steel are presented. The materials were thermally aged up to 30,000 h at temperatures between 290 and 450°C (~555 and 840°F). Aging at these temperatures leads to an increase in tensile strength and a decrease in impact energy, fracture toughness J_{IC}, and tearing modulus of the material. The ductile–to–brittle transition curve shifts to higher temperatures. The J_{IC} values are consistent with the Charpy–impact data, i.e., the relative reduction in impact energy is similar to the relative decrease in J_{IC} values. In general, the low–carbon CF–3 cast stainless steels are the most resistant and molybdenum–containing high–carbon CF–8M steels are the most susceptible to low–temperature embrittlement.

The effects of material variables on the embrittlement of cast stainless steels have been evaluated. The chemical composition of the steel and the ferrite content and spacing are important parameters in controlling the degree and kinetics of embrittlement. The ferrite morphology has a strong effect on the degree or extent of embrittlement. Small changes in the constituent elements of the cast material can significantly alter the kinetics of embrittlement.

The mechanisms of embrittlement of cast duplex stainless steel have been established. Embrittlement is caused by brittle fracture associated with either cleavage of ferrite or separation of ferrite/austenite phase boundaries. The formation of α' phase by spinodal decomposition of the ferrite provides the strengthening mechanism necessary to raise the local tensile stress above the critical value for cleavage. Alternatively, precipitation and/or growth of phase boundary carbides or nitrides leads to brittle failure by phase boundary separation and also facilitates cleavage of the ferrite by particle cracking. The degree of brittle fracture and, hence, the degree of embrittlement of a specific heat of cast stainless steel depends strongly on the amount and spacing of the ferrite in the duplex structure. Cast materials that are sensitive to embrittlement either have a semi–continuous ferrite morphology or are prone to fracture via phase boundary separation. For some materials, although a portion of the material may fail in a brittle fashion, the surrounding austenite provides ductility and toughness, e.g., cast materials with low ferrite content or the low–carbon cast stainless steels.

The kinetics of embrittlement are controlled by three processes, viz., spinodal decomposition, precipitation and growth of phase boundary carbides, and precipitation of G phase in ferrite. Kinetics of the spinodal reaction are controlled by chromium diffusion in the ferrite matrix which has an activation energy of ~230 kJ/mole (~55 kcal/mole). The precipitation of phase boundary carbides occurs at temperatures >350°C and, therefore, tends to increase the activation of embrittlement obtained from mechanical–property data for materials aged at temperatures in the range of 300 to 400°C. The precipitation of G phase

influences embrittlement either by changing the frequency of chromium fluctuations from spinodal decomposition or by altering the mechanisms of deformation and fracture. The kinetics of embrittlement for a specific cast stainless steel depend on the relative contributions of carbide and G–phase precipitation; the activation energies can range between 65 and 230 kJ/mole.

The toughness of cast stainless steels can be recovered by a short-time anneal of 1 h at 550°C and water quenching. However, preliminary data show that the recovery annealed material reembrittles in a relatively short time. Tests are being conducted on different grades of cast materials to better understand the recovery anneal and reembrittlement behavior of cast stainless steels.

Mechanical–property results from the present study and data from other investigations have been analyzed to develop the procedure and correlations for predicting the kinetics and extent of embrittlement of reactor components from known material parameters. A method and examples of estimating the impact strength and fracture toughness of cast components during reactor service are described. The results indicate that the lower–bound values of impact energy, J_{IC}, and tearing modulus at room temperature could be as low as 20 J/cm^2 (12 ft·lb), 25 kJ/m^2 (143 in.–lb/in.^{2}), and 24, respectively. Correlations for estimating the toughness at reactor temperatures have not been developed yet. Available data indicate that the lower–bound values of toughness at reactor temperatures are ~50% higher than those at room temperature. These values are probably very conservative for most materials. The present analysis has focussed on assuring that the correlations are adequately conservative for "bad" heats. Mechanical property data will be reanalyzed to try to develop correlations for more typical materials. The correlations will be validated and refined as the information on material parameters and data on long–term aging become available.

9 Acknowledgments

This work was supported by the Office of the Nuclear Regulatory Research, U. S. Nuclear Regulatory Commission. The authors are grateful to L. P. Burkle, W. K. Soppet, and C. Ensel for conducting the mechanical tests and to G. M. Dragel and L. Bush for contributions to the experimental effort. The authors also thank J. Muscara, W. J. Shack, and T. F. Kassner for their helpful discussions.

References

1. J. J. Heger, "885°F Embrittlement of the Ferritic Chromium–Iron Alloys," *Met. Progress*, p. 55 (1951).

2. R. M. Fisher, E. J. Dulis, and K. G. Carroll, "Identification of the Precipitate Accompanying 885°F Embrittlement in Chromium Steels," *Trans. AIME* **197**, 690 (1953).

3a. R. O. Williams, "Further Studies of the Iron–Chromium System," *Trans. AIME* **212**, 497 (1958).

3b. R. O. Williams and H. W. Paxton, “The Nature of Aging of Binary Iron–Chromium Alloys Around 500°C,” *J. Iron and Steel Inst. London* **185**, 358 (1957).

4. M. J. Marcinkowski, R. M. Fisher, and A. Szirmae, “Effect of 500°C Aging on the Deformation Behavior of an Iron–chromium Alloy,” *Trans. AIME* **230**, 676 (1964).

5. R. Lagneborg, “Metallography of the 475°C Embrittlement in an Iron–30% Chromium Alloy,” *Trans. ASM* **60**, 67 (1967).

6. P. J. Grobner, “The 885°F (475°C) Embrittlement of Ferritic Stainless Steels,” *Metall. Trans*. **4**, 251 (1973).

7. T. J. Nichol, A. Datta, and G. Aggen, “Embrittlement of Ferritic Stainless Steels,” *Metall. Trans*. **11A**, 573 (1980).

8. A. Trautwein and W. Gysel, “Influence of Long Time Aging of CF–8 and CF–8M Cast Steel at Temperatures Between 300 and 500°C on the Impact Toughness and the Structure Properties,” *Spectrum, Technische Mitteilungen aus dem+GF+Konzern*, No. 5 (May 1981); in *Stainless Steel Castings,* V. G. Behal and A. S. Melilli, eds., ASTM STP 756, Philadelphia, 1982 pp. 165–189.

9. G. Baudry and C. Pichard, “Evolution during Long Holding Times at 300 and 450°C of the Mechanical Properties of Austeno–Ferritic Steel Castings and Welded Joints Used in Pressurized Water Nuclear Reactors,” in *Troisieme Congress National sur la Technologie des Appareils a Bression*, Vol. 2, Materiaux, A.F.I.A.P., 1980, p. 673.

10. E. I. Landerman and W. H. Bamford, “Fracture Toughness and Fatigue Characteristics of Centrifugally Cast Type 316 Stainless Steel Pipe after Simulated Thermal Service Conditions,” in *Ductility and Toughness Considerations in Elevated Temperature Service*,” ASME MPC–8, New York, 1978, pp. 99–125.

11. G. Slama, P. Petrequin, and T. Magep, “Effect of Aging on Mechanical Properties of Austenitic Stainless Steel Castings and Welds,” presented at SMIRT Post–Conference Seminar 6, *Assuring Structural Integrity of Steel Reactor Pressure Boundary Components*, August 29–30, 1983, Monterey, CA.

12. O. K. Chopra and H. M. Chung, “Aging Degradation of Cast Stainless Steels: Effects on Mechanical Properties,” in *Environmental Degradation of Materials in Nuclear Power Systems – Water Reactors*, G. J. Theus and J. R. Weeks, eds., The Metall. Soc., Warrendale, 1988, pp. 737–748.

13. O. K. Chopra and H. M. Chung,, “Effect of Low–Temperature Aging on the Mechanical Properties of Cast Stainless Steels,” in *Properties of Stainless Steels in Elevated Temperature Service*, M. Prager, ed., MPC–Vol. 26/PVP–Vol. 132, ASME, New York, 1988, pp. 79–105.

14. O. K. Chopra and H. M. Chung, “Initial Assessment of the Processes and Significance of Thermal Aging in Cast Stainless Steels,” in *Proc. 16th Water Reactor Safety Information Meeting*, U. S. Nuclear Regulatory Commission, NUREG/CP–0097 Vol. 3, p. 519 (March 1989).

15. H. D. Solomon and T. M. Devine, “Influence of Microstructure on the Mechanical Properties and Localized Corrosion of a Duplex Stainless Steel,” in *Micon 78: Optimization of Processing, Properties, and Service Performance through Microstructural Control*, H. Abrams, G. N. Maniar, D. A. Nail, and H. D. Solomon, eds., ASTM STP 672, 1979, p. 430.

16. H. D. Solomon and T. M. Devine, Jr., “Duplex Stainless Steels – A Tale of Two Phases,” in *Duplex Stainless Steels*, R. A. Lula, ed., ASM, Metals Park, 1983, pp. 693–756.

17. H. D. Solomon and L. M. Levinson, “Mössbauer Effect Study of 475°C Embrittlement of Duplex and Ferritic Stainless Steels,” *Acta Metall.* **26**, 429 (1978).

18. K. Nakano, M. Kanao, and A. Hoshino, “Effect of Nickel Content and the Austenite Phase on Low Temperature Toughness and Embrittlement Behavior of Fe–26%Cr Alloys,” *Trans. Nat. Res. Inst. Met.* **20**, 1 (1978).

19. T. Magnin and F. Moret, “Mechanical Twinning in Ferritic Stainless Steels,” *Scripta Met.* **16**, 1225 (1982).

20. T. Magnin, J. LeCoze, and A. Desestret, “Twinning and Stress Corrosion Cracking of Ferritic Phase of Duplex Stainless Steels,” in *Duplex Stainless Steels*, R. A. Lula, ed., Metals Park, ASM, 1983, pp. 535–552.

21. M. Anglada. M. Nasarre, and J. A. Planell, “High Temperature Mechanical Twinning of Two Fe–Cr–Mo–Ni Ferritic Stainless Steels,” *Scri. Metall*. **21**, 931 (1987).

22. A. Hendry, Z. F. Mazur, and K. H. Jack, “Influence of Nitrogen on 475°C Embrittlement of High–chromium Ferritic Steels,” *Met. Sci.*, Vol. **13**, 482 (1979).

23. M. Courtnall and F. B. Pickering, “The Effect of Alloying on 475°C Embrittlement,” *Met. Sci.* Vol. **10**, 273 (1976).

24. A. W. Bowen and G. M. Leak, “Diffusion in BCC Iron Base Alloys,” *Metall. Trans.* **1**, 2767 (1970).

25. A. L. Hiser, *Tensile and J–R Curve Characterization of Thermally Aged Cast Stainless Steels*, NUREG/CR–5024, MEA–2229, Materials Engineering Associates, Inc., (September 1988).

26. A. L. Hiser, F. J. Loss, and B. H. Menke, *J–R Curve Characterization of Irradiated Low Upper Shelf Welds*, U. S. Nuclear Regulatory Commission Report NUREG/CR–3506 (April 1984).

27. W. L. Server, “Impact Three–Point Bend Testing for Notched and Precracked Specimens,” *J. Test. Eval.* **6**, 29 (1978).

28. Y. Meyzaud, P. Ould, P. Balladon, M. Bethmont, and P. Soulat, “Tearing Resistance of Aged Cast Austenitic Stainless Steel,” presented at *Intl. Conf. on Thermal Reactor Safety* (NUCSAFE 88), October 1988, Avignon, France.

29. P. McConnell and J. W. Sheckherd, *Fracture Toughness Characterization of Thermally Embrittled Cast Duplex Stainless Steel*,"Electric Power Research Institute Report NP–5439, Palo Alto, CA (September 1987).

30. A. Zahoor, R. M. Gamble, H. S. Mehta, S. Yukawa, and S. Ranganath, "Evaluation of Flaws in Carbon Steel Piping," Electric Power Research Institute Report NP–4824M, Palo Alto, CA (October 1986).

31. H. M. Chung and O. K. Chopra, "Microstructure of Cast Duplex Stainless Steel after Long–Term Aging," in *Proc. Second Int. Symp. on Environmental Degradation of Materials in Nuclear Power Systems – Water Reactors*, Am. Nucl. Soc., LaGrange Park, IL, 1986, pp. 287–292.

32. H. M. Chung and O. K. Chopra, "Kinetics and Mechanism of Thermal Aging Embrittlement of Duplex Stainless Steels," in *Environmental Degradation of Materials in Nuclear Power Systems – Water Reactors,* G. J. Theus and J. R. Weeks, eds., The Metall. Soc., Warrendale, 1988, p. 359.

33. H. M. Chung and O. K. Chopra, "Long–Term–Aging Embrittlement of Cast Austentic Stainless Steels – Mechanism and Kinetics," in *Properties of Stainless Steels in Elevated Temperature Service*, M. Prager, ed., MPC–Vol. 26/PVP–Vol. 132, ASME, New York, 1988, pp. 17–34.

34. J. Bentley, M. K. Miller, S. S. Brenner, and J. A. Spitznagel, "Identification of G–Phase in Aged Cast CF–8 Type Stainless Steel," in *Proc. 43rd. Electron Microscopy Society of America*, ed. G. W. Bailey, San Francisco Press, 1985, pp. 328–329.

35. M. K. Miller and J. Bentley, "Characterization of Fine–Scale Microstructures in Aged Primary Coolant Pipe Steels," in *Environmental Degradation of Materials in Nuclear Power Systems – Water Reactors*, G. J. Theus and J. R. Weeks, eds., The Metall. Soc., Warrendale, 1988, pp. 341–349.

36. T. J. Godfrey and G. D. W. Smith, "The Atom Probe Analysis of a Cast Duplex Stainless Steel," *J. de Phys. Paris,* Colloque C7, Vol. 47, suppl. to No. 11, p. 217 (1986).

37. J. M. Sassen et. al., "Kinetics of Spinodal Reaction in the Ferrite Phase of a Duplex Stainless Steel," in *Properties of Stainless Steels in Elevated Temperature Service*, M. Prager, ed., MPC–Vol. 26/PVP–Vol. 132, ASME, New York, 1988, pp. 65–78.

38. M. Vrinat, R. Cozar, and Y. Meyzaud, "Precipitated Phases in the Ferrite of Aged Cast Duplex Stainless Steel," *Sci. Metall.* **20**, 1101 (1986).

39. O. K. Chopra and H. M. Chung, "Aging of Cast Duplex Stainless Steels in LWR Systems," *Nucl. Eng. Des.* **89**, 305 (1985).